2-7-2023

The role of the neurodevelopmental disorder gene Myt1l in mammalian brain development

Jiayang Chen
Washington University in St. Louis

WASHINGTON UNIVERSITY IN ST. LOUIS

Division of Biology and Biomedical Sciences
Molecular Cell Biology

Dissertation Examination Committee:
Joseph D. Dougherty, Chair
Brian S. Clark
Harrison W. Gabel
Kristen L. Kroll
Andrew S. Yoo

The Role of the Neurodevelopmental Disorder Gene *Myt1l* in Mammalian Brain Development

by

Jiayang Chen

A dissertation presented to
Washington University in St. Louis
in partial fulfillment of the
requirements for the degree
of Doctor of Philosophy

May 2023
St. Louis, Missouri

Table of Contents

List of Figures

Chapter 1

Supplemental Figures

Chapter 2

Supplemental Figures

Chapter 3

List of Tables

Acknowledgments

Among numerous dreams I had as a child, there is a special one that starts quite early and never fades away: I wanted to become a biologist. Of course, I would not know what it meant to become a biologist then. Especially as a first-generation college student, it is such a long way to go from being an ignorant child to an independent neurogenetic researcher. Fortunately, I got tremendous support from people around me at different stages of my journey to the Ph.D., which enabled me to overcome hurdles and hold on to my passion for biology no matter what happened. Therefore, I would like to recognize these people and express my gratitude for having them along this journey.

First, I would like to thank my parents, Zhengyou Chen and Ping Zeng, for giving me the life to live, the chance to learn, the direction to go, and the ones to love. They have done their best to support me, financially and emotionally, so that I can make it all the way to this Ph.D. Most importantly, they stood with me for whatever decision I made. Unlike traditional Asian parents who often want to have control over kids, my parents allowed me to choose what I like to learn as my college major, to travel to another country for the graduate school, and to explore my potential with my own will, even though they probably did not fully understand what I am studying and where I am heading to. They just believe in their son for no reason, making me confident and fearless in my career. I thank my father for working so hard to earn the life for the family until disease knocked him down, and I will never find a way to make this up but only to make him proud of his beloved son. In addition, I would like to have a huge shoutout for my heroic mother, who is still working after retirement and taking care of my dad while I am gone for years during the pandemic. It is because of her that I can do research thousands of miles away from home without

any worry. I also gained so much positive energy from her every time we talked over the phone. To me, they are the perfect parents who are able to make their child's dream come true, and I dedicate this dissertation to both of them.

The road of my graduate school was never smooth, and I feel extremely lucky to find Dougherty Lab as my thesis lab and fulfill my scientific dreams. I would like to thank my fantastic mentor, Dr. Joseph Dougherty, for being willing to take me when my previous advisor left Washington University. He is no doubt the BEST mentor that I ever worked with, with amazing scientific knowledge to inspire me and powerful will to support me for anything I need. He is not only my academic mentor, but also my friend and, importantly, my cheerleader. Of course, I was surrounded by extraordinary lab mates and collaborators throughout my entire Ph.D. From my original bench mentor Dr. Cheng Cheng, who taught me many basic experimental skills, to my later lab buddies, Tomas, Allen, Simona, Din, Sarah, Sneha, and Mari, whom I talked to about research troubleshooting as well as my daily life, I was constantly learning from them so that I could improve myself and regain energy when I was down. Again, many thanks to Joe for gathering many talented people and bringing in multidisciplinary collaborations to the lab so that I could grow as fast as I could in the past years.

I would like to thank my friends who kept me company during my graduate school career and shared laughter and tears with me all the time. Special thanks to my McDonnell buddies, Lei and Zhen, my graduate school sweeties, Yujie, Lingzhen, Yiqiao, Lijun, Lorenzo, Allen, Melvin, and Simona, and my badminton partners, Chengke (Paco), Tian, and Yuyun. You all are amazing, and I am so grateful for every bittersweet moment we have been through together. I also thank Anthony Fischer, Simona Sarafinovska, Allen Yen, Sneha Chaturvedi, and Sarah Koester for copy editing my dissertation.

Finally, Weijia, my partner, I can never exhaust all the small and big things that I want to thank you for. I still cannot believe that we could meet and fall in love with each other in an overseas city, St. Louis, which is far away from our hometowns. Insisting on having you to buy me dinner for your birthday 5 years ago is the boldest but the best decision that I have ever made, and I managed to "trap" you since then. Without you, my graduate school would not be so joyful. Thank you for tolerating my bad tempers and still loving me after seeing me losing control and falling apart. Thank you for taking such good care of me, physically and emotionally, and offering me unconditional support when I was hungry, or unhappy, or sick, or whenever I needed you for whatever reasonable or ridiculous reasons. Thank you for accepting my stupid self-esteem. Thank you for teaching me how to confront failures. Thank you for traveling with me around the world… I love you, and I cannot wait to write the new chapters of our life with you in the future.

Jiayang Chen

Washington University in St. Louis

May 2023

Dedicated to my parents, Ping Zeng and Zhengyou Chen.

ABSTRACT OF THE DISSERTATION

The role of the neurodevelopmental disorder gene *Myt1l* in mammalian brain development

by

Jiayang Chen

Doctor of Philosophy in Biology and Biomedical Sciences

Molecular Cell Biology

Washington University in St. Louis, 2023

Dr. Joseph D. Dougherty, Chair

Recent human genetic studies have associated mutations in a gene called Myelin Transcription Factor 1 Like (MYT1L) with neurodevelopmental disorders (NDDs). Patients with MYT1L loss of function (LoF) mutations (MYT1L Syndrome patients) demonstrate shared symptoms such as microcephaly, attention deficit and hyperactivity disorder (ADHD), and obesity. Despite prior studies showing MYT1L overexpression facilitates neuronal differentiation *in vitro*, its functions *in vivo*, especially in the mammalian brain, and how its mutation leads to human disease pathology remains poorly understood. Here, I established the first mouse model of MYT1L Syndrome mimicking a patient specific LoF mutation. I found mice with Myt1l heterozygous mutation (Het) display MYT1L haploinsufficiency on both mRNA and protein levels and recapitulate various patient phenotypes. Utilizing this *Myt1l* germline knockout mouse model, I adapted Cleavage Under Targets and Release Using Nuclease (CUT&RUN) technology to map MYT1L binding targets in different developmental stages. Simultaneous measures on chromatin accessibility using Assay for Transposase-Accessible Chromatin with high-throughput sequencing (ATAC-seq), histone modifications using CUT&RUN, and gene expression using RNA-seq revealed that

MYT1L mainly functions a transcriptional repressor during mouse brain development, and its LoF leads to an upregulation of early neuronal development programs in both embryonic cortex and adult prefrontal cortex (PFC). Consequently, in the embryonic cortex, MYT1L loss results in deficient cell proliferation and precocious neuronal differentiation. In juvenile Het mouse visual cortex, neurons also show disrupted morphology and electrical properties. Furthermore, adult Het mice display abnormal cortical neuron layer specification in histology and thinner white matter in diffusion tensor imaging (DTI), and an immature neuronal transcriptional profile. This study developed a novel mouse model of MYT1L Syndrome and defined molecular and cellular functions of MYT1L during mammalian brain development, providing a useful toolkit for future pre-clinical studies of this human NDD.

Chapter 1: Introduction to the dissertation

Jiayang Chen, Allen Yen, Colin P Florian, Joseph D Dougherty

Adapted From:

MYT1L in the making: emerging insights on functions of a neurodevelopmental disorder gene.

Chen, J.*, Yen, A.*, Florian, C.P.*, Dougherty, J.D. (2022). MYT1L in the making: emerging insights on functions of a neurodevelopmental disorder gene. Translational Psychiatry, 2022;12(1):292.

1.1 Neurodevelopmental Disorders (NDDs)

1.1.1 NDD genetics

Neurodevelopmental disorders (NDDs) are complicated conditions that can affect the normal developmental trajectory of nervous system anatomy, motor skills, emotion, cognition, and various behaviors (Mullin et al. 2013). Some common examples of NDDs are attention-deficit/hyperactivity disorder (ADHD), autism spectrum condition (ASC), and intellectual disability (ID). Globally, the prevalence of NDDs ranges from 4.7 to 88.50% (Francés et al. 2022). More specifically, NDDs impact approximately 15% of children in the US, according to a 2008 parental survey from (Boyle et al. 2011). A new study from 2022 estimates roughly 1 in 4 publicly and 1 in 9 privately insured children have been diagnosed with a at least one NDD in the US (Straub et al. 2022). NDDs impose significant financial and emotional burden on patients and their families since some of these disorders can be challenging to treat. Patients often require life-long symptom management as developmental deficits can result in multifaceted conditions that affect individuals as adults (Xie et al. 2022). Nevertheless, the cause of NDDs remains poorly understood.

The etiology of NDDs consists of heterogenous and complex contributor with genetic factors as an important category. With the advances of human genetics in the past decades, many genetic mutations have been associated with NDDs. To understand the potential genotype-phenotype correlation, two main principles have been proposed: gene vulnerability, which represents the ability of a gene to tolerate detrimental mutations, and mutational load, which consists of both pathogenic germline and somatic mutations (Parenti et al. 2020). Indeed, the majority of published works have supported that the genetic etiology of NDDs is multifactorial and polygenic (Parenti et al. 2020), making it difficult to study and to develop broadly applicable therapies. Despite the heterogenous origins of NDDs, mutations in a single gene can also lead to

disease pathogenesis. For example, Rett Syndrome, a NDD that results in intellectual disability and motor deficits, is caused by mutations in a gene called Methyl-CpG Binding Protein 2 (*MECP2*) (Guy et al. 2001). In addition, several NDD-associated mutations are located in chromatin regulators/transcription factors (TFs), such as FOXP1, SETD5 and CHD8 (Araujo et al. 2015; Sessa et al. 2019; Katayama et al. 2016). Interestingly, functional studies found that different NDD genes can affect a consistent set of pathways (Parikshak et al. 2013; Sahin and Sur 2015; Voineagu et al. 2011), such as protein synthesis (Borrie et al. 2017), transcriptional and epigenetic regulation (Ronan, Wu, and Crabtree 2013), and synaptic function (Bourgeron 2015). This indicates that studying one specific NDD-associated gene can provide insight to other NDD syndromes, presenting an opportunity to understand any common pathogenesis and develop general therapies.

1.1.2 Animal models of NDDs

Model organisms are frequently used to perform functional studies to determine the consequences of disease associated genetic variants (Hedges 2002). Leveraging modern gene editing tools, animal models with patient-derived mutations can be generated to investigate disease pathology and test preclinical therapies (Perlman 2016; Lieschke and Currie 2007). In addition, utilizing animal models such as drosophila, zebrafish, and mice, provides special advantages in NDD research since they have relatively shorter developmental timelines than primates but still exhibit fairly complex behaviors, allowing us to assess how genetic mutations affect their developmental trajectories and cognitive functions (Bozzi and Fagiolini 2020). Therefore, animal models of different NDDs have been established to further understand NDD etiology. For example, drosophila and mouse models of Fragile X Syndrome, which is caused by mutations on a gene called Fragile X Messenger Ribonucleoprotein 1 (*FMR1*), have been characterized and utilized to

drastically advance therapeutic studies for this syndrome (Drozd, Bardoni, and Capovilla 2018; Kazdoba et al. 2014). Despite the growing use of animal models to study NDDs, only one zebrafish model of MYT1L knockout has been previously generated using morpholinos, which was briefly characterized to have neuroendocrine deficits (Blanchet et al. 2017). However, there is no well-characterized mammalian model for MYT1L Syndrome, which is needed to further investigate its pathology and explore therapeutic opportunities.

1.2 Myelin Transcriptional Factor 1 Like (MYT1L)

1.2.1 MYT1L Syndrome

Human genetic studies have recently identified the gene Myelin Transcription Factor 1 Like (MYT1L) as associated with neurodevelopmental disorders (NDDs) (de Ligt et al. 2012; De Rubeis et al. 2014; Sanders 2015; Wang et al. 2016; Blanchet et al. 2017; Loid et al. 2018; Satterstrom et al. 2020; Windheuser et al. 2020; Coursimault et al. 2022). Among those patients with *MYT1L* heterozygous loss of function (LoF) mutations, which might result in MYT1L haploinsufficiency, ID, ASC, ADHD, and developmental delay are the most common symptoms. Other phenotypes include seizures, syndromic obesity, microcephaly, macrocephaly, and muscular hypotonia. This constellation of symptoms has now been recognized as MYT1L Syndrome or 2p25.3 Deletion Syndrome (Blanchet et al. 2017; Coursimault et al. 2021; Mansfield, Constantino, and Baldridge 2020; Windheuser et al. 2020). Much remains unknown about MYT1L Syndrome's etiology since it is still an emerging NDD, with few studies looking at how MYT1L mutations can lead to human disease pathogenesis.

1.2.2 The association between MYT1L mutations and human diseases

Currently, there are over 100 described patients with 80% of them harboring potential

MYT1L LoF mutations and others harboring *MYT1L* partial duplications (Blanchet et al. 2017; Coursimault et al. 2021; Mansfield, Constantino, and Baldridge 2020; Windheuser et al. 2020). Specifically, MYT1L loss of function is associated with Intellectual Disability (ID) and Autism Spectrum Condition (ASC), while MYT1L duplication has been observed in patients with schizophrenia (SCZ) (Mansfield, Constantino, and Baldridge 2020). Yet, the mechanism by which MYT1L variants contribute to disease pathology is still unknown.

MYT1L LoF mutations include deletions, frameshift, and single nucleotide variations (SNVs), which are predicted to cause decreases in mRNA production or aberrant protein functions. Notably, missense mutations from clinical but not general-population studies cluster in the central zinc finger domains and the MYT1 domain (Adzhubei et al. 2010; Karczewski et al. 2020) (**Fig. S1A**), the most confident structures predicted by AlphaFold (**Fig. S1B**), indicating these domains might be crucial for the protein functions. In addition, most patients with *MYT1L* partial duplications were reported to either have ID, ASC, or both.

Regarding human full duplications, although 33% of *MYT1L* duplication patients presented with SCZ exclusively, all but one of those duplications contain neighboring gene *PXDN*, indicating MYT1L may or may not be the only contributing factor in the region for SCZ risk (Mansfield, Constantino, and Baldridge 2020). The association of both LoF and putative duplications with disease indicates that neurobiology is very sensitive to the levels of MYT1L activity, and identifying the loci that are influenced by altered MYT1L levels might aid in understanding the downstream pathophysiology. In sum, the emerging role of MYT1L in NDDs highlights the importance of a more complete understanding of MYT1L within transcriptional networks, and identification of its targets is essential to systematically study the downstream consequences of MYT1L haploinsufficiency.

1.2.3 Cellular function of MYT1L

Neuronal identity is determined by the effects of a combination of basic helix-loop-helix (bHLH; e.g., ASCL1, NEUROD1, and NEUROG1) transcription factors (TFs) as well as other developmentally expressed TFs such as BRN2 and MYT1L. *In vitro* overexpression studies have shown that the pioneer factor ASCL1 is sufficient for induction of neuronal traits, but overexpression in combination with other factors such as BRN2, and especially, MYT1L are necessary for efficient mouse embryonic fibroblast (MEF) conversion to neurons as well as maturation of the induced neurons (iNs) (Mall et al. 2017; Tomaz 2016; Vierbuchen et al. 2010a). Ultimately, many of these studies suggest that MYT1L and other members of the MYT family primarily function to preserve neuronal phenotypes as it has been shown that MYT1L is mostly expressed during the post-specification phase when cell populations have become post-mitotic. Furthermore, none of the MYT family members were observed to be expressed by *in situ* hybridization in germinal zones containing mostly undifferentiated cells (Kameyama et al. 2011; Matsushita et al. 2014), again arguing against an instructive role in neuronal specification *in vivo*.

Interrogation of specific domains of MYT1L has further defined its role in neuronal conversion. For example, Mall et al. (2017) showed that, when fused to an activating element (VP64), the DNA binding domains of MYT1L displayed a dominant-negative effect on ASCL1-mediated neuronal conversion. Additionally, just a 423-amino-acid fragment (i.e., amino acids 200-623), which contains the N-terminal domain and the middle two zinc fingers, was functionally indistinguishable from full-length MYT1L in driving neuronal conversion. Surprisingly, this fragment does not contain the MYT1 domain.

In contrast to the overexpression studies discussed above, knockdown of MYT1L via short hairpin (sh) RNAs resulted in a reduction of neuronal maturation gene programs such as neurite

outgrowth, axonal development, synaptic transmission, and ECM composition, which hints that MYT1L also acts as an activator (Kepa et al. 2017). It has also been reported that MYT1L was found to be deleted (~5%) and downregulated (>80%) in glioblastomas suggesting that gliomagenesis requires neutralization of terminal neural differentiation (Hu et al. 2013). Furthermore, others have shown that MYT1L and MYT1 expression can slow tumor growth in glioblastoma cell line models via repression of pro-proliferative genes (Melhuish et al. 2018). However, impacts on glia *in vivo* are likely not direct since MYT1L expression has not been consistently observed in glia (Kim et al. 1997). Therefore, it remains to be determined when and how MYT1L functions as a repressor and activator respectively.

Spatiotemporal expression of MYT family TFs is finely tuned across development, and specifically across neuronal maturation. Of the MYT family, Myt1 and Myt3 are expressed the earliest at embryonic (E) day 9.5 as suggested by in situ hybridization (Matsushita et al. 2014). Quantitative RT-PCR results showed that *Myt1* and *Myt1l* were upregulated from E10.5 to E15.5 and then down-regulated postnatally (**Fig. S2A**) (Matsushita et al. 2014). Additionally, *Myt1l* mRNA levels increase across neurogenesis in mice, and low levels are sustained in adulthood, which mirrors human expression patterns (Matsushita et al. 2014). The earliest time point of detectable *Myt1l* expression occurs at E9.5 in the ventrolateral portion of the spinal cord, again where newborn neurons are found. In addition, at E12.5, BrdU staining hardly overlapped with *Myt1l* expression, further supporting that *Myt1l*-positive cells were mostly post-mitotic (Matsushita et al. 2014). Indeed, across the multiple CNS regions examined (spinal cord, hindbrain, midbrain, cortex, and retina) *Myt1l* RNA was upregulated when neurons began to differentiate (**Fig. S2B**) and overlapped with markers of neurons. Overall, analysis of MYT1L expression pattern and time course further supports the assumption that it is responsible for

neuronal maturation and preservation of cell fate. However, there is a lack of loss of function evidence showing MYT1L is required for neuronal maturation and neuronal identity maintenance *in vivo*, which can be more informative for understanding human disease pathology.

As mentioned in the above section, one zebrafish study has shed light on MYT1L's necessity for neuronal maturation. They found knocking down zebrafish MYT1L orthologs, myt1la and myt1lb, by antisense morpholinos results in almost complete loss of oxytocin (OXT) and arginine vasopressin (AVP) in the neuroendocrine pre-optic area of the hypothalamus, suggesting MYT1L LoF might affect neuroendocrine system development (Blanchet et al. 2017). In addition, another group showed that MYT1L knockdown via shRNA delivered by *in utero* electroporation led to deficient neuronal migration in the developing mouse cortex, emphasizing MYT1L's roles in promoting neuronal differentiation (Mall et al. 2017). However, before my thesis work, no MYT1L germline knockout model was established to investigate MYT1L LoF *in vivo*. In addition, the longer consequences of MYT1L loss and the functions of MYT1L in adult central nervous system are largely unknown.

1.2.4 Molecular function of MYT1L

Structurally, MYT family TFs have several domains that may define their functions, and many initial studies of MYT family TFs focused on characterization of structural domains and DNA binding (Jiang et al. 1996; J. G. Kim et al. 1997). Sequence analysis of MYT1L isolated from rat pituitary and cerebellum cell lines showed that the protein has six zinc finger domains (Cys-Cys, His-Cys) that are organized into clusters with one at the N-terminus, a pair upstream of the Myt1 domain, and three at the C-terminal domain (Jiang et al. 1996). Using Alphafold (Jumper et al. 2021; Varadi et al. 2022) to model the structure of MYT1L, these six zinc finger domains are predicted to come together to form a DNA binding pocket (**Fig. S1C**). *MYT1L* LoF mutations

based on patient reports can be found throughout all domains of the protein (**Fig. S1D)** with a notable cluster of mutations within the central zinc finger domains (**Fig. S1E**). The N-terminus contains a highly acidic region, and a Ser/Thr-rich region between the zinc finger and coil domain.

The zinc fingers are thought to be involved in DNA-binding. These authors note that the core sequence recognized by the MYT1L zinc fingers, specifically from the two zinc fingers upstream of the MYT1 domain, is GAAAGTT (Jiang et al. 1996). An additional GTT that resides 4bp 5' of the core sequence element was observed in the DNA binding motif when testing the construct with the three zinc fingers at the C-terminal end of the protein. Competitive binding assays showed that AAGTT was the most crucial for binding (Jiang et al., 1996), which is consistent with the motif Mall et al. (2017) report from their ChIP-seq experiments. Further, two additional purines at the 5' end (RRAAGTT) are preferred for optimal binding. The N-terminus, which is the least conserved domain among the MYT family of TFs, with its highly acidic region that is enriched for Glu/Asp residues, has been implicated in transcriptional activation (Jiang et al. 1996; Manukyan et al. 2018), a function that appears dispensable for production of iNs (Mall et al. 2017).

The N-terminus, MYT1 domain, and C-terminus of MYT1L also contain structural components that are both unique to MYT1L as well as the MYT family. The MYT1 and C-terminal domains are highly conserved across the MYT family, and the MYT1 domain contains a Ser/Thr-rich region in both proteins (Jiang et al. 1996; Mall et al. 2017). The N-terminus of MYT1L, which is the least conserved domain among the MYT family of TFs, is composed of a highly acidic region that is enriched for Glu/Asp residues (Jiang et al. 1996; Mall et al. 2017).

As a TF, the primary function of MYT1L is supposed to bind *cis*-regulatory elements in the genome and mediate gene expression. Therefore, identifying where MYT1L binds in the

genome is essential to understand how MYT1L directly controls transcriptional networks in neurons and facilitates neuronal differentiation. While studies of gene expression are informative, they do not distinguish directly from indirect regulation. Direct targets have been identified by Chromatin Immunoprecipitation Sequencing (ChIP-seq) primarily in fibroblasts overexpressing MYT1L and with limited samples from endogenous MYT1L in the developing mouse brain (Mall et al. 2017). Within a subset of ChIP-seq peaks, the previously described AAGTT motif was enriched within downregulated genes in fibroblasts, consistent with the hypothesis of MYT1L's role as a transcriptional repressor. In particular, MYT1L repressed Notch signaling and Hes1 to promote neurogenesis. Unfortunately, the endogenous MYT1L ChIP-seq experiments did not work as efficiently as in fibroblast system since the data quality was not ideal, and only 500 MYT1L binding regions were identified. Meanwhile, Mall et al. (2017) only performed ChIP-seq on embryonic day 14 (E14) mouse brain (Mall et al. 2017). Little was known whether MYT1L adopted new targets in the later developmental time points or whether MYT1L has distinct targets in the different adult brain regions. More efficient measures on MYT1L binding across different stages central nervous system development and different brain regions are needed to comprehensively understand MYT1L normal functions in neuronal development and its LoF in human disease pathology.

1.3 Strategies for Protein-DNA binding profiling

1.3.1 Chromatin Immunoprecipitation Sequencing (ChIP-seq)

Chromatin Immunoprecipitation Sequencing (ChIP-seq) is a widely used technique to map DNA binding targets of a certain protein or profile histone modification landscapes. ChIP-seq leverages the traditional chromatin immunoprecipitation assay (Solomon, Larsen, and Varshavsky 1988) and advances in next generation sequencing (NGS) to assess protein binding with base pair

resolution (Johnson et al. 2007; Barski et al. 2007). General steps of ChIP-seq include formaldehyde cross linking, DNA shearing, antibody-based immunoprecipitation, DNA purification, library preparation, and deep sequencing (Park 2009). In the past decades, ChIP-seq has been extremely successful as it provides larger scale profiling in the genome of a DNA binding protein and better resolution compared to other methods like Chip-chip (Park 2009). However, there are several limitations in ChIP-seq. First, the ChIP-seq process requires breaking up cells and chromatin, which might destroy native interactions between proteins and DNA. Although cross-linking can be used to strengthen these interactions (Tian, Yang, and Brasier 2012), formaldehyde, the agent used for cross-linking, can mask epitopes and reduce immunoprecipitation efficiency (Dapson 2007), consequently affecting ChIP-seq sensitivity. Likewise, since ChIP-seq does not have great signal to noise ratio, a paired-end sequencing depth of at least 30M reads is needed to reliably call peaks (Jung et al. 2014). ChIP-seq also requires a high quality protein-specific antibody to enrich genomic fragments bound by the target protein (Park 2009). If there is no antibody available or none works well for ChIP of the target protein, ChIP-seq for that specific protein will be impossible. Last, the ChIP-seq process can be time consuming and tedious, and it can last a whole week (Park 2009). Therefore, a more efficient, sensitive, and affordable method is desirable to accommodate the increasing demands for protein-DNA binding profiling.

1.3.2 Cleavage Under Targets and Release Using Nuclease (CUT&RUN)

Cleavage Under Targets and Release Using Nuclease (CUT&RUN) is a new high-resolution protein-DNA interaction profiling technique first described by the Henikoff group in 2017 (Skene and Henikoff 2017). CUT&RUN utilizes protein A-tethered MNase (pA-MNase) that binds to antibodies and cleaves nearby genomic regions to enrich protein-bound DNA fragments

for sequencing (Skene and Henikoff 2017). Standard procedures of CUT&RUN include nuclei extraction, binding nuclei to magnetic beads, primary antibody incubation, binding pA-MNase to primary antibody, activation of pA-MNase, elution of genomic fragments, and library preparation for sequencing. CUT&RUN offers several advantages over traditional ChIP-seq for protein-DNA interaction profiling (Meers et al. 2019). First, CUT&RUN does not require cross-linking, allowing detection of protein-DNA interactions in their natural states (Skene and Henikoff 2017). Second, CUT&RUN significantly reduces background signal, thus increasing meaningful biological signal, so that the amount of input material (as low as 1,000 cells) and sequencing depth needed to produce high-quality mapping is drastically reduced (Meers et al. 2019). Last, the procedure of CUT&RUN is simpler than ChIP-seq, allowing simultaneous preparation for multiple reactions (Meers et al. 2019; Skene, Henikoff, and Henikoff 2018). Although it might sound like CUT&RUN is a perfect technology for protein-DNA interaction profiling, one big limitation is that CUT&RUN is not compatible with existing single cell pipelines. Therefore, if the target protein is only expressed in a small portion of the input cells, profiling efficiency will be reduced, and more starting materials might be necessary to ensure accurate measuring.

1.3.3 Cleavage Under Targets and Tagmentation (CUT&Tag)

To overcome some of the limitations of both ChIP-seq and CUT&RUN, Cleavage Under Targets and Tagmentation (CUT&Tag) was developed to enable fast and multimodal protein-DNA interaction and histone modification profiling (Kaya-Okur et al. 2019). Instead of tethering protein A with MNase, CUT&Tag utilizes protein A-tethered Tn5 transposase (pA-Tn5), a hyperactive enzyme that cuts naked DNA and inserts transposons into DNA, to cleave out genomic regions near the target protein binding sites while simultaneously adding adapter sequences to DNA fragments (Kaya-Okur et al. 2019). Similar to the CUT&RUN protocol, CUT&Tag requires

binding nuclei to magnetic beads, primary antibody incubation, secondary antibody incubation, binding pA-Tn5 to secondary antibody, cleavage, elution, and library preparation (Kaya-Okur et al. 2020). Since pA-Tn5 cleavage can insert adapter sequences at its cutting sites, only one final PCR amplification is needed to add sequencing indexes and amplify libraries, which significantly decreases library preparation time compared to ChIP-seq and CUT&RUN (Kaya-Okur et al. 2020). In addition, customization of adapter sequences added by Tn5 transposases will allow simultaneous measures for different target proteins and histone modifications with the same input materials (Gopalan et al. 2021; Gopalan and Fazzio 2022). This barcoding feature upon cleavage makes CUT&Tag compatible with single cell assays (Bartosovic, Kabbe, and Castelo-Branco 2021; Wu et al. 2021). In the past two years, based on the original CUT&Tag platform, different multimodal chromatin profiling techniques have been developed to measure histone modifications and chromatin accessibility in the same cell (Gopalan et al. 2021; Meers et al. 2022; Bartosovic and Castelo-Branco 2022). Although CUT&Tag is thought to have extremely low background signals, CUT&Tag works more efficiently on highly abundant proteins, like RNA Polymerase II, or histone modifications than on regular TFs, while CUT&RUN works for both rare and abundant targets. This might be because the background activity of pA-Tn5 is still high enough to mask any signals produced by rare targets. Therefore, for any TF of interest, such as MYT1L in this dissertation, pilot experiments will be necessary to determine if CUT&Tag will be a good fit. If not, CUT&RUN might offer a better solution in terms of TF binding profiling.

1.4 Conclusions

MYT1L is a novel neurodevelopmental disorder gene recently associated with a constellation of symptoms (Blanchet et al. 2017; Coursimault et al. 2021; Mansfield, Constantino, and Baldridge 2020; Windheuser et al. 2020). Previous *in vitro* studies have shown that

overexpression of MYT1L together with ASCL1 and BRN2 can directly reprogram MEF into functional neurons (Vierbuchen et al. 2010b). During this processes, MYT1L suppresses non-neuronal genes to facilitate neuronal differentiation (Mall et al. 2017). Although limited *in vivo* studies revealed MYT1L is important for neuroendocrine development in zebrafish (Blanchet et al. 2017), no mammalian animal model has been established to study how MYT1L mutations lead to disease phenotypes and what the potential long-term consequences of MYT1L loss are. In addition, MYT1L's molecular and cellular functions *in vivo* need further investigation to shed light on how MYT1L promotes neuronal differentiation and maturation during normal brain development. Therefore, the key goals of this dissertation were to: 1) generate and characterize a mammalian animal model for MYT1L Syndrome; 2) map MYT1L binding sites in the brain across development; 3) define molecular mechanism underlying how MYT1L regulates neuronal gene expression; 4) determine cellular functions of MYT1L and the long-term consequences of MYT1L loss *in vivo*.

1.5 Figures

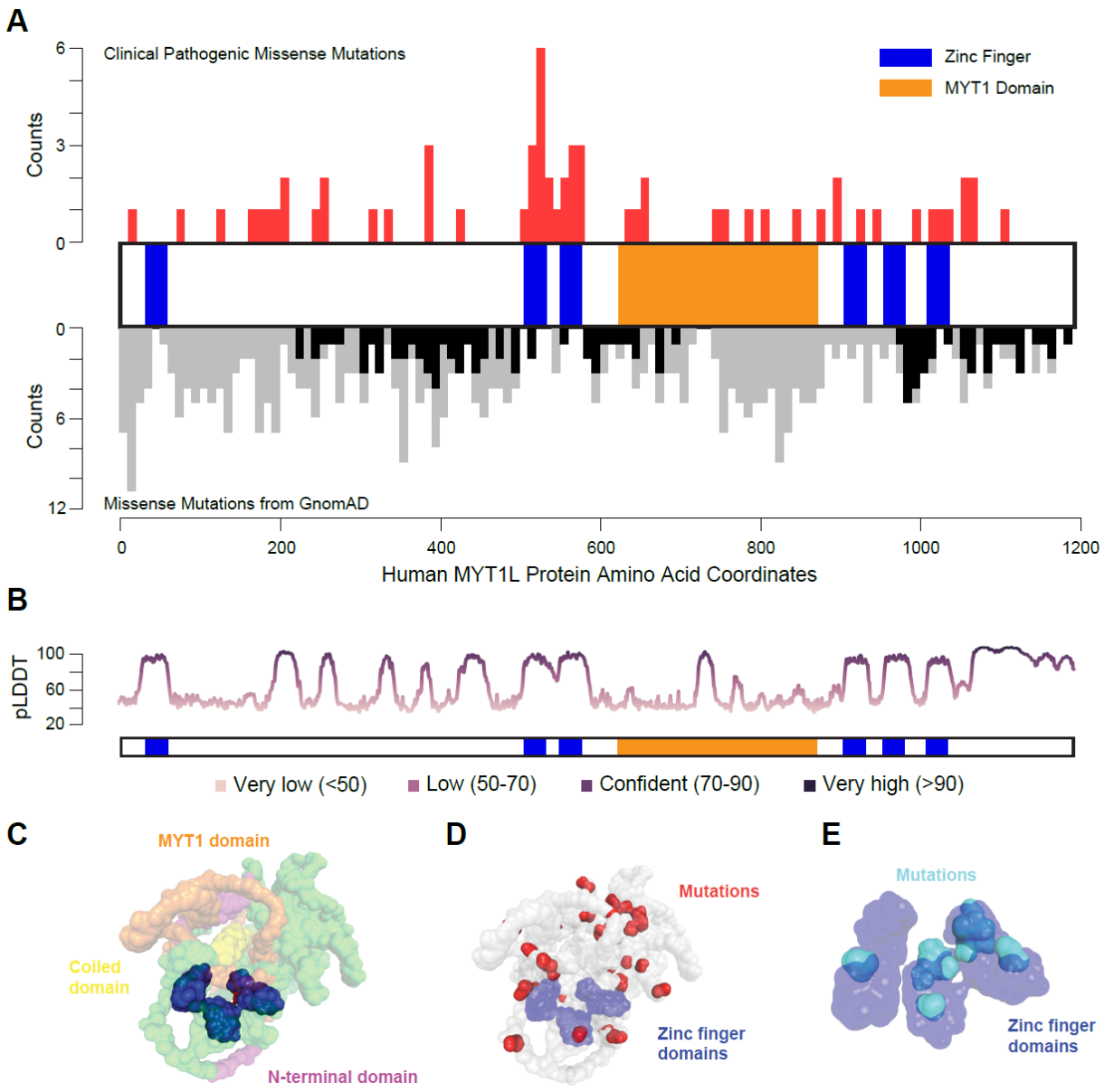

Supplemental Figure 1: Schematic of human MYT1L domains and predicted protein structure by AlphaFold.

(A) Distribution of missense mutations described in clinical studies (top, red) compared to a general population sample (gnomAD, bottom, with gray bars displaying all missense mutations and black bars displaying 'possible damaging mutations' as predicted by PolyPhen2). 'Possible damaging mutations' in the general population are largely excluded from the regions mutated in clinical samples. **(B)** AlphaFold's calculated confidence measure (pLDDT score) per-residue of

the model's prediction based on the IDDT-Cα metric **(C)** 3D AlphaFold structure (AF-Q9UL68-F1) prediction of MYT1L protein showing the N-terminal domain (magenta), MYT1 domain (orange), coiled domain (yellow), and six zinc finger domains (blue) coming in proximity with each other to form a putative DNA-binding pocket. Unannotated regions are shown in green. (https://alphafold.ebi.ac.uk/entry/Q9UL68). **(D)** Loss of function mutations from patient reports are found throughout the protein. Those not within the annotated zinc finger domains (blue) are shown in red. **(E)** Isolated and magnified view of the zinc finger domains (blue) shows patient mutations (cyan) cluster in the zinc fingers.

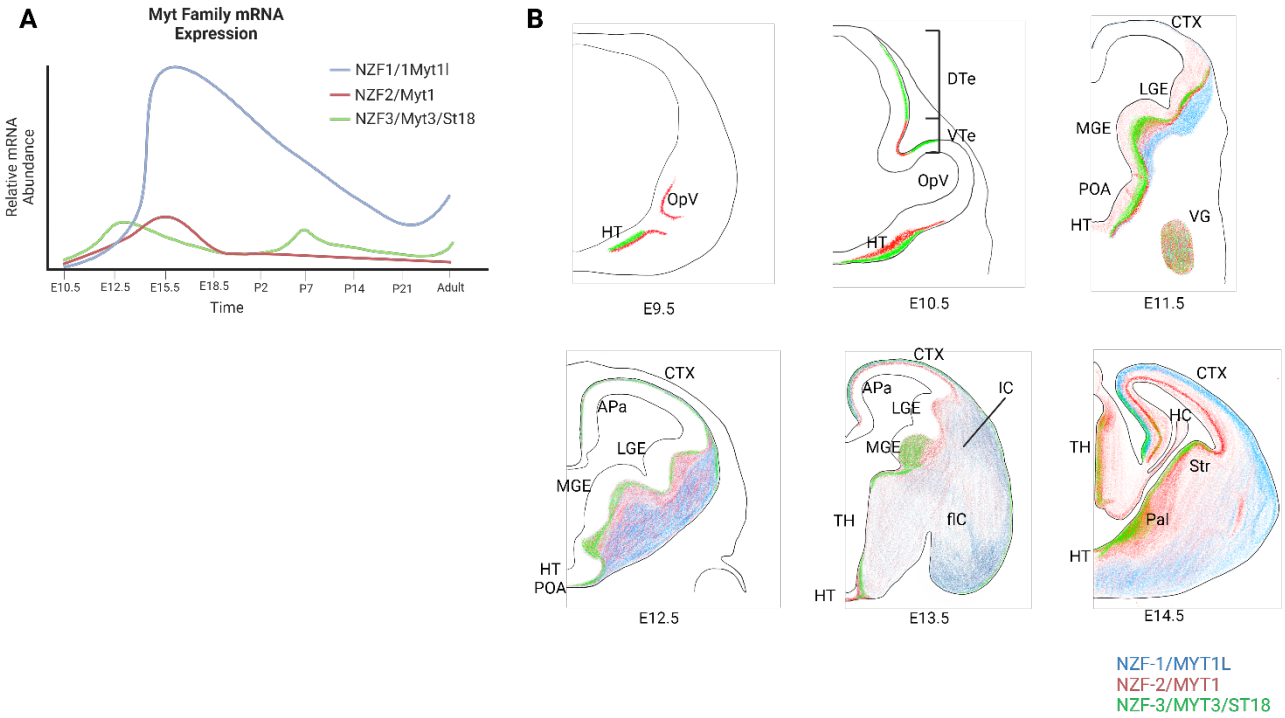

Supplemental Figure 2: Mouse embryonic brain expression patterns of MYT family transcription factors.

(A) Quantitative RT-PCR summarized as relative mRNA expression of *Myt1* (red), *Myt1l* (blue), and Myt3 (green) in the developing mouse from E10.5 to adult, adapted from (Matsushita et al. 2014). **(B)** Color coded summary of published in situ hybridization data from Matsushita et al., (2014) showing spatial expression pattern of MYT1, MYT1L, and MYT3 in the developing cortex. *APa, archipallium; BG, basal ganglia; CTX, cortex; DTe, dorsal telencephalon; fIC, fibers of the internal capsule; HC, hippocampus; HT, hypothalamus; IC, internal capsule; LGE, lateral ganglionic eminence; MGE, medial ganglionic eminence; OpV, optic vesicle; Pal, pallidum; POA, preoptic area; Str, striatum; TH, thalamus; Vg, trigeminal ganglion; VTe, ventral telencephalon.*

Chapter 2: Generation and Characterization of MYT1L Germline Knockout Mouse Model

Jiayang Chen, Xia Ge, Joshua T. Dearborn, Yating Liu, Katherine B. McCullough, Raylynn G. Swift, Lucy Tian, Kevin Noguchi, Joel R. Garbow, John N. Constantino, Susan E. Maloney, Joseph D. Dougherty

Adapted From:

A MYT1L syndrome mouse model recapitulates patient phenotypes and reveals altered brain development due to disrupted neuronal maturation

Chen, J., Lambo, M.E., Ge, X., Dearborn, J.T., Liu, Y., McCullough, K.B., Swift, R.G., Tabachnick, D.R., Tian, L., Noguchi, K., et al. (2021). A MYT1L syndrome mouse model recapitulates patient phenotypes and reveals altered brain development due to disrupted neuronal maturation. Neuron vol. 109,23 (2021): 3775-3792.e14.

2.1 Introduction

In this chapter, I will focus on how I established a novel mouse model for MYT1L Syndrome, which harbors a patient specific mutation described locally at Washington University School of Medicine. With the help from the Genome Engineering and Stem Cell Center (GESC) at Washington University in St. Louis, a *Myt1l* germline knockout mouse line was generated and confirmed with MYT1L loss at both mRNA and protein levels. Next, physical traits were examined on these *Myt1l* knockout mice. Then, brain histology and diffusion tensor imaging (DTI) was performed to investigate anatomical changes of *Myt1l* mutant brains. Finally, to assess if this mouse line mimics behavioral aspects of human MYT1L Syndrome and can be useful for future pre-clinical studies, a series of behavioral assays were conducted to test how MYT1L loss affects mouse behavior.

2.2 Results

2.2.1 Generation of *Myt1l* germline knockout mouse line

Germline mutants of *Myt1l* would enable studies of its role in CNS development, its function on chromatin, gene expression, and the cellular, physiological, and behavioral phenotypes of haploinsufficiency. Therefore, I generated mice with a mutation on exon7 (chr12:29849338, c.3035dupG, S710fsX; **Fig. 1A**), based on a MYT1L patient mutation in the homologous exon 10 (**Appendix Table 2**), resulting in frameshift and a predicted stop-gain (**Fig. 1B**). As I found *Myt1l* homozygous mutant (KO) mice die at birth, I confirmed *Myt1l* transcripts and protein decreased by 25% in heterozygous mice (Het; **Fig. 1C, D, E**), and IF showed complete MYT1L protein loss in KO E14 mouse cortex (**Fig. 1F**). No truncated protein (est. 80.63 kDa) was produced by the mutation (**Fig. 1G**). Further sequencing of the cDNA from Hets revealed a depletion of the mutant

mRNA compared to genomic controls, consistent with nonsense mediated decay (**Fig. 1H**). Thus, this mutation appears to result in haploinsufficiency.

2.2.2 Physical characterization of *Myt1l* knockout mice

To understand how well this mouse line can mimic patient phenotypes, physical abnormalities reported in patients were first assessed for physical abnormalities. I observed clinodactyly (**Fig. 2A**) and abnormal hindlimb posture: transient hyperflexions of one or both hindlimbs (**Fig. 2B, C**), reflected not in clasping, but in holding limb(s) at midline. Finally, I also observed obesity in Hets. There was an initial separation of group weights at P45 which became statistically significant at P94, and was more pronounced in females than males (**Fig. 2D**). Thus, *Myt1l* mutation results in physical alterations and obesity in mice and humans.

2.2.3 Neuroanatomical characterization of *Myt1l* knockout mice

Almost half of patients have central nervous system (CNS) malformations like microcephaly, hydrocephalus and thinned white-matter. Therefore, I investigated structural abnormalities in P60 Hets with Nissl staining (**Fig. 3A, B**). Brain organization was grossly normal, yet Hets had decreased brain weight and smaller cortical volume (**Fig. 3C, D**) with no change in cortex/brain ratio (**Fig. S3A**). Regarding white-matter, there was a trend towards reduced corpus callosum volume (**Fig. S3B**). In addition, there was no cell density change (**Fig. S3C**), indicating that microcephaly in Hets corresponds to fewer cells, rather than less parenchyma.

I next investigated mouse brains with magnetic resonance (MR)-based Diffusion Tensor Imaging (DTI) in collaboration with the IDDRC developmental neuroimaging core. This is a more sensitive, *in vivo*, clinically-translatable technique that can provide both structural and functional information (**Fig. 3E**). From maps of apparent diffusion coefficient (**ADC; Fig. S3D**) and fractional anisotropy (FA**; Fig. 3F**), I segmented several brain regions and performed 3D

reconstruction (**Fig. 3G, S3E, F**). By MR, Hets again had smaller brain volumes, with no size change in the ventricular system (**Fig. 3H, S3G**). With segmentation of FA maps (**Fig. 3F, G**), Hets had a smaller corpus callosum volume (**Fig. 3I**). Functionally, FA values were unchanged in white matter and cortex, suggesting that remaining axons were normal (**Fig. S3H**). This suggests the decrease in white matter reflects a loss of axons rather than oligodendroglial dysfunction (e.g. dysmyelination). Overall, *Myt1l* mutation results in both decreased brain size and smaller specific white-matter tracts.

2.2.4 Behavioral characterization of *Myt1l* knockout mice

Last, I determined behavioral circuit consequences resulting from MYT1L haploinsufficiency. I evaluated Hets for features related to developmental delays, ID, ADHD, and ASC present in human MYT1L deletion patients. Language and motor delay are universal in MYT1L deletion patients (Blanchet et al. 2017), therefore, I assessed Hets for gross developmental, communication, and motor delay. Physically, Hets did not exhibit signs of gross developmental delay in pinnae detachment, eye opening, and postnatal weight gain (**Fig. 4A**). I examined early communicative interaction by recording ultrasonic vocalizations (USV) emitted by isolated pups. Hets exhibited increased USV rates (**Fig. 4B**) following maternal separation that is likely independent of altered respiratory muscle function (**Fig. 4C-F**). Rather than delayed communicative behavior, this elevated rate suggests an anxiety-like phenotype or, since USV rate also reflects arousal levels, a heightened arousal that may reflect a hyperactive phenotype.

As patients show ID, in collaboration with Dr. Susan Maloney, we examined spatial learning and memory and Pavlovian fear conditioning. Hets displayed normal spatial acquisition and memory retention in the Barnes maze (**Fig S4A, B**). However, Hets failed to show typical contextual and cued fear conditioning (**Fig. S4C**), suggesting decreased associative memory. In

the same cohort of mice, we examined activity levels for ADHD-like features at P30. Regardless of sex, Hets were hyperactive in the open-field task, traveling a greater distance than WT littermates (**Fig. S5A**). This hyperactivity replicated in subsequent assays: in distance traveled in the social operant task and in heightened baseline force measurements in the startle task (a measurement of movement in the apparatus in the absence of startle stimuli; **Fig. S5B**). This hyperactive phenotype confounds the interpretation of the conditioning data above because it can mirror a conditioning deficit in this task. Thus, further investigations are necessary to understand any learning deficits in this model. Finally, we assessed the center variables of the open field task for anxiety-related behaviors (thigmotaxis), and found no increase in anxiety-related behavior in Hets as measured in this task (**Fig. S5C**). The hyperactivity phenotype in the absence of anxiety-related markers sheds more light on the heightened USV data, supporting an interpretation that the increase in call rate reflects elevated arousal.

We also investigated multiple behaviors related to ASC circuits. First, we investigated cognitive inflexibility, sensory sensitivity, repetitive behaviors and stereotypies across multiple assays. In the spontaneous alternation T-maze, Hets exhibited comparable percent alternation to WTs (with both different from chance, 50%; **Fig. S5D**), indicating no preservation here. To assess sensory sensitivities, we quantified responses to stimulation of the plantar surface of the paw with von Frey filaments. Het mice exhibited an overall reduced sensitivity to this tactile stimulation (**Fig. S5E**). Examination of open field movement plots revealed sharp vertical movements in the perimeter, suggestive of jumping. Therefore, we re-analyzed the video-data (**Fig. S5F**) to generate supervised machine-learning behavioral predictive classifiers for automated quantification of jumping behavior. Despite hyperactivity displayed by both male and female Hets (**Fig. S5A**), only female Hets exhibited significantly more jumping (**Fig. S5G**). Therefore, this may be a female-

specific overactivity trait. We also did not observe grooming-like stereotyped behavior in the force-plate actometer (FPA), the form of bouts of low mobility, or movement during those bouts (**Fig. S5 H, I**). Indeed, our machine learning classifier revealed that while there was an interesting sex difference in duration of grooming bouts (**Fig. S5J**), *Myt1l* mutation did not further modulate this behavior (**Fig. S5K**). Thus, in the tasks used here, no behaviors related to repetitive/restrictive interests or stereotypies were observed.

Previous work suggested MYT1L promotes differentiation of oligodendroglia (Shi et al., 2018), which could impact myelination. Demyelination can result in a tremor in mice, as assessed by the FPA (Li et al., 2019). However, we did not observe any tremor in Hets (**Fig. S5L**), suggesting the white matter anomalies we see do not reflect demyelination, consistent with the normal FA values (**Fig. S3H**).

Finally, we assayed multiple aspects of social behavior. To assess social hierarchy behavior, we used the social dominance tube test. MYT1L loss was associated with submission in this test (**Fig. 5A**). In the social approach task (**Fig. 5B**), Hets showed reduced sociability (less time investigating the novel conspecific compared to WTs) during both trials (**Fig. 5C**), though still exhibiting social preference (**Fig. 5D**). This is due to reduced investigation time overall, as Hets spent more time in the center chamber (**Fig.5E**). These findings, coupled with reduced entries into the social investigation zone (**Fig. 5F**), indicate reduced sociability in Hets.

Deficits in sociability may be due to reduced motivation to engage with a social partner. Social motivation requires both social reward circuits and social orienting circuits (i.e., attending to a social stimulus when presented) (Chevallier et al., 2012). Therefore, we used data from an adapted and extended social operant paradigm (Martin and Iceberg, 2015), to understand the effect of MYT1L loss on social motivation directly and parse these two possibilities. We adapted

standard operant conditioning (**Fig. 5G, H**) to assess social motivation by rewarding nosepokes with an opportunity for transient social interaction (**Fig. 5I-L**). Social reward seeking is quantified by increasing the number of nosepokes required (work) to elicit each reward, and in parallel the animal's social orienting can be assessed by tracking its behavior. Hets were normal on learning the task, including day to reach criteria based on correct to incorrect nosepokes (**Fig. 5M**) and appeared to show normal social reward-seeking defined by the maximum number (breakpoint) of correct nosepokes made for a reward (**Fig. 5N**). However, during training male Hets achieved fewer social rewards compared to WT males (**Fig. 5O**) despite exhibiting a comparable number of correct nosepokes (**Fig. 5P**). This suggested the Het males continued to poke despite the presentation of a social reward. Indeed, we found that Het males tended to spend less time at the door during a reward (**Fig. 5Q**) and showed a significant decrease in overall time in the interaction zone (**Fig. 5R**). This reduction is not secondary to increased activity levels of male Hets as both males and female Hets show increased distance traveled (**Fig. 5S**). Together, these data indicate that Het males failed to cease nosepoking and orient to a social stimulus at the WT rate, indicating a male specific deficit in social orienting.

2.3 Discussion

Here, I described the generation of the first mouse model for MYT1L Syndrome. I confirmed MYT1L haploinsufficiency in Het mice by molecular experiments and demonstrated that this mouse model recapitulates many aspects of human MYT1L Syndrome, including obesity, microcephaly, and behavioral anomalies in circuits related to ADHD and ASC. This mouse model will be an important resource for future pre-clinical studies, enabling potential therapy development for MYT1L Syndrome. In addition, this germline knockout mouse line can also offer great opportunities to understand long-term consequences of MYT1L loss in the mammalian brain.

MYT1L LoF studies using this mouse line will advance our understanding of MYT1L's functions in physiological conditions and during normal development, beyond what was previously learned by neuronal trans-differentiation systems.

2.4 Materials and Methods

2.4.1 Human subjects

All procedures with human subjects were approved by the Washington University Institutional Review Board (201603131).

2.4.2 Animal models

All procedures using mice were approved by the Institutional Care and Use Committee at Washington University School of Medicine and conducted in accordance with the approved Animal Studies Protocol. All mice used in this study were bred and maintained in the vivarium at Washington University in St. Louis in individually ventilated (36.2 x 17.1 x 13 cm) or static (28.5 x 17.5 x 12 cm; post-weaning behavior only) translucent plastic cages with corncob bedding and *ad libitum* access to standard lab diet and water. Animals were kept at 12/12-hour light/dark cycle, and room temperature (20-22°C) and relative humidity (50%) were controlled automatically. For all experiments, adequate measures were taken to minimize any pain or discomfort. Breeding pairs for experimental cohorts comprised *Myt1l* Hets and wild type C57BL/6J mice (JAX Stock No. 000664) to generate male and female *Myt1l* Het and WT littermates. For embryonic ATAC-seq, RNA-seq, and EdU labeling, *Myt1l* Het x Het breeding pairs were used to generate *Myt1l* WT, Het and homozygous mutant littermates. Animals were weaned at P21, and group-housed by sex and genotype. Biological replicates for all experiments are sex and genotype balanced.

2.4.3 Method details

Generation of MYT1L knockout mice.

CRISPR-mediated homology-directed repair (HDR) was used to generate *Myt1l* S710fsX mice. A Cas9 gRNA was designed to target the 7th exon of the mouse MYT1L gene (seq: 5' GCTCTTGCTACACGTGCTACNGG 3'), similar to where a patient specific heterozygous *de novo* mutation defined by our clinical colleagues in a human case with ASC (c.2117dupG). Cutting efficiency of reagents and homologous recombination was confirmed in cell culture. Then validated gRNA and Cas9 protein (IDT) were electroporated into fertilized C57BL6/J oocytes along with single stranded oligonucleotides carrying homology to the targeted region and the G mutation as well as blocking for the other strand to prevent homozygous mutation and presumptive embryonic lethality of founders. Eggs were cultured for 1-2 hours to confirm viability, then transferred to pseudopregnant surrogate dams for gestation. Pups were then screened for the targeted allele by amplicon PCR with mutation flanking primers followed by Illumina sequencing. Founders carrying the appropriate allele were then bred with wild type C57BL/6J mice (JAX Stock No. 000664) to confirm transmission. F1 pups from the lead founder were genotyped by sequencing as above, then bred to generate experimental animals. Subsequent genotyping at each generation was conducted utilizing allele specific PCR using the MYT1L mutant primers and control primers, amplified using Phusion and the following cycling conditions: 98°C for 3 min, 98°C for 10 s, 61°C for 20 s, 72°C for 20 s, repeat 2-4 for 35 cycles, 72°C for 5 min, and hold at 4°C.

RNA extraction and RT-qPCR

Mice brains or cortex were dissected out at different developmental stages and homogenized in lysis buffer (10 mM Tris-HCl, pH 7.4, 10 mM NaCl, 3 mM MgCl2, 0.1% IGEPAL

CA-630, 0.1% Rnase inhibitor) on ice. Then lysates were mixed with Trizol LS and chloroform. After centrifugation, RNA was extracted from the aqueous layer with Zymo RNA Clean and ConcentratorTM-5 kit. cDNA libraries were prepared using qScript cDNA synthesis Kit (QuantaBio). RT-qPCR were performed using SYBR Green Master Mix (Thermo Fisher) on QuantStudio 6 Flex Real Time PCR System using primers in the **Key Resource Table** (**Appendix**). We normalized cycle counts to Gapdh or β-actin and calculated normalized relative gene expression using ΔΔCT. To compare MYT1L mRNA expression between genotypes, we put 6 WT and 8 Het brains into qPCR procedure. To understand MYT1L expression in human brain, we acquired normalized RNA-seq RPKM values of MYT1L in primary somatosensory cortex (S1C) from Allen Brain Atlas BrainSpan dataset (http://www.brainspan.org/) and plotted MYT1L mRNA temporal expression in R.

Western Blot

Mice brains or cortex were dissected out at different developmental stages and homogenized in lysis buffer (50 mM Tris-HCl, pH 7.4, 100 mM NaCl, 3 mM MgCl2, 1% IGEPAL CA-630, 10 mM NaF, 10 mM Na3Vo4 with Protease inhibitors). After centrifugation, supernatants were collected, and protein concentration was measured by BCA assay. For each sample, 20 µg of protein was run on the 7.5% BioRad precast gel and transferred to the PVDF membrane. We blocked the membrane using TBST with 3% BSA for 2 hours at room temperature (RT). Then, the membrane was incubated with anti-MYT1L (1:500, 25234-1-AP, Proteintech) and anti-GAPDH (1:5000, G8795, Sigma) primary antibodies overnight at 4°C and then incubated with HRP conjugated anti-Mouse (1:2000, 1706516, BioRad) and anti-goat (1:2000, AP307P, Millipore) for one hour at RT. After washing, the membrane was developed in BioRad ECL Western Blotting Substrates and imaged with myECL Imager (Thermo Fisher). Fluorescent intensity was measured

by ImageJ and MYT1L expression was normalized to GAPDH. To compare MYT1L protein expression between genotypes, we put 3 WT and 4 Het brains into Western Blot procedure.

Immunofluorescence

Mice brains were dissected out at different developmental stages and fixed in 4% paraformaldehyde (PFA) overnight at 4°C. After gradient sucrose dehydration and O.C.T. compound embedding, brains were sectioned using Leica Cryostat (15 μm for E14 brains and 30 μm for postnatal brains). Antigen retrieval was performed by boiling sections in 95°C 10 nM sodium citrate (pH 6.0, 0.05% Tween-20) for 10 mins. Then, sections were incubated in the blocking buffer (5% normal donkey serum, 0.1% Triton X-100 in PBS) at RT for 1 hour. Primary antibodies, including anti-MYT1L (1:500, 25234-1-AP, Proteintech), anti-MAP2 (1:200, #188044, SYSY), anti-SOX2 (1:200, sc-17320, Santa Cruz), anti-TBR2 (1:400, AB15894, Millipore), anti-Ki-67 (1:500, #14-5698-82, Invitrogen), anti-CTIP2 (1:500, ab18465, Abcam), anti-BRN2 (1:500, sc-393324, Santa Cruz), anti-NEUN (1:500, #12943, Cell Signaling), anti-GFAP (1:500, ab53554, Abcam), anti-OLIG2 (1:200, AF2418, R&D Systems), and anti-TBR1 (1:500, ab31940, Abcam) were used to detect different cell markers. Next, sections were incubated in fluorescence conjugated secondary antibodies, including donkey anti-rabbit (Alexa 488, 546, and 647, Invitrogen), donkey anti-mouse (Alexa 546, Invitrogen), donkey anti-chicken (Alexa 488, Jackson ImmunoResearch), donkey anti-rat (Alexa 488 and 647, Invitrogen), and donkey anti-goat (Alexa 488 and 647, Jackson ImmunoResearch) at 1:500 dilution for 2 hours in RT. Images were captured under Zeiss Confocal Microscope or Zeiss Axio Scan Slide Scanner and cell counting was performed using ImageJ. In order to compare cell numbers of different cell types across genotypes, we had 5 WT, 6 Het, and 5 KO E14 brains for cell counting experiments. And we had 6 WT, 6 Het, and 5 KO E14 brains to quantify the Ki-67 positive cells.

Sanger Sequencing

Genomic DNA (gDNA) was extracted from mouse tissue by Qiagen Blood and Tissue Kit. A 2.2kb gDNA fragment flanking the G duplication site was amplified using the primers **Key Resource Table** (**Appendix**), Phusion, and following program: 98°C for 2 min, 98°C for 10 s, 60°C for 20 s, 72°C for 1 min, repeat 2-4 for 30 cycles, 72°C for 5 min, and hold at 4°C. PCR products were purified with QIAquick PCR Purification Kit and submitted for sanger sequencing at Genewiz. We used Snapgene to check and visualize sanger sequencing results.

Illumina Sequencing

gDNA and cDNA library from mice brains was generated as described in the above sections. To prepare sequencing libraries, we performed two-step PCR to first tag 200bp DNA fragments flaking the mutation site with Illumina adapters (Taq, primers seen **Key Resource Table** (**Appendix**), PCR program: 94°C for 3 min, 94°C for 10 s, 58°C for 20 s, 68°C for 1 min, repeat 2-4 for 30 cycles, 68°C for 5 min, and hold at 4°C) and then add unique index to individual samples (Taq, primers seen supplemental tables, PCR program: 98°C for 3 min, 98°C for 10 s, 64°C for 30 s, 72°C for 1 min, repeat 2-4 for 20 cycles, 72°C for 5 min, and hold at 4°C). Final PCR products were purified by gel extraction using Qiagen Gel Extraction Kit and submit for 2×150 Illumina sequencing to CGSSB at Washington University School of Medicine. For each sample, we were able to get ~80,000 reads. We conducted quality control on raw reads using FastQC. Then, reads were trimmed by Trimmomatic software and aligned to the mouse genome by STAR. We used VarScan and Samtools to determine the percentage of the mutation in gDNA (n = 8) and cDNA (n = 8) samples.

Nissl Staining

Following perfusion with 4% paraformaldehyde, the brains were removed, weighed (WT n = 5, Het n = 6), sectioned coronally using a vibratome at 70 μm, and then mounted onto gelatin coated slides (WT n = 8, Het n = 9). Sections were then rehydrated for 5 minutes in xylene, xylene, 100% ethanol, 100% ethanol, 95% ethanol, 70% ethanol, and deionized water. Using 0.1% cresyl violet at 60°C, sections were stained for two hours and rinsed with two exchanges of deionized water. Differentiation began with 30 second rinses in 70% ethanol, 80% ethanol, and 90% ethanol. Next, a two-minute rinse in 95% ethanol was done, checking microscopically for a clearing background. This was followed by a 30-second rinse in two exchanges of 100% ethanol, a 15-minute rinse using 50% xylene in ethanol, and a 1-hour rinse of xylene. Finally, the sections were mounted and coverslipped using DPX mountant. Whole and regional volumes were outlined by a rater blind to treatment using Stereoinvestigator Software (v 2019.1.3, MBF Bioscience, Williston, Vermont, USA) running on a Dell Precision Tower 5810 computer connected to a Qimaging 2000R camera and a Labophot-2 Nikon microscope with electronically driven motorized stage.

In vivo Magnetic Resonance Imaging (MRI): data acquisition.

All animal experiments were approved by Washington University's Institutional Animal Care and Use Committee. MRI experiments were performed on a small-animal MR scanner built around an Oxford Instruments (Oxford, United Kingdom) 4.7T horizontal-bore superconducting magnet and equipped with an Agilent/Varian (Santa Clara, CA) DirectDrive™ console. Data were collected with a laboratory-built, actively-decoupled 7.5-cm ID volume coil (transmit)/1.5-cm OD surface coil (receive) RF coil pair. Mice were anesthetized with isoflurane/O_2 (1.2% v/v) and body temperature was maintained at 37±1°C *via* circulating warm water. Mouse respiratory rate (50-70 breaths/minutes) and body temperature (rectal probe) were monitored with a Small Animal Instruments (SAI, Stony Brook, NY) monitoring and gating unit.

T2-weighted transaxial images (T2W) were collected with a 2D fast spin-echo multi-slice (FSEMS) sequence: echo train length=4, kzero=4, repetition time (TR)=1.5 s, effective echo time (TE)=60 ms; field of view (FOV)=24 x 24 mm^2, matrix size =192 x 192, slice thickness=0.5 mm, 21 slices, 4 averages. Co-registered T1-weighted images (T1W) were collected with a 2D spin-echo multi-slice (SEMS) sequence: TR=0.8 s, TE=11.3 ms, 2 averages.

Diffusion Tensor Imaging (DTI) measures the directional water movement along and perpendicular to axons (fractional anisotropy: FA) as a measure of white-matter integrity, and the same images can be used for structural assessments. DTI data were collected using a multi-echo, spin-echo diffusion-weighted sequence with 25-direction diffusion encoding, max b-value=2200 s/mm^2. Two echoes were collected per scan, with an echo spacing of 23.4 ms, and combined offline to increase signal-to-noise ratio (SNR), resulting in a SNR improvement of 1.4x compared with a single echo. Other MR acquisition parameters were TR=1.5 s, TE=32 ms, length of diffusion-encoding gradients (δ)=6 ms, spacing between diffusion gradients (Δ)=18 ms, FOV = 24 mm x 24 mm, matrix size = 192 x 192, slice thickness=0.5 mm, 21 slices, 1 average. The total acquisition time was approximately 2 hours and 5 minutes.

DTI Data Analysis.

DTI datasets were analyzed in MatLab (The MathWorks®, Natick MA). Following zero-padding of the k-space data to matrix size 384 x 384, the data were Fourier-transformed and the images from the two spin echoes were added together. A 3 x 3 Gaussian filter (Sigma = 0.7) was applied and the resulting images were fit as a mono-exponential decay using the standard MR diffusion equation (Stejskal and Tanner, 1965):

$$S/S_0 = \exp[(-\gamma^2 G^2 \delta^2 (\mathbf{\Delta} - \delta/3) D)],$$

in which S is the diffusion-weighted signal intensity, S_0 the signal intensity without diffusion weighting, γ is the gyromagnetic ratio, G is the gradient strength, and D is the diffusion coefficient. Eigenvalues (λ_1,λ_2,λ_3) corresponding to the diffusion coefficients in three orthogonal directions were calculated and parametric maps of apparent diffusion coefficient (ADC), axial diffusion (D_{axial}), radial diffusion (D_{radial}), and fractional anisotropy (FA) were calculated according to standard methods (Basser and Pierpaoli, 2011; Mori, 2007). Parametric maps were converted into NifTI (.nii) files for inspection and segmentation in ITK-SNAP (www.itksnap.org). We ended up analyzing 8 WT mice and 6 Het mice.

Developmental assessment.

During the first three weeks postnatal, we assessed the *Myt1l* Het and WT littermates for signs of gross developmental delay and communicative delay, which are universal in MYT1L deletion patients (Blanchet et al., 2017). To evaluate gross development, the mice were weighed daily from P5 - P21, and evaluated for physical milestones of development including pinna detachment by P5 and eye opening by P14. While human language cannot be explored in mice, vocal communication behavior is conserved across taxa (Ehret, 1980). Mouse pups produce isolation calls as a way to attract the dam for maternal care (Haack et al., 1983), thus it is one of the earliest forms of social communication we can examine in mice. This behavior also has a developmental trajectory, beginning just after birth, peaking during the first week postnatal and disappearing around P14, making it useful for examining delay in early social circuits. Ultrasonic vocalizations (USVs) were recorded on P5, P7. P9 and P11 following our previous methods (Maloney et al., 2018a). Briefly, the dam was removed from the nest and the litter placed in a warming cabinet. The surface temperature of each pup was recorded (HDE Infrared Thermometer; Het: *M*=35.4°C, *SD*=0.90; WT: *M*=35.2°C, *SD*=1.16), and then the pup was placed in an empty

cage (28.5 x 17.5 x 12 cm) in a sound-attenuating chamber. USVs were recorded for three minutes using an Avisoft UltraSoundGate CM16 microphone, Avisoft UltraSoundGate 116H amplifier, and Avisoft Recorder software (gain = 3 dB, 16 bits, sampling rate = 250 kHz). The pup was then removed, weighed, tissue collected for genotyping (P5 only), and returned to the nest. Following recording of the last pup, the dam was returned to the nest. Frequency sonograms were prepared from recordings in MATLAB (frequency range = 25 kHz to 120 kHz, FFT size = 512, overlap = 50%, time resolution = 1.024 ms, frequency resolution = 488.2 Hz). Individual syllables and other spectral features were identified and counted from the sonograms as previously described (Holy and Guo, 2005; Rieger and Dougherty, 2016).

Open field

Locomotor ambulation was measured at P30 to assess activity, exploration, and anxiety-like levels in the open field assay similar to our previous work (Maloney et al., 2018b). Specifically, the behavior of each mouse was evaluated over a 1-hr period in a translucent acrylic apparatus measuring 59 x 39 x 22 cm, housed inside a custom sound-attenuating chamber (70.5 x 50.5 x 60 cm), under approximately 9 lux illumination (LED Color-Changing Flex Ribbon Lights, Commercial Electric, Home Depot, Atlanta, GA). A CCTV camera (SuperCircuits, Austin, TX) connected to a PC computer running the software program ANY-maze (Stoelting Co., Wood Dale, IL; http://www.anymaze.co.uk/) tracked the movement of the mouse within the apparatus to quantify distance traveled, and time spent in and entries into the center 50% and outer perimeter zones. The apparatus was cleaned between animals with a 0.02% chlorhexidine diacetate solution (Nolvasan, Zoetis, Parsippany-Troy Hills, NJ).

Pose estimation (DeepLabCut (Mathis et al., 2018) and machine learning classification (SimBA (Nilsson et al., 2020)) were used to further quantify behaviors of the mice in videos

recorded during the open field test. Specifically, we used DeepLabCut to estimate the pose of eight body parts of the mice, including nose, left ear, right ear, center, lateral left, lateral right, tail base, and tail end. A random subset of frames from all 41 videos were used for the network training. The trained network was then applied to all videos, yielding pose tracking files. The video and the tracking file of a Het female mouse were input to SimBA to build classifiers for jumping, facial grooming, and body/tail grooming. A region of interest (ROI) defined as a rectangle covering the center area of the open field was appended to the machine learning features extracted from the tracking file. Then the training video was annotated for interesting behaviors using the SimBA event-logger. Random forest classifiers were trained using default hyperparameters, and classifier performances were evaluated. We set the discrimination threshold of jumping, facial grooming and body/tail grooming to 0.8, 0.444, and 0.521 respectively. The minimum behavior bout length (ms) for all behaviors was set to 200. In the end, the classifiers were applied to analyze all the videos. Facial grooming and body/tail grooming were combined for analyses. The descriptive statistics for each predictive classifier in the project, including the total time, the number of frames, total number of 'bouts', mean and median bout interval, time to first occurrence, and mean and median interval between each bout, were generated.

Force-plate actometer

At P36, the presence of stereotyped movements indicative of self-grooming (bouts of low mobility or movement during those bouts) and presence of tremor resulting from possible demyelination was assessed in the force-plate actometer (FPA), as previously described (Reddy et al., 2012; Tischfield et al., 2017). The custom made FPA consisted of a carbon fiber/nomex composite material load plate measuring 24 × 24 cm surrounded by a clear polycarbonate cage (15 cm high) with a removable clear polycarbonate top perforated with ventilation holes, and housed

in a sound-attenuating cabinet measuring 70.5 x 50.5 x 60 cm. Force was measured by summing the signal from four transducers, which is then expressed as a percentage of body weight. Grooming only takes place during low mobility bouts, as previously defined (Reddy et al., 2012) and validated (Tischfield et al., 2017). Raw data was acquired with a DOS-based Free Pascal program and further processed using custom MATLAB scripts (Fowler et al., 2001). To identify any tremor, each force time series was Fourier transformed to identify unique frequencies and plotted as a continuous function or power spectra. Tremor was identified as the frequency at peak power.

Barnes maze

Spatial learning and memory were evaluated in the Barnes maze using methods adapted from previous work (Pitts, 2018). The Barnes maze apparatus consisted of a circular white acrylic platform measuring 122 cm in diameter, with 20 equally spaced holes (5 cm in diameter) around the perimeter 6.35 cm from the edge, elevated 80 cm from the floor. The maze was brightly lit with overhead lighting, and extra maze cues were used to aid learning. Testing comprised two acquisition trials separated by 45 minutes on each of 5 consecutive days. During acquisition trials, an escape box measuring 15.2 x 12.7 cm with an inclined entry was attached to the maze underneath one hole location (three escape locations were counterbalanced across mice). Prior to the first trial on the first day, each mouse was placed in the escape hole for 30 seconds covered by a clear acrylic tube. During each trial, a mouse was placed in the center of the maze facing a random direction, 75 dB white noise sounded until the mouse entered the escape box, which ended the trial. Each mouse was allowed to remain in the escape box for 30 seconds. If the mouse failed to enter the escape box, the trial would end after a maximum of three minutes and the mouse would be placed in the escape box for 30 seconds. On the sixth day, a three minute probe trial was

conducted to assess each animal's memory for the previously learned location of the escape box. The escape box was removed, and a mouse was placed in the center of the maze facing a random direction, and 75 dB white noise sounded until the end of the trial. A digital USB 2.0 CMOS Camera (Stoelting Co., Wood Dale, IL) connected to a PC computer running the software program ANY-maze (Stoelting Co., Wood Dale, IL; http://www.anymaze.co.uk/) tracked the movement of the mouse within the apparatus to quantify distance traveled, frequency and duration of visits to the escape box and to incorrect holes. All males were tested first, followed by the females. The apparatus was cleaned between animals with a 0.02% chlorhexidine diacetate solution (Nolvasan, Zoetis, Parsippany-Troy Hills, NJ).

Social operant

Social motivation, including social reward seeking and social orienting (Chevallier et al., 2012), was evaluated from P48-P60 using a social operant task adapted and extended from previous methods (Martin and Iceberg, 2015; Martin et al., 2014), adding continuous tracking to measure social reward seeking and social orienting in parallel. Standard operant chambers (Med Associates) enclosed in sound-attenuating chambers (Med Associates) were modified. A clear acrylic conspecific stimulus chamber (10.2 x 10.2 x 18.4 cm; Amac box, The Container Store) was attached to the side, separated from the operant chamber proper by a door opening (10.2 x 6 cm) with stainless steel bars (spaced 6mm apart), centered between the nosepoke holes. A 3D printed filament door was attached via fishing wire to a motor (Longruner) controlled by an Arduino (UNO R3 Board Atmega328P) connected to the Med Associates input panel. The chamber included a red cue light that illuminated at the beginning of the test trial and remained illuminated until the test trial ended. The rest of the chamber was illuminated with a puck light (Honwell) to achieve 54 lux. The operant chamber bottom tray was filled with one cup of fresh corn cob bedding, which was

replaced between mice. Operant chambers and stimulus chambers were designated for males or females throughout the experiment. The operant chambers were cleaned with 70% ethanol and the stimulus chambers were cleaned with 0.02% chlorhexidine diacetate solution (acrylic; Nolvasan, Zoetis) between animals. One of the operant chamber holes was designated the "correct" hole, and the other the "incorrect" hole, which were counterbalanced across groups. A nosepoke into the correct hole triggered illumination of a cue light within that hole and the raising (opening) of the door between the operant and stimulus chambers. A nosepoke into the incorrect hole did not trigger an event. The experimental and stimulus animals were allowed to interact across the bars for 12 sec (social reward) and then the door was lowered (shut) and the correct hole cue light turned off. The operant chambers were connected to a PC computer via a power box (Med Associates). MED PC-V software quantified nosepokes as "correct", "incorrect", and "rewards" to measure social reward seeking behavior as part of social motivation. CCTV cameras (Vanxse) were mounted above the chambers and connected to a PC computer via BNC cables and quad processors. Any-Maze tracking software (Stoelting Co., Wood Dale, IL; http://www.anymaze.co.uk/) was used to track the experimental and stimulus animals' behavior to quantify distance traveled, and time spent in and entries into the social interaction zone (6 x 3 cm zone in front of the door in each the operant and stimulus chamber). This allowed us to quantify the social orienting aspect of social motivation, defined as the experimental animal entering and spending time in the social interaction zone. Custom Java tools and SPSS syntax were used to align the Any-Maze tracking data with the timing of rewards in the Med Associates text data to extract presence or absence of each animal within the interaction zones during each second of every reward.

The operant paradigm comprised habituation, training, and testing trials. For all trials, sex- and age-matched, novel C57BL/6J mice served as conspecific stimulus mice. All mice,

experimental and stimulus, were group housed by sex during the entirety of the operant paradigm. The stimulus mice were loaded into and removed from the stimulus chambers prior to the placement and after removal of the experimental mice into the operant chambers, respectively, to prevent the experimental animals from being in the chambers without a conspecific stimulus partner. Habituation consisted of a 30 minute trial on each of two consecutive days, during which the door remained opened, and the nosepoke holes were shifted to be inaccessible to prevent any nose-poking prior to training. This allowed the experimental mice to acclimate to the chamber and the presence of a stimulus partner in the adjoining chamber. Training consisted of 1-hr trials during which the fixed ratio 1 (FR1) reinforcement schedule was used to reward the mouse with a 12-sec social interaction opportunity following one correct nosepoke. During the 12-sec reward period, any additional correct nosepokes did not result in another reward. Each mouse received at least three days of FR1, after which achievement of learning criteria moved the mouse on to testing. Ten days of FR1 without reaching criteria resulted in "non-learner" status. Learning criteria included at least 40 correct nosepokes, a 3:1 correct:incorrect ratio, and at least 65% of rewards including a social interaction (defined as both experimental and stimulus mice in their respective social interaction zones simultaneously for at least 1 sec of the reward). Testing comprised a 1-hr trial on each of 3 consecutive days, during which the fixed ratio 3 (FR3) reinforcement schedule was used to reward the mouse with a 12-sec social interaction opportunity following three consecutive correct nosepokes. FR3 served to increase social reward seeking effort required to receive a social reward. Following completion of FR3 testing, breakpoint testing was conducted on the following day during a 1-hr trial. To measure the breakpoint, or maximum nosepokes or effort the animal would exhibit for a social reward, the progressive ratio 3 (PR3) reinforcement schedule was used to reward the mouse with a 12-sec social interaction opportunity following a

progressive increase in required correct nosepokes by 3 (e.g. 3, 6, 9, 12, etc). Due to the limited number of testing chambers and the length of testing daily, we restricted the number of animals to 17 WTs (10 females, 7 males) and 19 Hets (10 females, 9 males) in order to fit all runs into one day. Task validation data was derived from a cohort of 40 male (n=20) and female (n=20) C57BL/6J adult mice (~P60), which served as either experimental mice (n=20) that received a social partner interaction as a reward or control mice (n=20) that received only the opening of a door as a reward. The testing procedure was as stated above, except that all mice received four consecutive PR3 testing days to assess reliability of performance within individuals.

Tube test of social dominance

Mice begin to develop social hierarchy behaviors at 6 weeks of age under laboratory conditions, which result in dominance ranks within their social groups (Hayashi, 1993). The tube test of social dominance was used to assess the social hierarchy behavior of the mice as previously described (Maloney et al., 2018b). Briefly, a pair of sex-matched *MYT1L* Het and WT mice were gently guided into a clear acrylic tube measuring 30 cm in length and 3.6 cm in diameter from either end. When the mice met in the center, a divider was lifted and the time for one mouse to back out of the tube as the bout loser/submissive partner up to 2 min was recorded. This was repeated once across three consecutive days for each animal with a novel sex-matched partner. Prior to testing, each mouse was habituated to the tube by gently guiding it through the tube from either end across two consecutive days. The tube was cleaned with 0.02% chlorhexidine diacetate solution (Nolvasan, Zoetis, Parsippany-Troy Hills, NJ) between each pair. Each trial was video recorded and subsequently scored for the dominant and submissive partner of each bout. Because testing required sex-matched genotype-mixed pairs, only a subset of 17 WTs (9 females, 8 males) and 17 Hets (9 females and 8 males) were used.

Prepulse inhibition/startle

Sensorimotor gating and reactivity were assessed at P94 in the prepulse inhibition (PPI) /acoustic startle task as previously described (Dougherty et al., 2013). Briefly, PPI (response to a prepulse plus the startle pulse) and acoustic startle to a 120 dBA auditory stimulus pulse (40 ms broadband burst) were measured concurrently using computerized instrumentation (StartleMonitor, Kinder Scientific). A total of 65 trials were presented. Twenty startle trials were presented over a 20 min test period, during which the first 5 min served as an acclimation period when no stimuli above the 65 dB white noise background were presented (non-startle trials). The session began and ended by presenting 5 consecutive startle (120 db pulse alone) trials unaccompanied by other trial types. The middle 10 startle trials were interspersed with PPI trials, consisting of an additional 30 presentations of 120 dB startle stimuli preceded by prepulse stimuli of 4, 12, or 20 dB above background (10 trials for each PPI trial type). A percent PPI score for each trial was calculated using the following equation: %PPI = 100 × (startle pulse alone − prepulse + startle pulse)/startle pulse alone. The apparatus was cleaned with 0.02% chlorhexidine diacetate solution (Nolvasan, Zoetis, Parsippany-Troy Hills, NJ).

Fear conditioning

To assess associative memory to an aversive stimuli, we evaluated our mice in the fear conditioning paradigm as we previously described (Maloney et al., 2019a). In this task, freezing behavior was quantified as a proxy for the fear response. Briefly, the apparatus consisted of an acrylic chamber (26 x 18 x 18 cm) with a metal grid floor, an LED cue light and an inaccessible peppermint odorant that is housed in a sound-attenuating chamber (Actimetrics). The cue light turned on at the start of each trial and remained illuminated. The procedure comprised a 5-minute training session, an 8-minute contextual memory test, and a 10 minute cued memory test across 3

consecutive days. During training an 80 dB tone (white noise) sounded for 20 sec at 100 sec, 160 sec and 220 sec. A 1.0 mA shock (unconditioned stimulus; UCS) was paired with the last two sec of the tone (new conditioned stimulus; CS). Baseline freezing behavior was measured during the first two minutes and the freezing behavior as the conditioned response (CR) to the presentation of tone and foot shock was measured during the last three minutes. Freezing behavior was quantified through the computerized image analysis software program FreezeFrame (Actimetrics, Evanston, IL). During contextual conditioning testing on day 2, no tones or shocks were presented allowing for the evaluation of freezing behavior (CR) in response to the contextual cues associated with the shock stimulus (UCS) from day 1. During cued conditioning testing on day 3 the context of the chamber was changed to an opaque acrylic-walled chamber containing a different (coconut) odorant. The 80 dB tone (CS) began at 120 sec and lasted the remainder of the trial. During the first two min baseline freezing behavior to the new context (pre-CS) was measured. During the remaining eight min, freezing behavior (CR) in response to the auditory cue (CS) associated with the shock stimulus (UCS) from day 1 was quantified. Sensitivity to footshocks was evaluated following testing as previously described (Maloney et al., 2019b), and no differences were observed between genotypes (data not shown).

Social approach

The three-chamber social approach task was used to test sociability and social novelty preference as previously described (Maloney et al., 2018b). Sociability is defined here as the preference to spend time with a novel conspecific over a novel empty cup. Social novelty is defined as the preference to spend time with a novel versus familiar conspecific. The clear acrylic apparatus measuring 60 x 39 x 22 cm is divided into three equal chambers each measuring 19.5 x 39 x 22 cm with two doors of 5 x 8 cm. During testing, an acrylic lid with four air holes is placed on top

of the apparatus. Two stainless steel cages (Galaxy Pencil/Utility Cup, Spectrum Diversified Designs, Inc) measuring 10 cm tall and 10 cm in diameter with vertical bars served as conspecific stimulus cages and allowed for controlled, minimal contact interactions between experimental and stimulus mice. The apparatus is placed inside a custom-built sound-attenuating chamber (70.5 × 50.5 × 60 cm). Testing is completed under red light illumination of ~11 lux provided by LED Flex Ribbon Lights (Commercial Electric, Home Depot). Video is captured by a CCTV camera (SuperCircuits) mounted in the top of each sound-attenuated chamber. A PC computer with the program ANY-maze (Stoelting Co., Wood Dale, IL; http://www.anymaze.co.uk/) recorded video and live tracked the nose, body and tail of the test mouse to produce variables for analysis: distance traveled, time spent in and entries into each chamber and investigation zone. An investigation zone is the area 2 cm outward from the perimeter of each conspecific cage. An entry into the investigation zone requires the nose-point to be within the zone, constituting a purposeful interaction by the test mouse. The social preference score was calculated as (time in social / (time in social + time in empty))*100. The novelty preference score was calculated as (time in novel / (time in novel + time in familiar))*100. Statistical analysis was as previously described (Nygaard et al., 2019).

Testing consists of four, consecutive 10-minute trials. Trials 1 and 2 habituate the test mouse to the center chamber and the whole apparatus, respectively. At the completion of trial 2 the mouse is gently guided back to the center chamber and doors closed. Trials 3 and 4 test sociability and social novelty preference, respectively. In trial 3, an unfamiliar, sex-matched conspecific (C57BL/6J) in a conspecific cage is added to one of outer chambers, and an empty conspecific cage is added to the other outer chamber. The conspecific cage locations were counterbalanced between groups. The test mouse was allowed to explore freely, and at the end of

the trial was guided back to the center chamber. During trial 4, a new novel conspecific mouse (C57BL/6J) is added to the empty cage, the conspecific mouse from trial 3 remains in the same cage to serve as the familiar stimulus. After each test, the apparatus is cleaned with 0.02% chlorhexidine diacetate solution (Nolvasan, Zoetis). The conspecific cages were cleaned with 70% ethanol solution.

Spontaneous alternation T-maze

The spontaneous alternation T-maze was used to assess perseverative exploratory behavior with procedures adapted from our previous work (Maloney et al., 2018b). The apparatus is made of grey acrylic walls with a clear acrylic floor (Noldus). White paper is adhered to the underside of the floor to create distinction between coat color and the apparatus for contrast. A Start chamber (20 x 8.7 cm) is connected to two radiating arms (25 x 8.7 cm), each separated by a door that closes from the floor up. The doors for each arm and start chamber are controlled automatically by Ethovision XT 14 (Noldus) through air compression provided by an ultra-quiet air compressor (California Air Tools) located in an adjacent room. Video is captured by an IR camera (Basler acA1300) mounted above the apparatus, which is connected to a PC computer. Testing is completed in the dark with four IR LED lights (JC Infrared Illuminator) and consists of 10 consecutive trials. Prior to the start of the trial, the mouse is sequestered in the Start chamber for two minutes to habituate to this chamber. To begin the trial, the start door opens, and the mouse is free to explore. An arm choice is made when the whole body crosses the arm threshold located 11.1 cm beyond the door to the arm, and which triggers all doors to close, and the mouse is allowed to explore the chamber for 15 seconds. The door to that arm is then lowered, allowing the animal to move back to the Start chamber, triggering the closing of all doors. After 5s in the Start chamber, the doors all re-open, triggering the beginning of the next trial. If no arm choice is made after two

minutes, it is considered a non-choice trial, and the start of the next trial is triggered. Once all 10 trials are completed the mouse is returned to its home cage and the apparatus cleaned with 0.02% chlorhexidine diacetate solution (Nolvasan, Zoetis).

Tactile sensitivity assessment

Tactile sensitivity task assessed reflexive, mechanical sensitivity to a punctate stimulus (von Frey filaments), and was conducted as previously described (Maloney et al., 2018b). The testing apparatus consisted of a metal grid surface elevated 63.5 cm, which allowed access to the plantar surface of each animals' paws. Each animal was housed in an individual acrylic box (10 cm x 10 cm x 10 cm) open on the bottom and opaque on three sides to prevent visual cues between animals. All mice were acclimated to the testing room 30 min prior to habituation and testing. On days 1 and 2, all mice were habituated to the testing apparatus for 1 hour. On day 3, mice were allowed to acclimate to the testing apparatus for 30 minutes prior to start of testing. Eight different von Frey hair filaments (applying 0.04-2 g of force; North Coast Medical and Rehabilitation Products) were applied to the plantar surface of each animal's hind paw and withdrawal responses were recorded. Presentations started with the lowest filament strength (0.04 g) and increased to the maximum filament strength (2 g). Each filament was applied to the plantar surface of each hind paw five times, and the number of paw withdrawal responses was recorded as percentage of responses. To evaluate the changes in paw withdrawal responses to the whole range of filaments over the testing duration, the area of the curve (AUC) was calculated for each animal.

Weight, posture, and physical assessments

All mice from the second cohort were weighed continuously throughout the experiment, starting on P30, to assess obesity-related weight gain in the mice. In addition, on P86, the mice were assessed for posture and physical characteristics. Posture was assessed by picking up the

animal by the base of its tail and evaluating the splay of the forelimbs and hindlimbs. Normal posture was defined as splay of both forelimbs and hindlimbs. Abnormal posture was defined as any deviation from this, including hyperflexion or grasping of limbs. Posture was analyzed as a binary measure: normal splayed posture or abnormal posture. The physical examination consisted of assessment of the condition of eyes (presence of debris or cataracts), whiskers (full, partial, pruned), fur (matted or clean), skin (presence of dermatitis), nose (presence of drainage), and anus (presence of prolapse), as well as presence of any seizure-like activity induced by handling or tumors.

2.5 Acknowledgement

I thank Dr. Monica Sentamet and the Genome Engineering and Stem Cell Center (GESC) at Washington University in St. Louis for gRNA design and validation, Dr. Michael White and the transgenic services core for oocyte injection, Dr. Cheng Cheng, Dr. Lingchun Kong, Dr. Xiaoying Chen, Dr. Adam Clemens, Weijia Cao, Brant Swiney, Nicole Fuhler, Rena Silverman, Joelle Schneiderman for technical assistance, and Drs. Carla Yuede and David Wozniak for access to behavioral equipment, and the Mallinckrodt Institute of Radiology's Small Animal Magnetic Resonance Facility and Washington University Center for Cellular Imaging for technical support. Funding was provided by The Jakob Gene Fund, the Mallinckrodt Institute of Radiology at Washington University School of Medicine, McDonnell International Scholars Academy (J.C.), The Brain & Behavior Research Foundation (K.H.), and the NIH: (R01MH107515, R01MH124808 to JDD, and NIH 5UL1TR002345 (ICTS) and P50 HD103525 (IDDRC)).

2.6 Figures and Tables

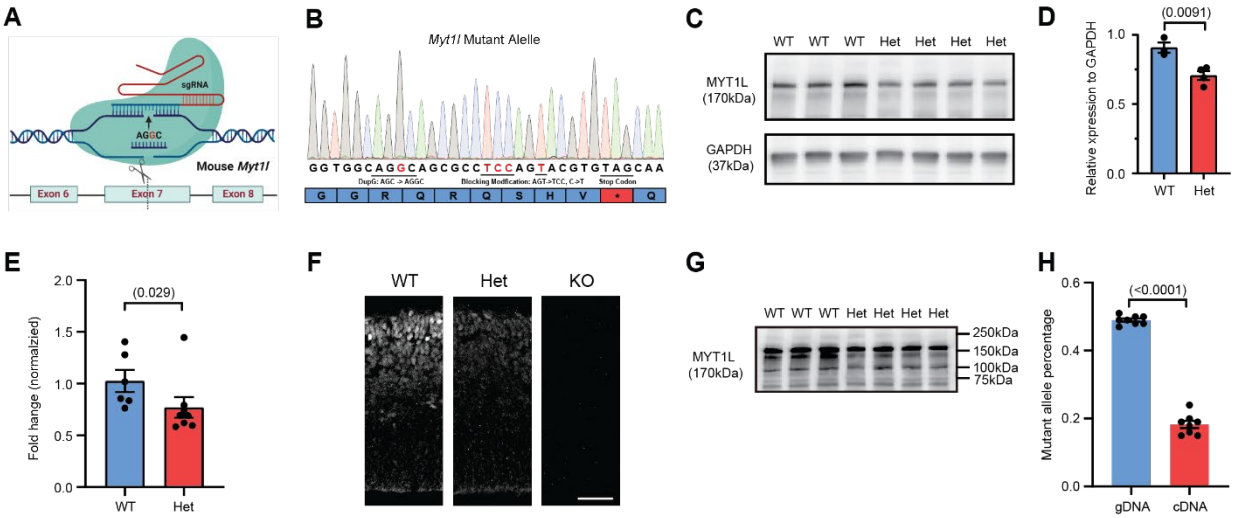

Figure 1: MYT1L frameshift mutation results in protein haploinsufficiency.

(A) Schematics for MYT1L KO mouse line generation. **(B)** Sanger sequencing of c.3035dupG mutation on MYT1L mutant allele. **(C, D)** Western blot on P1 whole brain lysates confirmed MYT1L protein reduction in Het mice. **(E)** RT-qPCR revealed *Myt1l* relative mRNA expression to *Gapdh* decreases in P1 Het whole brain lysates (WT n = 6, Het n = 7). **(F)** Immunofluorescence on E14 mouse cortex further validated antibody specificity and protein loss in *Myt1l* KO mice. **(G)** Long exposure of Western blot in **Fig. 1C** showed no truncated protein produced by *MYT1L* c.3035dupG mutation. **(H)** Illumina sequencing on gDNA and cDNA from P1 *Myt1l* Het mouse brain showed mutant allele-specific in cDNA (n = 8), consistent with nonsense mediated decay.

*Data were represented as mean ± SEM. Scale bars, 50 μm in **F**. See **Table S1** for statistical test details.*

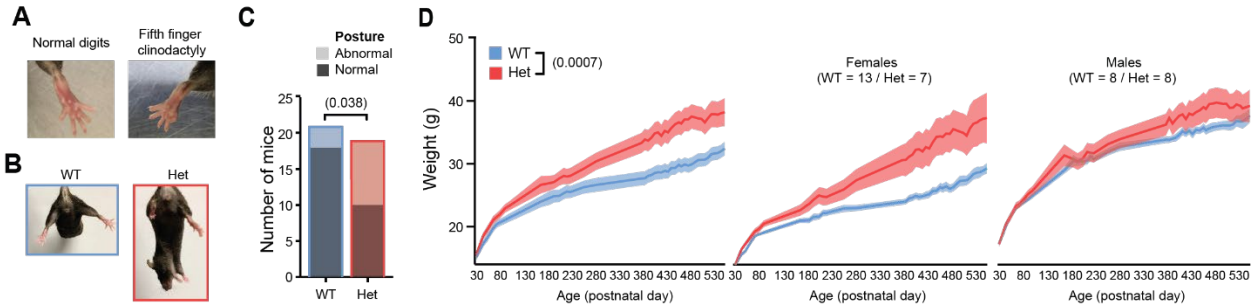

Figure 2: MYT1L frameshift mutation results in physical anomalies, and obesity.

(A) In physical examination, a subset of Het mice displayed fifth finger clinodactyly and **(B, C)** abnormal hindlimb posture. **(D)** Het mice weighed significantly more than WTs as adults, which was more pronounced in females.

*Data were represented as mean ± SEM. See **Table S1** for statistical test details.*

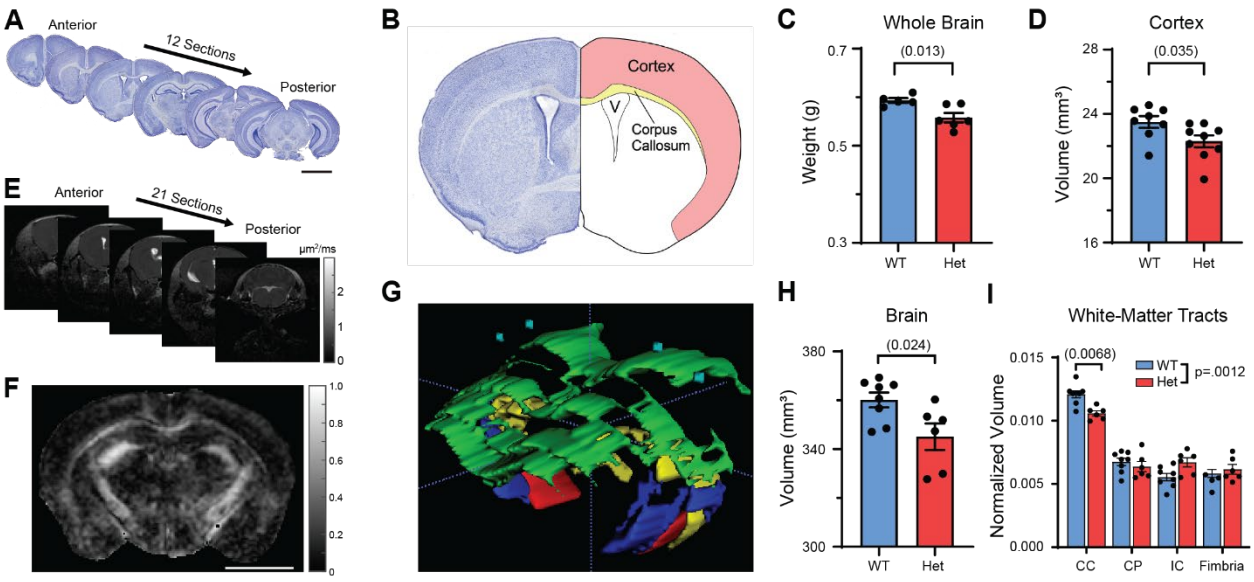

Figure 3: MYT1L haploinsufficiency causes microcephaly and white-matter thinning in corpus callosum.

(A) Sectioning strategy for Nissl staining. Scale bar, 3 mm. **(B)** Diagram of different brain structures examined. **(C)** Adult Het mice had decreased brain weight and **(D)** decreased cortical volume. **(E)** Coronal images acquired from DTI. **(F)** Fractional anisotropy (FA) map for visualization of white-matter tracts. Scale bar, 0.5 cm. **(G)** 3D reconstruction of different white-matter tracts via FA maps, including corpus callosum (CC, green), cerebral peduncle (CP, red), internal capsule (IC, blue), fimbria (yellow), and cortex (blue). **(H)** DTI recapitulated smaller brain phenotype in Het mice. **(I)** Histogram showed adult Het mice had decreased corpus callosum volume. Data were normalized to brain volume.

*Data were represented as mean ± SEM. See **Table S1** for statistical test details.*

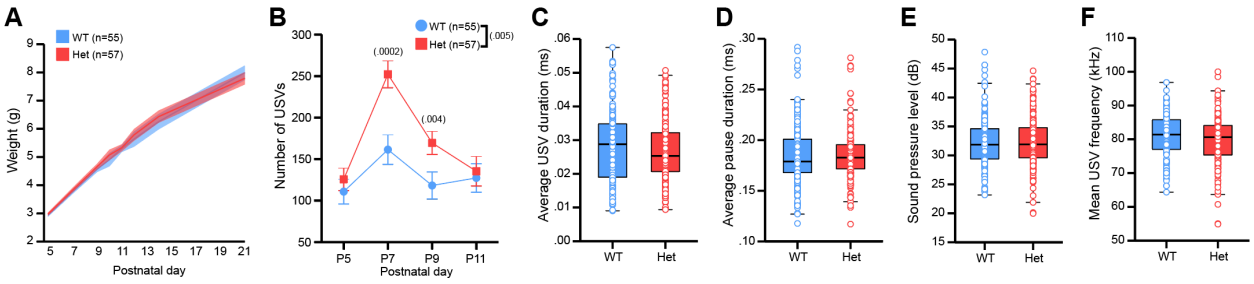

Figure 4: *Myt1l* haploinsufficiency results in heightened USV production.

(A) Hets have comparable early postnatal weight trajectories. **(B)** Hets produced fewer USVs than WT, which did not differ from WT calls on **(C-E)** temporal (call duration, pause duration, sound pressure level) or **(F)** spectral (mean frequency) features.

For panels A and B, grouped data are presented as means ± SEM. For panels C-F, grouped data are presented as boxplots with thick horizontal lines respective group medians, boxes 25th–75th percentiles, and whiskers 1.5xIQR. Individual data points are open circles. See ***Table S1*** *for statistical details.*

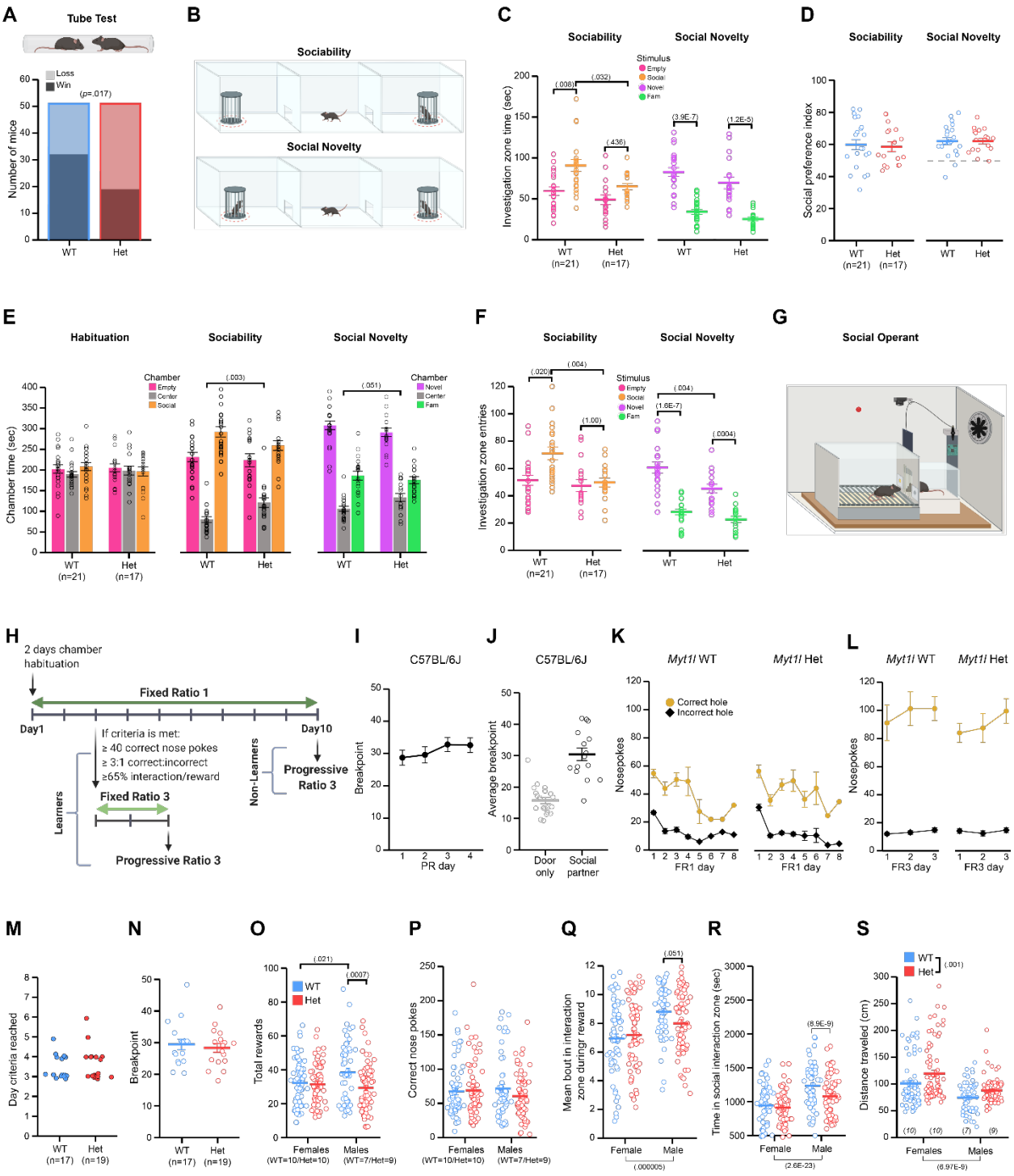

Figure 5: *Myt1l* haploinsufficiency altered social behaviors.

(A) MYT1L loss was associated with losses in the social dominance assay. **(B)** Social approach test schematic. Investigation zones demarcated by the dotted red lines. **(C)** In the sociability trial,

Hets spent less time investigating the social stimulus than WTs and failed to show an increase in time spent in the social versus empty investigation zones. No difference was observed in social novelty. **(D)** Sociability and social novelty preference scores were comparable. **(E)** Hets spent more time in the center chamber during both trials compared to WTs. **(F)** In the sociability trial, Hets entered the zone surrounding the social stimulus fewer times and failed to show an increase in entries into the social cup zone versus empty cup zone. In the social novelty trial, Hets entered the zone surrounding the novel mouse less than WT mice. **(G-H)** Social operant assay and timeline schematics. **(I)** C57BL/6J mice show consistency in the max level of effort they will exert for access to social interaction reward, demonstrating performance in the social operant test is reproducible across test days. **(J)** This max effort is driven by the social aspect of the reward as demonstrated by the difference in performance between mice that receive the social interaction reward versus mice that did not. **(K)** The time series of task acquisition demonstrates that *Myt1l* WT and Het mice learn to discriminate between correct versus incorrect holes for access to a social interaction reward during FR1 training. **(L)** All mice that meet learning criteria are motivated to work harder for the social interaction reward when more effort is required in FR3 testing. **(M)** Day to reach criteria during social operant training and **(N)** breakpoint reached during PR3 testing was not different between Hets and WTs. **(O)** Het males achieved less social rewards compared to WT males. **(P)** Het males and females exhibited a comparable number of correct nosepokes to WT littermates. **(Q)** During a reward, Het males trended towards less total time in the social interaction zone compared to WT males. Regardless of genotype, males spent more time in the social interaction zone compared to females. **(R)** Het males spent less total time in the social interaction zone than WT males. Regardless of genotype, males spent more time in the social interaction zone compared to females. **(S)** Female and male Hets traveled farther distances during 1-hr social

operant trials compared to WTs. Overall, females traveled farther distances than males during social operant trials.

For panels C-F, I-L, and N-S, grouped data are means ± SEM. Individual data points are open circles. See ***Table S1*** *for statistical details.*

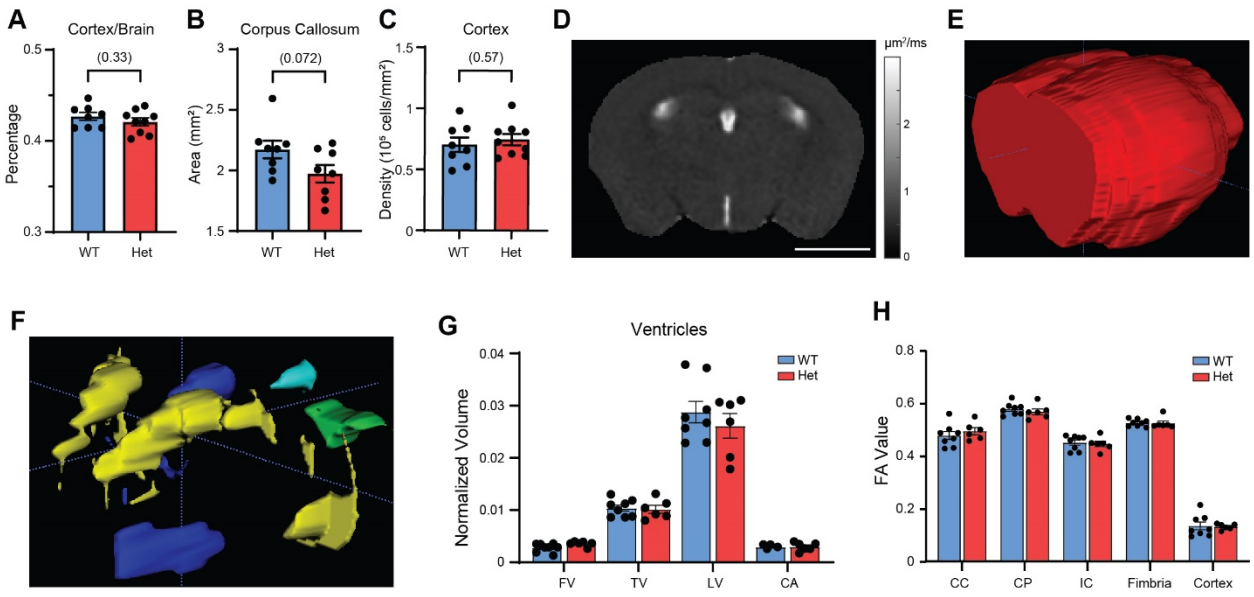

Supplemental Figure 3: MYT1L haploinsufficiency causes microcephaly and white-matter thinning in the corpus callosum of the adult mouse brain.

(A) The ratio between cortex and brain volume remains unchanged in *Myt1l* Het mice. **(B)** *Myt1l* Het mice had smaller corpus callosum volume ($p = 0.072$). **(C)** MYT1L loss did not change gross cell density in the adult Het mouse brain. **(D)** Apparent diffusion coefficient (ADC) map showing ventricular structures as hyperintense (bright) areas. Scale bar, 0.5 cm. **(E)** 3D reconstruction of the brain contour and **(F)** different ventricles, including the fourth ventricle (FV (green), third ventricle (TV; blue), lateral ventricles (LV; yellow), and cerebral aqueduct (CA; light blue). **(G)** MYT1L loss did not change ventricular sizes. **(H)** FA values were unchanged between Het and WT littermates.

*Data are represented as mean ± SEM. See **Table S1** for statistical test details.*

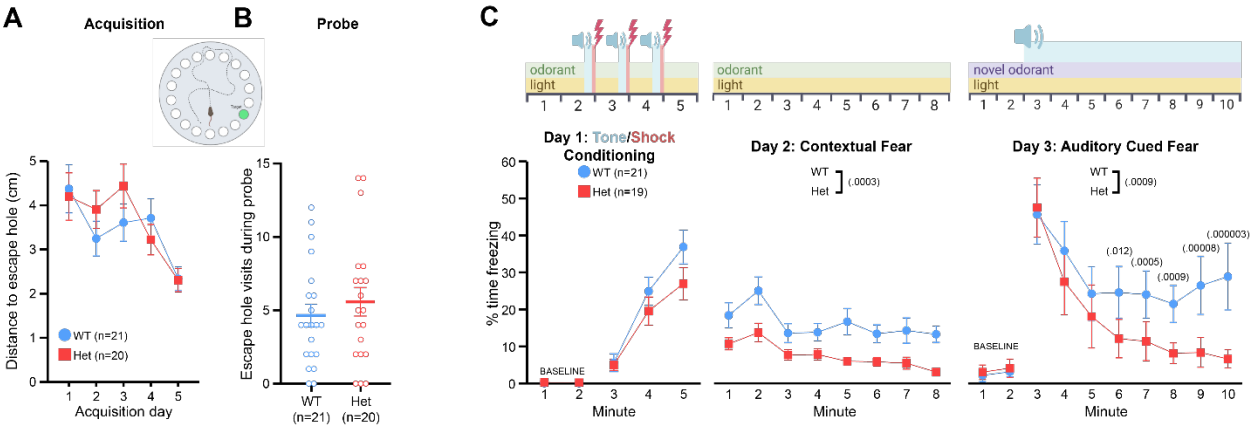

Supplemental Figure 4: *Myt1l* haploinsufficiency did not clearly disrupt spatial learning and memory or fear conditioning but leads to locomotor hyperactivity.

(A) Distance to reach the escape hole was not different between Hets and WTs during acquisitions trials in the Barnes maze. **(B)** During the Barnes maze probe trial, Hets visited the previously learned escape hole location at a similar frequency to WTs. **(C)** Conditioned fear timeline. Hets froze in response to a pairing of shock and tone/context at a level comparable to WTs on Day 1, yet, froze less during contextual and cued fear tests. No differences were observed for baseline data.

Grouped data are presented as means ± SEM with individual data points as open circles. See ***Table S1*** *for statistical test details.*

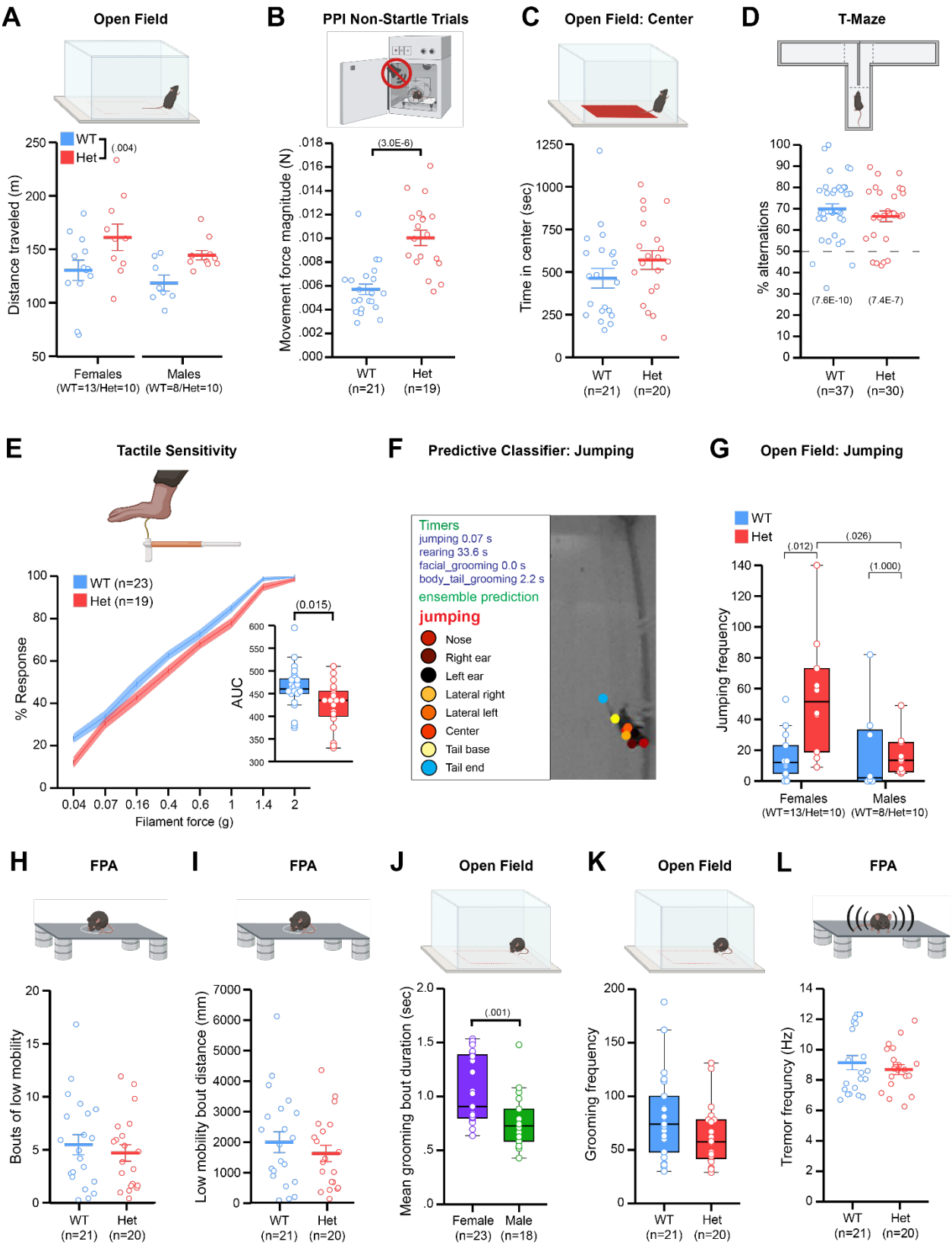
A
Open Field
Distance traveled (m)
WT
Het
(.004)
Females
(WT=13/Het=10)
Males
(WT=8/Het=10)
B
PPI Non-Startle Trials
Movement force magnitude (N)
(3.0E-6)
WT
(n=21)
Het
(n=19)
C
Open Field: Center
Time in center (sec)
WT
(n=21)
Het
(n=20)
D
T-Maze
% alternations
(7.6E-10)
(7.4E-7)
WT
(n=37)
Het
(n=30)
E
Tactile Sensitivity
% Response
WT (n=23)
Het (n=19)
Filament force (g)
AUC
(0.015)
F
Predictive Classifier: Jumping
Timers
jumping 0.07 s
rearing 33.6 s
facial_grooming 0.0 s
body_tail_grooming 2.2 s
ensemble prediction
jumping
Nose
Right ear
Left ear
Lateral right
Lateral left
Center
Tail base
Tail end
G
Open Field: Jumping
WT
Het
(.012)
(.026)
(1.000)
Jumping frequency
Females
(WT=13/Het=10)
Males
(WT=8/Het=10)
H
FPA
Bouts of low mobility
WT
(n=21)
Het
(n=20)
I
FPA
Low mobility bout distance (mm)
WT
(n=21)
Het
(n=20)
J
Open Field
Mean grooming bout duration (sec)
(.001)
Female
(n=23)
Male
(n=18)
K
Open Field
Grooming frequency
WT
(n=21)
Het
(n=20)
L
FPA
Tremor frequncy (Hz)
WT
(n=21)
Het
(n=20)

Supplemental Figure 5: *Myt1l* haploinsufficiency resulted in hyperactivity and reduced tactile sensitivity without evidence of stereotypies.

(A) Hets exhibited a longer distance traveled in the open field than WTs. **(B)** During the non-startle trials of the PPI task, Hets exhibited greater movement force magnitude than WTs. **(C)** Hets spent comparable time in the center of the open field chamber to WTs. **(D)** WTs and Hets exhibited % alternations in the T-maze different from chance (50%). **(E)** Het mice responded less than WTs to varying forces of tactile stimulation via von Frey filaments. **(F)** Representative video image frame for SimBA for jumping ensemble prediction. **(G)** Female Hets jumped significantly more than female WTs or male Hets. **(H-I)** In the FPA, Hets demonstrated a comparable number of low mobility bouts and distance traveled during those bouts to WTs. **(J)** Female mice engaged in longer grooming bouts than males. **(K)** Hets did not exhibit altered grooming frequency compared to WTs. **(L)** Hets did not exhibit a difference in tremor frequency in the FPA compared to WTs.

For panels A-F, I, J, and M grouped data are presented as means ± SEM. For panels F (inset), K, and L grouped data are presented as boxplots with thick horizontal lines respective group medians, boxes $25^{th} - 75^{th}$ percentiles, and whiskers 1.5 x IQR. Individual data points are open circles. See ***Table S1*** *for statistical test details.*

Supplemental Table 1. Statistical analyses for Chapter 2.

FIG	VARIABLE	COMPARISON	STATISTICAL TEST	OUTPUT
1D	MYT1L protein relative expression	genotype	One sample t test	t(5)=4.128, p =.0091
1E	MYT1L mRNA relative expression	genotype	Mann-Whiteny U	$U(N_{WT}=6,N_{Hets}=8)=7$, p=.029
1H	MYT1L allele specific expression	gDNA w/i cDNA	One sample t test	t(14)=26.48, p <.0001
2C	Posture	genotype	Fisher's exact test	OR=0.185, 95% CI[0.041,0.845], p=.038
2D	Weight	genotype	two-way rmANOVA	F(1,32)=8.398, p=.0007
		genotype x age		F(1.695,54.247)=8.074, p=.002
		sex		F(1,32)=23.711, p=.00003
3C	Brain weight	genotype	One sample t test	t(9)=3.061, p =.013
3D	Cortex Volume	genotype	One sample t test	t(15)=2.318, p =.035
3H	Brain volume	genotype	One sample t test	t(12)=2.579, p =.024
3I	White matter tracts (Normalized)	genotype x area	Two-way ANOVA	F(3,48)=7.737, p=.0003
	Corpus callosum	genotype	Bonferroni's multiple comparison	p =.0002
	Cerebral Peduncle	genotype	Bonferroni's multiple comparison	p =.60
	Internal Capsule	genotype	Bonferroni's multiple comparison	p =.17
	Fimbria	genotype	Bonferroni's multiple comparison	p >0.9999
S3A	Cortex/Brain	genotype	One sample t test	t(15)=0.9957, p =.33
S3B	Corpus callosum	genotype	One sample t test	t(14)=1.949, p =.072
S3C	Cortex cell density	genotype	One sample t test	t(15)=.5769, p =.57
S3G	Ventricles (Normalized)	genotype x area	Two-way ANOVA	F(3,36)=1.041, p=.39
	Fourth ventricle	genotype	Bonferroni's multiple comparison	p >0.9999

	Third ventricle	genotype	Bonferroni's multiple comparison	p >0.9999
	Lateral ventricle	genotype	Bonferroni's multiple comparison	p =.4673
	Cerebral aqueduct	genotype	Bonferroni's multiple comparison	p >0.9999
S3H	FA	genotype x area	Two-way ANOVA	F(4,60)=.4146, p=.80
	Corpus callosum	genotype	Bonferroni's multiple comparison	p >0.9999
	Cerebral Peduncle	genotype	Bonferroni's multiple comparison	p >0.9999
	Internal Capsule	genotype	Bonferroni's multiple comparison	p >0.9999
	Fimbria	genotype	Bonferroni's multiple comparison	p >0.9999
	Cortex	genotype	Bonferroni's multiple comparison	p >0.9999
4C	weight P5-P21	genotype	Linear mixed model	F(1,127)=0.041, p=.840
4D	USVs	genotype	two-way rmANOVA	F(1,108)=8.331, p=.005
		genotype x age		F(3,324)=3.721, p=.021
4E	Average USV duration	genotype	Mann-Whitney U	$U(N_{WT}$=186,N_{Het}=210)=17677, z=-1.630, p=.103
4F	Average pause duration	Genotype	Mann-Whitney U	$U(N_{WT}$=186,N_{Het}=210)=18783, z=-0.657, p=.511
4G	Sound pressure level	genotype	Mann-Whitney U	$U(N_{WT}$=186,N_{Het}=210)=19151, z=-0.333, p=.739
4H	Mean frequency	genotype	Mann-Whitney U	$U(N_{WT}$=186,N_{Het}=210)=17433, z=-1.845, p=.065
S4A	Barnes maze acquisition trial distance to escape hole	genotype	two-way rmANOVA	F(1,37)=3.766, p=.517

S4B	Barnes maze probe escape hole visits	genotype	two-way ANOVA	$F(1,37)=3.391$, $p=.365$
S4C	fear conditioning % freezing day 1, baseline	genotype	two-way rmANOVA	$F(1,36)=0.478$, $p=.494$
	fear conditioning % freezing day 1, min 3-5	genotype	two-way rmANOVA	$F(1,36)=1.947$, $p=.171$
	fear conditioning % freezing day 2	genotype	two-way rmANOVA	$F(1,36)=16.014$, $p=.0003$
	fear conditioning % freezing day 3, baseline	genotype	two-way rmANOVA	$F(1,36)=0.012$, $p=.913$
	fear conditioning % freezing day 3, min 3-10	genotype	two-way rmANOVA	$F(1,36)=12.925$, $p=.00097$
		genotype x minute		$F(6.575,236.7)=4.375$, $p=.0002$
5A	number of wins vs. losses in tube test	wins/losses x genotype	Chi-square	$\chi^2(1,102)=6.627$, $p=.017$
5C	sociability investigation time	genotype	two-way rmANOVA	$F(1,34)=10.021$, $p=.003$
		genotype w/i social stimulus	simple main effect, Bonferroni	$F(1,68)=7.471$, $p=.032$
		stimulus w/i WTs	simple main effect, Bonferroni	$F(1,34)=10.829$, $p=.008$
		stimulus w/i Hets	simple main effect, Bonferroni	$F(1,34)=2.705$, $p=.436$
5C	social novelty investigation time	genotype	two-way rmANOVA	$F(1,34)=5.115$, $p=.030$
		genotype w/i novel stimulus	simple main effect, Bonferroni	$F(1,68)=.003$, $p=.954$
		stimulus w/i WTs	simple main effect, Bonferroni	$F(1,34)=45.392$, $p=9.7E-8$
		stimulus w/i Hets	simple main effect, Bonferroni	$F(1,34)=21.012$, $p=.000003$
5D	social preference score	genotype	two-way ANOVA	$F(1,34)=0.075$, $p=.786$

	novelty preference score	genotype	two-way ANOVA	$F(1,34)=0.049$, $p=.827$
5E	habituation chamber time	genotype x chamber	two-way rmANOVA	$F(1.7,66.1)=2.871$, $p=.065$
	sociabiltiy chamber time	genotype x chamber	two-way rmANOVA	$F(1.8,66.5)=3.420$, $p=.042$
		genotype w/i center		$F(1,34)=8.445$, $p=.003$
	social novelty chamber time	genotype x chamber	two-way rmANOVA	$F(2,72)=2.113$, $p=.128$
5F	sociability investigation zone entries	genotype	two-way rmANOVA	$F(1,34)=10.210$, $p=.003$
		genotype w/i social stimulus	simple main effect, Bonferroni	$F(1,68)=11.429$, $p=.004$
		stimulus w/i WTs	simple main effect, Bonferroni	$F(1,34)=8.824$, $p=.020$
		stimulus w/i Hets	simple main effect, Bonferroni	$F(1,34)=.098$, $p=1.00$
5F	social novelty investigation zone entries	genotype	two-way rmANOVA	$F(1,34)=13.453$, $p=.0008$
		genotype w/i novel stimulus	simple main effect, Bonferroni	$F(1,68)=12.278$, $p=.004$
		stimulus w/i WTs	simple main effect, Bonferroni	$F(1,34)=48.683$, $p=4.8E-8$
		stimulus w/i Hets	simple main effect, Bonferroni	$F(1,34)=19.125$, $p=.0001$
5M	social operant day to reach cirteria	genotype	two-way ANOVA	$F(1,32)=0.433$, $p=.515$
5N	social operant breakpoint	genotype	two-way ANOVA	$F(1,31)=0.284$, $p=.598$
5O	social operant number of social rewards	genotype x sex	two-way ANOVA	$F(1,246)=5.177$, $p=.024$
		genotype w/i males	simple main effect	$F(1,246)=11.930$, $p=.0007$
		sex w/I WTs	simple main effect	$F(1,246)=5.359$, $p=.021$
5P	Number of correct nosepokes	genotype x sex	two-way ANOVA	$F(1,246)=1.659$, $p=.199$
		genotype w/i males		$F(1,246)=2.418$, $p=.121$
5Q	social operant mean bout in interaction zone during rewards	sex	two-way ANOVA	$F(1,246)=21.652$, $p=.000005$

		genotype x sex		$F(1,246)=3.420$, $p=.066$
		genotype w/i males	simple main effect	$F(1,246)=3.833$, $p=.051$
5R	social operant mean bout in interaction zone during rewards	sex	two-way ANOVA	$F(1,246)=122.630$, $p=2.2E-23$
		genotype x sex		$F(1,246)=12.451$, $p=.0005$
		genotype w/i males	simple main effect	$F(1,246)=35.472$, $p=8.9E-9$
S5A	distance traveled in open field	genotype	two-way ANOVA	$F(1,37)=9.162$, $p=.004$
S5B	social operant distance traveled	genotype	two-way ANOVA	$F(1,281)=10.687$, $p=.001$
		sex		$F(1,281)=35.693$, $p=6.97E-9$
S5C	movement force magnitude during non-startle trials	genotype	two-way ANOVA	$F(1,36)=30.656$, $p=3.0E-6$
S5D	time in center of open field	genotype	two-way ANOVA	$F(1,37)=1.459$, $p=.235$
S5E	% alternation in T-maze	WTs to 50%	One-sample t-test	$t(36)=8.513$, $p=7.6E-10$
		Hets to 50%	One-sample t-test	$t(28)=6.595$, $p=7.4E-7$
S5F	von Frey responses area under the curve	genotype	Mann-Whitney U	$U(N_{WT}=23,N_{Hets}=19)=123$, $z=-2.416$, $p=.015$
S5H	jumping frequency in the open field	genotype w/i females	Mann-Whitney U, Bonferroni correction	$U(N_{WT}=13,N_{Hets}=10)=19$, $z=-2.854$, $p=.012$
		sex w/i Hets	Mann-Whitney U, Bonferroni correction	$U(N_{Female}=10,N_{Male}=10)=15$, $z=-2.647$, $p=.026$
S5I	FPA number of low mobility bouts	genotype	two-way ANOVA	$F(1,37)=0.128$, $p=.722$
S5J	FPA distance during low mobility bouts	genotype	two-way ANOVA	$F(1,37)=0.291$, $p=.593$
S5K	mean grooming bout duration	sex	Mann-Whitney U	$U(N_{FEMALES}=23,N_{MALES}=18)=85$, $z=-3.205$, $p=.001$
S5L	grooming frequency	genotype	Mann-Whitney U	$U(N_{WT}=21,N_{Het}=19)=139$, $z=-1.639$, $p=.105$
S5M	tremor frequency	genotype	two-way ANOVA	$F(1,37)=0.998$, $p=.324$

Chapter 3: Molecular Functions of MYT1L in the Mouse Brain across Development

Jiayang Chen, Nicole A. Fuhler, Kevin Noguchi, Harrison W. Gabel, Joseph D. Dougherty

Adapted From:

A MYT1L syndrome mouse model recapitulates patient phenotypes and reveals altered brain development due to disrupted neuronal maturation

Chen, J., Lambo, M.E., Ge, X., Dearborn, J.T., Liu, Y., McCullough, K.B., Swift, R.G., Tabachnick, D.R., Tian, L., Noguchi, K., et al. (2021). A MYT1L syndrome mouse model recapitulates patient phenotypes and reveals altered brain development due to disrupted neuronal maturation. Neuron vol. 109,23 (2021): 3775-3792.e14.

And:

MYT1L is required for suppressing earlier neuronal development programs in the adult mouse brain

Chen, J., Fuhler, N.A., Noguchi, K., Dougherty, J.D. (2022). MYT1L is required for suppressing earlier neuronal development programs in the adult mouse brain.
bioRxiv 2022.10.17.512591; doi: https://doi.org/10.1101/2022.10.17.512591, in revision, Genome Research

3.1 Introduction

To further understand the molecular mechanisms underlying how MYT1L loss leads to different phenotypes in mice and potentially in humans, we first need to define MYT1L's normal molecular functions in the CNS, as well as how its loss alters mouse epigenetics and gene transcription. Therefore, in this third chapter, I focus on unraveling MYT1L's molecular functions during CNS development using MYT1L germline knockout mice generated in the previous chapter. I first defined MYT1L's expression pattern across multiple developmental stages and brain regions to help with choosing the proper time points and regions for molecular studies. Next, I adapted the CUT&RUN to map MYT1L binding in the mouse brain, as well as to measure histone modification changes upon MYT1L loss. I also combined ATAC-seq and RNA-seq with CUT&RUN targets to investigate how MYT1L loss directly changes chromatin accessibility and gene expression, looking for specific dysregulated pathways involved with disease pathogenesis. Finally, I performed motif analysis and co-immunoprecipitation (co-IP) experiments to explore MYT1L's binding partners, which might cooperate with MYT1L in regulating its target gene expression.

3.2 Results

3.2.1 Temporal and spatial expression patterns of MYT1L in the mouse brain

To establish where MYT1L functions, I first defined its expression across development. First, I looked at temporal expression in mice, to guide spatial expression studies afterwards. I found *Myt1l* mRNA increased across neurogenesis and peaked on postnatal day (P)1 yet sustained low levels into adulthood (**Fig. 6A**), paralleling human expression (**Fig. S6A**). Further, MYT1L maintained similar protein levels from embryonic day (E)14 to P1 then declined (**Fig. 6B**).

Initial spatial studies highlighted expression in new neurons of the developing brain (Kim et al., 1997), with an absence in glia. In contrast, a recent report proposed expression in oligodendroglia, promoting their fate (Shi et al., 2018). To resolve this inconsistency, I next investigated MYT1L's cellular expression. Immunofluorescence (IF) during peak cortical neurogenesis (E14), with a knockout-validated MYT1L antibody (**Fig. S6J**), revealed MYT1L's gradient of expression in the cortex and medial ganglionic eminence: almost absent in the progenitor layers (SOX2+) and highest in the upper cortical plate (CP, MAP2+; **Fig. 6C, D, S6B, C**), mirroring prior studies (Kim et al., 1997; Matsushita et al., 2014; Weiner and Chun, 1997). This parallels neuronal maturation gradients, with dim intermediate zone (IZ, TBR2+) expression, where immature neurons are found, and strongest expression in CP. In neonates, MYT1L was expressed in BRN2+ and CTIP2+ postmitotic neurons and a small portion of SOX2+ radial glia, but not in OLIG2+ oligodendroglia (**Fig. S6D, E**). In adults, MYT1L was expressed in NeuN+ neurons across all regions examined (**Fig. S6F, G**). MYT1L was not found in GFAP+ astrocytes nor OLIG2+ oligodendroglia (**Fig. S6H**). Collectively, my expression studies indicate MYT1L's function commences concurrently with final proliferation of neuronal progenitors, and its expression in all postmitotic neurons implies MYT1L haploinsufficiency potentially influences any neuron type. Further, the timeline suggests a peak function during neuronal maturation, but does not rule out a sustained role in adult neurons.

3.2.2 Mapping MYT1L binding sites in embryonic mouse cortex using CUT&RUN

The previous section has demonstrated that MYT1L has peak protein expression between E14 and P1 in the mouse brain. In order to map MYT1L targets *in vivo*, I optimized CUT&RUN on E14 mouse cortex (**Fig. 7A**) (Skene and Henikoff 2017). First, leveraging the MYT1L germline

knockout (S710fsX) mouse line, I validated CUT&RUN and antibody specificity on MYT1L KO samples. These S710fsX mice do not produce any MYT1L protein and thus can serve as a gold-standard control.

Next, I compared two peak calling methods, a stringent one where we called peaks from each biological replicate independently and intersected peak profiles from all three, and a more sensitive approach where we called peaks from a single merged alignment file of all three samples. In the intersected peaks, I identified 560 MYT1L peaks in wild-type (WT) E14 mouse cortex, and no peaks in all KO samples (**Fig. 7B**), indicating specificity. With the increased sensitivity approach, I identified 20305 unique peaks in WT compared with KO (**Fig. 7C**). Although MYT1L binding activity was still absent in KOs (**Fig. 7C**), this method led to a higher percentage of lower-enrichment peaks (49.1% of targets with enrichment score < 3, 9969 out of 20305, **Fig. S7A**). In addition, in *de novo* motif finding, the known MYT1L core binding motif AAGTT (Jiang et al. 1996; Mall et al. 2017) was significantly enriched in all 560 intersected peaks (100% of targets, p = 1e-11, **Fig. S7B,C**) but not in all peaks called from merged alignment file (**Fig. S7E**), suggesting peak calling from merged files might be recovering either more low-affinity bindings or experimental noise. Regardless, since MYT1L binding profiles have not been characterized at all after development, I next conducted CUT&RUN the adult mouse brain. Also, E14 brain has relatively few MYT1L-expressing cells (neurons), thus adult brain with its higher neuron proportion may map MYT1L binding in a more efficient way.

3.2.3 Mapping MYT1L binding sites in adult mouse prefrontal cortex using CUT&RUN

ADHD is observed in MYT1L Syndrome human patients, and hyperactivity is found in the mouse models. As ID and ASC are not well localized in the brain, I focused on the prefrontal

cortex (PFC), known to be dysregulated in human ADHD (Yasumura et al. 2019), as the target region for MYT1L CUT&RUN. I again compared two peak calling methods. First, I identified 28,798 reproducible MYT1L bound peaks by intersecting peak calls from 3 biological replicates of WT mouse PFC (**Fig. S7C**), and the MYT1L core binding motif AAGTT is significantly enriched via *de novo* motif finding (76.37% of targets, p = 1e-3125) (**Fig S7C, D**). Next, I did peak calling from the merged alignment file. This resulted in 115,143 peaks with slightly improved peak enrichment (55.7 % > 3 vs. 50.9% > 3 in E14) compared with the E14 dataset (**Fig S7A**). Motif analysis also showed a significantly enriched AAGTT motif (33.38% of targets, p = 1e-713) (**Fig. S7E, F**). Overall, many more peaks were identified from PFC CUT&RUN experiments, yet the majority of the E14 peaks were also recovered in PFC CUT&RUN (**Fig S7C, E**), suggesting CUT&RUN on PFC is more efficient than E14. In addition, I compared my MYT1L CUT&RUN targets with MYT1L ChIP-seq data from both E14 brain and fibroblasts overexpressing MYT1L, BRN2, and ASCL1 (Mall et al. 2017). Surprisingly, I did not see substantial overlaps between MYT1L CUT&RUN and ChIP-seq peaks (**Fig. S7G-J**). Notably, MYT1L CUT&RUN peaks overlap better with MYT1L brain ChIP-seq than with MYT1L fibroblast ChIP-seq (**Fig. S7G-J**), suggesting MYT1L binding is very context dependent with different binding in different cell types, and thus MYT1L likely does not serve as a pioneer factor that opens the chromatin of its targets regardless of cellular context. Since intersected peaks from PFC have the best MYT1L motif enrichment, I focused on the 28,798 MYT1L high-stringency binding targets identified from PFC CUT&RUN for the downstream analysis to understand MYT1L's functions in the adult brain and the long-term consequences of MYT1L loss.

3.2.4 Assessment of MYT1L binding partners

Previous ChIP-seq experiments have shown that MYT1L mainly binds to the promoter regions when overexpressed during reprogramming of MEFs (Mall et al. 2017). To test if it is also true *in vivo*, I annotated MYT1L targets from adult mouse PFC. Analysis of MYT1L of colocalization at these regions showed that MYT1L tends to bind open chromatin regions (95.3%, 27450/28798) with enhancers being the most common category, when compared to the categories of all open chromatin regions (**Fig. 7D, E, F**). Meanwhile, I utilized nuclei from the same animals to perform CUT&RUN on several histone modifications, including H3K4me3, H3K4me1, and H3K27ac (**Fig. 7A**). Leveraging these histone modification profiles, I further categorized enhancers into poised (H3K4me1+/H327ac-) and active (H3K4me1+/H3K27ac+) as previously described (Creyghton et al. 2010). To understand sequence preferences of MYT1L at promoters, poised enhancers, and active enhancers, I performed motif analysis using monaLisa to compare *de novo* binding motifs and predicted TFs co-occupancy between the three. Surprisingly, I found motifs for TFs that behave as transcriptional activators' motifs (e.g., SP1 and ELK1) to be enriched in MYT1L bound promoters, while neurogenic TFs (e.g., MEF2A and NEUROD1) and activity dependent TF (e.g., JUNB) motifs were specifically enriched in MYT1L bound enhancers (**Fig. 8A**), even when controlling for the differential baseline frequency of these TF motifs at promoters, poised enhancers and active enhancers respectively. Furthermore, this is not driven by the MYT1L core binding motif AAGTT since both MYT1L bound promoters and enhancers are significantly enriched for AAGTT (**Fig 8B**). In order to investigate if these motif abundances reflected the actual TF co-occupancy, I compared MYT1L CUT&RUN targets with published TF ChIP-seq data. As expected, compared to MYT1L unbound regions (MYT1L-), ChIP-seq peaks of candidate TFs, including SP1, ELK1, MEF2A, JUNB, NEUROD1, and NEUROD2, are significantly enriched in

MYT1L bound genomic regions (MYT1L+) (**Fig S8A-G**), suggesting these TFs are frequently bound at MYT1L bound peaks. Next, I compared TF ChIP-seq enrichment between the MYT1L+ promoters and the MYT1L+ enhancers. Echoing the motif analysis, MYT1L has significantly higher co-occupancy with SP1 and ELK1 in promoter regions than in enhancer regions (**Fig 8C, D, S8G**). Likewise, MEF2A and JUNB prefer binding MYT1L enhancer targets over promoter targets (**Fig 8E, F, S8G**). However, in contrast to the motif analysis, a much higher percentage of bHLH TFs NEUROD1 and NEUROD2 ChIP-seq peaks are at MYT1L-bound promoter targets than at MYT1L bound enhancers (**Fig 8G, H, S8G**), suggesting relative motif enrichment will not always predict the corresponding TF binding, or that a different protein might be binding this sequence at enhancers. Meanwhile, MYT1L does not appear to block the binding of NEUROD1 and NEUROD2 at enhancers since no obvious depletion of TF binding in MYT1L+ enhancers was observed (**Fig S8A-F**). Overall, such differential TF co-occupancy suggests MYT1L might play different roles at promoters and enhancers by cooperating with different co-factors.

In addition, *in vitro* studies have demonstrated that MYT1L can bind to SIN3B, a transcriptional repressor that recruits histone deacetylase (HDAC1/2) and demethylase (KDM5A) (Bainor et al. 2018; Naruse et al. 1999; Romm et al. 2005; Hayakawa et al. 2007; Nishibuchi et al. 2014). I found MYT1L interacts with SIN3B as well as HDAC2 in the mouse cortex as well from co-immunoprecipitation (Co-IP) experiments, while no direct interaction between MYT1L and HDAC1 was observed (**Fig. 8I**). These results suggest MYT1 might be able to facilitate the removal of active histone via interacting with the SIN3B repressor complex, echoing its repressive roles in trans-differentiation systems.

3.2.5 Histone modification changes in the adult *Myt1l* knockout mouse brain

Histone modifications are closely correlated with gene expression, where H3K4me3 and H3K27ac are thought to be marks for active gene expression (Black, Van Rechem, and Whetstine 2012; Heintzman et al. 2009). Thus, I investigated how histone landscape changes upon MYT1L loss. At MYT1L bound promoters, with decreased MYT1L binding activities in Hets (**Fig. S9A**) I found there were more H3K4me3 and H3K27ac modifications in Het PFC compared with WT (**Fig. S9B-E**), indicating MYT1L's role is normally to suppress gene expression by facilitating the removal of these marks.

In addition to promoters, enhancers are also crucial for controlling neuronal development programs as well as neuronal functions (Lu et al. 2020; Malik et al. 2014). Given enhancers have spatiotemporal activities throughout development (Carullo and Day 2019), and most of MYT1L targets identified in PFC are enhancers, I investigated how MYT1L binding influences histone landscapes at its bound enhancers. After segregating enhancers into active and poised stages by H3K27ac enrichment (**Fig. 7D, F**), I found MYT1L preferentially binds to activated enhancers compared to poised enhancers in the adult mouse PFC (**Fig. 7F**), and that the Het PFC has reduced MYT1L binding at both active and poised enhancers (**Fig. 9A**). Next, I explored how MYT1L bound enhancers are developmentally regulated. By integrating the histone CUT&RUN data from E14 CTX, I defined active and poised enhancers in E14 CTX and compared those with adult PFC enhancers. Out of 13,050 MYT1L bound active enhancers in adult PFC, 80% (10,443/13,050) are adult-specific active enhancers and only 20% are shared at both developmental time points (**Fig. 9B, C**). Furthermore, 24.8% (2,593/10,443) of those adult-specific active enhancer targets were poised in E14 CTX, suggesting MYT1L might also guide the activation of a small subset of poised enhancers during development. On the other hand, out of 3077 MYT1L targets annotated as E14

CTX active enhancers, only 21.3% (656/3077) of them are E14 CTX-specific active enhancers. Apparently, MYT1L occupancy at active enhancers is more prevalent in the adult stage, consistent with its major expression pattern in post-mitotic neurons.

Next, I examined histone landscape alterations at MYT1L+ enhancers in Het PFC to understand how MYT1L regulates enhancer activity. I found MYT1L+ active enhancer targets have increased H3K4me1 levels in Hets compared to WTs, while MYT1L poised enhancer targets showed unchanged H3K4me1 (**Fig. 9D**). Notably, both MYT1L+ active and poised enhancers displayed increased enrichment of H3K27ac, a histone modification marking enhancer activation, in Het PFC (**Fig. 9E**), suggesting MYT1L loss can also activate its bound poised enhancers. Together, these results indicate MYT1L normally facilitates repression of its bound enhancers, and MYT1L loss leads to aberrant enhancer activation.

3.2.6 Chromatin accessibility changes in the *Myt1l* knockout mouse brain across development

Chromatin accessibility is another indicator for gene activation/repression. Therefore, I performed Assay for Transposase Accessible Chromatin (ATAC)-seq (**Fig. 7A**) to determine how MYT1L loss alters chromatin accessibility. MYT1L is thought to modulate chromatin (Romm et al. 2005), with overexpression studies highlighting a repressive role (Mall et al. 2017). I sought here to determine if it has the same role during normal brain development and in the adult brain.

3.2.6.1 Chromatin accessibility changes in the developing *Myt1l* knockout mouse brain

I identified 1522 (FDR<.05, 3630 FDR<.1) differentially accessible regions (DARs) in mutant E14 cortex (Het and KO), with 871 less accessible DARs (**Fig. 10A, S10A-E**) and 641 more accessible DARs (**Fig. 10B**). Interestingly, KO mice showed smaller changes than Hets in terms of DARs decreasing accessibility after *Myt1l* mutation (**Fig. 10A**). Motif analysis on DARs

revealed that regions losing accessibility in mutants were enriched for motifs of stem-cell TFs (*Lhx2*, *Sox2*), as well as the key neurogenic TF *Ascl1* (**Fig. 10C**). More-accessible DARs are enriched for motifs of pro-differentiation TFs (*NF-1* and *Olig2*). A Gene Ontology (GO) analysis on DARs located in transcriptional start sites (TSS) revealed that less-accessible TSS were enriched for cell cycle and neurogenesis pathways (**Fig. 10D**). To parse out the direct effects from MYT1L loss, I specifically examined MYT1L binding targets defined from E13.5 brain and reprogrammed fibroblasts (Mall et al. 2017) as MYT1L CUT&RUN on E14 CTX did not produce high quality data. I found MYT1L loss decreased the accessibility of bound regions (**Fig. S10F**), suggesting loss of an activator. However, only a small subset of ChIP targets were DARs (3.62% of 6652 ChIP peaks). Thus, chromatin accessibility changes in mutants can be attributed to both direct and indirect effects. These results indicate MYT1L loss might lead to the repression of neural stem cell but activation of neural differentiation programs in the developing cortex, which is opposite to the *in vitro* findings that MYT1L is responsible for suppressing cell proliferation and promoting neuronal differentiation (Mall et al. 2017; Hu et al. 2013).

3.2.6.2 Chromatin accessibility changes in the adult *Myt1l* knockout mouse brain

I next asked if this chromatin accessibility deficits continue, or if MYT1L serves a distinct role in the adult brain by performing ATAC-seq on adult Het PFC. I discovered 4988 DARs (FDR<.05, 9756 FDR<.1, **Fig. S10G-K**), with 2607 less accessible DARs (**Fig. 10E**), 2381 more accessible DARs (**Fig. 10F**), and no peak showing sex*genotype interaction. Motif analysis on DARs found regions of lost accessibility in Hets are enriched for motifs of TFs involved in neuron projection (*Egr2,* **Fig. 10G**) and the NDD gene *Foxp1*, while those more-accessible regions had motifs for an early neuronal TF (*Eomes*; **Fig. S10L**). GO analysis, likewise, highlighted disruption of neuronal projection development and synaptic transmission pathways (**Fig. 10H, S10M**). Again,

I integrated ATAC-seq data with MYT1L CUT&RUN targets in adult PFC. I found that, although MYT1L haploinsufficiency indeed reduces overall MYT1L binding activities (**Fig. 9A**), it does not affect chromatin accessibility at promoter targets (**Fig. 10I, S10N**). Unlike MYT1L+ promoters which showed no ATAC-differences, in Hets, the MYT1L+ active enhancers showed increased chromatin accessibility compared to WTs (**Fig. 10J, S10O**), while MYT1L+ poised enhancers have no change (**Fig. 10K, S10P**). When only looking at DARs annotated as active enhancers, up-regulated DARs have a higher percentage in MYT1L+ active enhancers than in MYT1L- active enhancers (**Fig. S10Q**). Likewise, DARs annotated as poised enhancers showed the same pattern (**Fig. S10R**). This demonstrates that, at least on the chromatin accessibility, MYT1L tends to close the chromatin of its bound enhancers, and many DARs are direct effects in the adult brain.

Overall, ATAC-seq experiments revealed that MYT1L tends to be a chromatin activator during early brain development, while it mainly functions as a repressor in the adult brain. One thing to note is that most of MYT1L ChIP-seq targets from Mall et al. (2017) were from reprogrammed neurons (~3000 peaks) instead of E13.5 mouse brains (~500 peaks). This can make MYT1L's direct effects on chromatin accessibility in developing CTX inconclusive as ATAC-seq and ChIP-seq were not performed on the physiologically relevant backgrounds. However, at least in the adult, MYT1L consistently functions as a chromatin repressor at its bound promoters and especially enhancers in terms of histone modifications and chromatin accessibility.

3.2.7 Transcriptomic changes in the *Myt1l* knockout mouse brain across development

To understand the transcriptional consequences of altered histone landscapes and chromatin accessibility, I conducted RNA-seq on both E14 CTX and adult PFC. This allowed me

to both identify the transcriptional consequences of MYT1L mutation, and to determine if MYT1L has distinct effects on transcription between development and adulthood.

3.2.6.1 Transcriptomic alternations in the developing *Myt1l* knockout mouse brain

From E14 CTX, I identified 1768/13846 differentially expressed genes (DEGs; **Fig. 11A**). Fold changes of DEGs correlated well between Het and KO datasets. However, unlike ATAC-seq where KOs had smaller effects, there are larger DEG fold changes in KOs than Hets (**Fig. S11A, B**). This is consistent with a dose-dependence for MYT1L transcriptional regulatory activity. In addition, unlike in neuronal reprogramming where MYT1L overexpression mostly suppressed the expression of ChIP-seq targets, those targets showed subtly decreased expression in E14 RNA-seq upon MYT1L loss (**Fig. S11C, D**). Generally, there is no correlation between our mutant fold-changes and prior RNA-seq of MYT1L overexpression (OE) in MEF or knockdown (KD) fold-changes in cultured neurons (Mall et al. 2017) (**Fig. S11E, F**). I also categorically defined '*in vitro* MYT1L repressed' genes (downregulated by OE, upregulated by KD) and '*in vitro* MYT1L induced' genes (upregulated by OE, downregulated by KD) from published data (Mall et al. 2017). I found downregulated genes from my *in vivo* RNA-seq included 33 *in vitro* MYT1L induced genes from cultures ($p<.0005$). However, my upregulated genes did not show significant overlap with MYT1L repressed genes (**Fig. S11G, H**). Collectively, the loss of expression of MYT1L target genes *in vivo* indicates MYT1L functions preponderantly as an activator during early brain development. This is distinct from the 'repressor of non-neuronal lineages' function reported in direct conversion studies by OE *in vitro* (Mall et al. 2017). Specifically, I observed no de-repression of the previously described non-neuronal lineage genes with MYT1L mutation (**Fig. S11I**).

Next, as adult structural abnormalities can be attributed to deficits during development, I examined the gestalt of the RNA-seq using GO analysis to understand the pathways dysregulated in the embryo. There was an upregulation of CNS development pathways (**Fig. 11B**) in mutants, driven by markers of neuronal differentiation, suggesting early differentiation in mutants. Likewise, with Gene Set Enrichment Analysis (GSEA), I discovered a downregulation of mouse embryonic fibroblast (MEF) genes and upregulation of induced neuron (iN) genes in E14 mutants (**Fig. 11D, E**), indicating mutant cortex shifted profiles towards early neuronal differentiation. This was further supported by GSEA of pre-defined "mid-fetal" and "early-fetal" genes from the human brain, with mid-fetal genes precociously upregulated in mutants (**Fig. S11J, K**), opposite to the expression pattern of Chd8 mutants, who have macrocephaly rather than microcephaly (Katayama et al. 2016). I also looked at the Wnt and Notch signaling pathways, as they were suppressed by MYT1L in OE studies (Mall et al. 2017). However, I found no significant categorical upregulation in our Myt1l mutants (**Fig. S11L, M**). Surprisingly, MYT1L loss also impacted cell cycle pathway genes, with inhibitors (e.g. *Rb1*, *Gas1*) upregulated and mitosis genes (e.g. *Mcm7*, *Cdca5*) downregulated (**Fig. 11B, C**). I further compared gene expression between Het and KO mice and found a further upregulation of genes associated with chromatin activation in KOs (e.g. *Setd2*, *Dpf3*; **Fig. S11N**). Overall, the results suggest MYT1L mutation leads to precocious early neuronal programs and perturbs proliferation programs in embryos.

3.2.6.2 Transcriptomic alternations in the adult *Myt1l* knockout mouse brain

Then, I performed RNA-seq on the PFC to determine long-term transcriptional consequences of MYT1L haploinsufficiency. I identified 533/14,104 DEGs in Het PFC (**Fig. 12A**), with a few significant sex*genotype interactions. Mapped to ATAC-seq data, there was correspondence between changes in TSS accessibility and changes in gene expression (**Fig. S12A**),

as expected. Next, to define a role of MYT1L in the adult brain, I performed GO analysis on the DEGs. This revealed that genes from early phases of CNS development (e.g. *Eomes*, *Dcx*) were up-regulated in Hets (**Fig. 12B**). These are genes expressed in immature neurons, again indicating a shift in timing of transcriptional maturation. When comparing DEGs' expression between adult *in vivo* and prior *in vitro* RNA-seq, I still did not see significant correlation in their fold changes (**Fig. S12A, B**), indicating generally different transcriptional consequences in the two systems. Interestingly, however, only upregulated genes from our *in vivo* RNA-seq significantly overlapped with MYT1L repressed genes, while our downregulated genes did not show any overlap with MYT1L induced genes (**Fig. S12C, D**). Then, I performed GSEA and confirmed increased expression of "early-fetal" genes with no expression change of "mid-fetal", Wnt signaling, and Notch signaling genes in Hets (**Fig. 12D, E, S12E, F**). Persistent activation of developmental programs suggests that adult Het brains are trapped in an immature state. Indeed, genes downregulated upon MYT1L loss were significantly enriched in neuronal genes, showing an impaired mature neuronal identity (**Fig. S14A**). Likewise, GO analysis showed downregulation of neuronal projection development (e.g. *Epha7*, *L1cam*), ion homeostasis (e.g. *Kcnt2*, *Kcne4*), and synaptic transmission (*Gipc1*, *Vamp2*, **Fig. 12C**), echoing this immaturity and potentially disrupted neuronal functions.

With the high quality MYT1L CUT&RUN targets from adult PFC, I was able to further distinguish MYT1L's direct from indirect actions on gene expression. By looking at adult Het PFC RNA-seq fold changes of genes whose promoters are bound by MYT1L, I saw a subtle but significant upregulated expression of those MYT1L targets in Het (**Fig. 13A**), echoing MYT1L's role as a transcriptional repressor in reprogramming neurons (Mall et al. 2017). Then, I specifically looked at differentially expressed genes (DEGs). Among 310 down-regulated genes (dDEGs) and

223 up-regulated genes (uDEGs) in MYT1L Het PFC, I saw no biased distribution of MYT1L promoter targets, with 106 of the dDEGs and 85 of the uDEGs' promoters bound by MYT1L (**Fig. 13B**). Gene ontology (GO) analysis on these overlapped genes revealed that MYT1L promoter targets up-regulated in the MYT1L Het are significantly enriched in chromatin modification (e.g., *Hdac4*, **Fig. 13C, S13A**) and neuron projection development (e.g., *Lingo1* and *Cit*) pathways (**Fig. 13C**). Notably, several key regulators of neuronal migration (e.g., *Ctnnd2*, **Fig. S13B**) and deep cortical layer identity are directly bound by MYT1L and up-regulated in Het PFC, including Bcl11b, a master regulator of DL fate (Arlotta et al. 2005) (**Fig. S13C**). However, mature neuron functional pathways, like synaptic transmission and ion transport, that were down-regulated in Het PFC are not enriched in MYT1L promoter targets (data not shown), indicating their dysregulation is likely an indirect effect of MYT1L loss. Together, these findings suggest that MYT1L directly suppresses neuronal development programs for chromatin, migration, and neurite extension via binding to corresponding genes' promoters.

Enhancers are important cis-regulatory elements for gene expression. Therefore, I again leveraged my RNA-seq datasets to understand how MYT1L together with enhancers control gene expression and to define the transcriptional consequences of MYT1L loss at enhancers. To find enhancer-gene-pairs ('enhancer targets'), I utilized EnhancerAtlas 2.0, a consensus enhancer prediction database based on multiple high throughput dataset including histone modifications, ATAC-seq, ChIA-seq, etc. (Gao and Qian 2020). I only focused on active enhancers since they are MYT1L's major targets. Consistent with their increased active histone marks, MYT1L+ active enhancer targets tend to show increased gene expression in Het PFC compared with MYT1L-'s targets (**Fig. 14A**). Likewise, when overlapping with DEGs, there are more uDEGs associated with

MYT1L+ active enhancers compared to dDEGs, again emphasizing MYT1L's primary role as a transcriptional repressor (**Fig. 14B**) in adult cortex.

I next examined the putative function of all MYT1L enhancer target genes using GO, focusing on adult-specific MYT1L+ enhancers and those enhancers bound at both ages. Since there are too few overlaps between MYT1L active enhancer targets and DEGs to perform GO (**Fig. 14B**), I focused on all MYT1L+ active enhancer targets to obtain an overview of those enhancer functions. GO analysis on active enhancer targets found at both ages displayed enrichment of cytoskeleton pathways (**Fig. 14C**). This is consistent with cytoskeleton related biological processes being constantly required from early development to adulthood. Meanwhile, PFC-specific active enhancer targets showed significant enrichment of neuronal migration and projection neuron development pathways (e.g., *Dcx*, **Fig. 14D, E**), indicating the aberrant activation of earlier neuronal development programs in Het PFC seen at promoters can also be further exacerbated by dysregulation of MYT1L bound active enhancers.

3.2.6.3 Cross comparison between MYT1L Syndrome mouse model and other NDD mouse models as well as human disease dataset

Finally, since MYT1L Syndrome is one of several forms of ID/ASC caused by TF mutation, I tested whether our MYT1L DEGs are dysregulated in related models. DEGs from adult RNA-seq significantly overlapped with DEGs from *Chd8*, *Chd2*, *Kdm5c*, *Phf6*, *Foxp1*, and *Pogz* KO mouse models (**Fig. S14B**). DEGs from E14 were enriched in the *Chd2* and *Chd8* datasets (**Fig. S14B, C**). Interestingly, post hoc analysis showed genes were dysregulated in an opposite direction between *Myt1l* mutant mice and other NDD mouse models (**Fig. S14C**). This suggests genes implicated in different NDD models are pathogenic when dysregulated in either direction.

Comparison to human data showed that DEGs derived from PFC of Het mice were enriched in ADHD and ASC associated genes but not in human IDD, SCZ, or microcephaly genes

(**Fig. S14B, D**). Conversely, DEGs from E14 only significantly overlapped with human ID and microcephaly (**Fig. S14B, D**). Together, these findings highlight some convergence between MYT1L Syndrome and other NDDs.

3.3 Discussion

3.3.1 Does MYT1L have distinct functions between embryonic cortex and PFC?

Although the majority of the 560 peaks from E14 CTX CUT&RUN were recovered in PFC CUT&RUN, the lack of sensitivity in E14 CUT&RUN makes it difficult to determine if this a trend will still hold true for all possible MYT1L binding sites in E14 CTX. In addition, MYT1L tends to bind open chromatin regions with an AAGTT motif, based on PFC CUT&RUN and ATAC-seq. As chromatin accessibility changes drastically across different developmental stages, it is highly likely that there are distinct genomic regions available for MYT1L to bind in E14 CTX and adult PFC, respectively. Nevertheless, more precise and efficient measures of MYT1L binding in E14 CTX are necessary to further investigate this hypothetical difference.

Utilizing MYT1L ChIP-seq targets from Mall et al. (2017), I defined MYT1L mainly as an activator in terms of chromatin opening and transcriptional activation in E14 CTX. This is corroborated by *in vivo* studies (Kepa et al. 2017; Chen et al. 2021). On the other hand, multi-omics data integration for adult PFC suggests MYT1L interacts with SIN3B repressor complex to erase active histone marks, close chromatin, and suppress gene expression. Despite these differences in its main function, MYT1L suppresses early neuronal development programs at both ages. This supports the conclusions from trans-differentiation *in vitro* studies, which state that MYT1L suppresses non-neuronal genes to facilitate neuronal differentiation (Wapinski et al. 2013;

Mall et al. 2017). These results suggest MYT1L binding has distinct functions at different sites or acts in a context-dependent manner, and the effects of MYT1L binding might depend on characteristics of its bound genomic regions as well as available co-factors at different developmental timepoints.

3.3.2 Does MYT1L have different *in vitro* and *in vivo* functions?

Despite consensus findings that MYT1L represses transcription in both trans-differentiation systems and adult mouse PFC, MYT1L tends to have distinct targets between the two. Unlike the repressive effects of MYT1L overexpression on non-neuronal genes described in the trans-differentiation system (Mall et al. 2017), I defined a novel role of MYT1L in suppressing neuronal developmental programs in the adult mouse brain, in which no obvious activation of non-neuronal genes was observed upon MYT1L loss. Observation of the same effects on different targets between *in vitro* and *vivo* systems again indicate MYT1L's repressive functions are context dependent.

Interestingly, I also showed poor overlap between *in vitro* ChIP-seq targets and *in vivo* CUT&RUN targets, although both are highly enriched for MYT1L core binding motifs. Meanwhile, I was also able to identify more MYT1L binding sites with CUT&RUN compared to the published ChIP-seq, with the majority of them being enhancers instead of promoters. Furthermore, MYT1L seems to mainly function as an activator to open chromatin and promote cell proliferation programs, which were normally repressed by MYT1L overexpression *in vitro* (Mall et al. 2017; Hu et al. 2013). This discrepancy first speaks for the improved sensitivity of CUT&RUN over ChIP-seq (Skene and Henikoff 2017). Second, it indicates ectopic expression of MYT1L might change its functions from those found under physiological conditions.

3.3.3 Summary

Here, I utilized a MYT1L germline knockout mouse model to investigate MYT1L's role in neuronal maturation and underlying molecular mechanisms. I mapped high-confidence MYT1L binding targets as well as histone landscape changes upon MYT1L loss *in vivo* using CUT&RUN. Integrating data from CUT&RUN, ATAC-seq, and RNA-seq, I defined a novel role for MYT1L to suppress neuronal developmental programs in adult mouse brain by closing chromatin structures and erasing active histone markers at its binding sites, especially at enhancers. Meanwhile, parallel studies on E14 CTX showed that MYT1L can facilitate cell proliferation while suppressing early neuronal differentiation, suggesting a disrupted neuronal development trajectory, although more precise mapping of MYT1L binding targets at this stage is still needed.

Collectively, this chapter provides technical guidance for using CUT&RUN to profile MYT1L binding in different developmental stages and systems. As a high confidence approach, MYT1L CUT&RUN data enables high throughput functional screening assays to further delineate MYT1L's effects on different targets. Finally, this detailed investigation on MYT1L binding coupled with dysregulation in the MYT1L Syndrome mouse model advances our understanding of the complicated neuronal development programs in both physiological and pathological conditions.

3.4 Materials and Methods

3.4.1 Animal models

All procedures using mice were approved by the Institutional Care and Use Committee at Washington University School of Medicine and conducted in accordance with the approved Animal Studies Protocol. All mice used in this study were bred and maintained in the vivarium at

Washington University in St. Louis in individually ventilated (36.2 x 17.1 x 13 cm) or static (28.5 x 17.5 x 12 cm; post-weaning behavior only) translucent plastic cages with corncob bedding and ad libitum access to standard lab diet and water. Animals were kept at 12/12 hour light/dark cycle, and room temperature (20-22°C) and relative humidity (50%) were controlled automatically. For all experiments, adequate measures were taken to minimize any pain or discomfort. Breeding pairs for experimental cohorts comprised *Myt1l* Hets and wild type C57BL/6J mice (JAX Stock No. 000664) to generate male and female *Myt1l* Het and WT littermates. For embryonic CUT&RUN, *Myt1l* Het x Het breeding pairs were used to generate *Myt1l* WT and homozygous mutant littermates. Animals were weaned at P21, and group-housed by sex and genotype. Biological replicates for all experiments are sex and genotype balanced.

3.4.2 Method details

RNA extraction and RT-qPCR

Mice brains or cortex were dissected out at different developmental stages and homogenized in lysis buffer (10 mM Tris-HCl, pH 7.4, 10 mM NaCl, 3 mM MgCl2, 0.1% IGEPAL CA-630, 0.1% RNase inhibitor) on ice. Then lysates were mixed with Trizol LS and chloroform. After centrifugation, RNA was extracted from the aqueous layer with Zymo RNA Clean and ConcentratorTM-5 kit. cDNA libraries were prepared using qScript cDNA synthesis Kit (QuantaBio). RT-qPCR were performed using SYBR Green Master Mix (Thermo Fisher) on QuantStudio 6 Flex Real Time PCR System using primers in the **Appendix**. We normalized cycle counts to Gapdh or β-actin and calculated normalized relative gene expression using ΔΔCT. To compare MYT1L mRNA expression between genotypes, we put 6 WT and 8 Het brains into qPCR procedure. To understand MYT1L expression in human brain, we acquired normalized RNA-seq RPKM values of MYT1L in primary somatosensory cortex (S1C) from Allen Brain Atlas

BrainSpan dataset (http://www.brainspan.org/) and plotted MYT1L mRNA temporal expression in R.

Immunofluorescence

Mice brains were dissected out at different developmental stages and fixed in 4% paraformaldehyde (PFA) overnight at 4°C. After gradient sucrose dehydration and O.C.T. compound embedding, brains were sectioned using Leica Cryostat (15 μm for E14 brains and 30 μm for postnatal brains). Antigen retrieval was performed by boiling sections in 95°C 10 nM sodium citrate (pH 6.0, 0.05% Tween-20) for 10 mins. Then, sections were incubated in the blocking buffer (5% normal donkey serum, 0.1% Triton X-100 in PBS) at RT for 1 hour. Primary antibodies, including anti-MYT1L (1:500, 25234-1-AP, Proteintech), anti-MAP2 (1:200, #188044, SYSY), anti-SOX2 (1:200, sc-17320, Santa Cruz), anti-TBR2 (1:400, AB15894, Millipore), anti-Ki-67 (1:500, #14-5698-82, Invitrogen), anti-CTIP2 (1:500, ab18465, Abcam), anti-BRN2 (1:500, sc-393324, Santa Cruz), anti-NEUN (1:500, #12943, Cell Signaling), anti-GFAP (1:500, ab53554, Abcam), anti-OLIG2 (1:200, AF2418, R&D Systems), and anti-TBR1 (1:500, ab31940, Abcam) were used to detect different cell markers. Next, sections were incubated in fluorescence conjugated secondary antibodies, including donkey anti-rabbit (Alexa 488, 546, and 647, Invitrogen), donkey anti-mouse (Alexa 546, Invitrogen), donkey anti-chicken (Alexa 488, Jackson ImmunoResearch), donkey anti-rat (Alexa 488 and 647, Invitrogen), and donkey anti-goat (Alexa 488 and 647, Jackson ImmunoResearch) at 1:500 dilution for 2 hours in RT. Images were captured under Zeiss Confocal Microscope or Zeiss Axio Scan Slide Scanner and cell counting was performed using ImageJ. In order to compare cell numbers of different cell types across genotypes, we had 5 WT, 6 Het, and 5 KO E14 brains for cell counting experiments. And we had 6 WT, 6 Het, and 5 KO E14 brains to quantify the Ki-67 positive cells.

CUT&RUN on embryonic and adult prefrontal cortex

CUT&RUN was performed on the embryonic and adult prefrontal cortex as previously described. 3 biological replicates were included for each age and genotype. Briefly, we dissected out E14.5 mouse embryonic cortex or P60 mouse prefrontal cortex, and nuclei were isolated using Nuclei EZ Prep Buffer (Sigma 4432370) and counted on cell cytometer. 300k nuclei were bound to the Concanavalin A-Coated beads for one CUT&RUN reaction on either MYT1L, or IgG, or histone marks. Then, beads were incubated with desired primary antibodies separately, including Rb-MYT1L (0.5 µg), Rb-H3K4me1 (1 µg), Rb-H3K4me3 (1 µg), Rb-H3K27ac (1 µg), and Rb IgG (1 µg), at 4 ℃ on the nutator for overnight. To bind pAg-MNase fusion protein, beads were incubated with diluted CUTANA pAg-MNase (1:20) on the rotator at 4 ℃ for 1 hour. Chromatin digestion was performed at 0 ℃ with the addition of CaCl2 (100 mM) for 30min. To digest the RNA and release the cleaved DNA fragments, reactions were incubated with Stop Buffer at 37 ℃ for 30min in the thermocycler. Magnetic stands were used to bind beads afterwards, and supernants containing DNA fragments were retrieved for sequencing library preparations.

CUT&RUN library preparation and the next generation sequencing

DNA fragments were extracted from CUT&RUN experiments by Phenol/Chloroform/isoamyl Alcohol (pH 7.9) mix. KAPA HyperPrep Kit (KK8504) was used to generate dual-indexed sequencing libraries. Generated libraries were purified using Mag-Bind beads. We ran Tapestation for libraries and checked the nucleosome peaks pattern as quality control. Finally, libraries were submitted to GTAC Washington University School of Medicine for Novaseq aiming for 50M reads per MYT1L and IgG library and 10M reads per histone library.

CUT&RUN data analysis

Raw reads were trimmed by Trimmomatic software to remove adapter sequence. We used Fastqc to check read quality before and after trimming. Then reads were mapped to the mm10 genome by Bowtie2. We filtered out mitochondrial reads (Samtools), PCR duplicates (Picard), non-unique alignments (MAPQ > 30), and unmapped reads (Samtools). MYT1L peaks were called from both individual biological replicates and merged bam files from one genotype by MACS2 ($q<0.05$) using IgG as background. Histones' peaks were called from merged bam files by MACS2 ($q<0.05$) using down-sampled IgG as background. With MYT1L peaks called from biological replicates, bedTools was used to find intersecting peaks among 3 replicates. With MYT1L peaks called from merged bam files, bedTools was also utilized to exclude peaks from KO samples. Peaks were annotated primarily by Homer and then grouped into subcategories according to the following method sections. Peak heatmaps were generated by the bedTools plotHeatmap function. Genome track graphs were generated using Integrated Genomics Viewer (https://igv.org/). In order to compare fold changes of histone peaks between WT and mutant libraries, we derived peaks read counts from individual histone library's bam file using bedtools. With read counts, we utilized the edgeR package to perform differential enrichment analysis and calculated fold changes of each histone peak in mutant libraries.

Define active and poised enhancers

Active and poised enhancers were defined as previously described. Briefly, enhancers were defined as H3K4me1 peaks located outside of the promoter regions (TSS ±1kb) as well as absent of H3K4me3. Enhancers that overlap with H3K27ac peaks were categorized as active enhancers, and those H3K27ac negative ones were defined as poised enhancers.

Motif analysis

De novo motif findings were performed using both Homer and monaLisa (Machlab et al. 2022). For Homer usage, full length peaks were fed into the software, and ATAC-seq peaks from the same brain region and the same age were used as background. For monaLisa usage, promoter, active enhancer, and poised enhancer targets were grouped into separate bins and tested individually. To avoid length bias, we resized peaks into fixed-size regions around the peak midpoint before running the analysis. Then, the k-mer enrichment analysis was performed to examine the MYT1L core binding motif enrichment using 5 as unbiased motif length and ATAC-seq peaks as background. De novo motifs with FDR<1e-50 were plotted out in the heatmap. At last, we performed known motif finding using monaLisa and JASPAR2020 motif database on MYT1L targets. plotMotifHeatmaps was used to visualize significantly enriched known motifs with FDR<1e-5. TFs only being expressed in PFC RNA-seq dataset were plotted in the heatmap.

Predicting enhancer-gene-pairs (EGPs)

EGPs were predicted using EnhancerAtlas 2.0 (http://www.enhanceratlas.org/) (Gao and Qian 2020). Specifically, I selected the E14.5 Brain, Brain, and Neuron database to annotate different subgroups of enhancers with their putative targeting genes.

ATAC-seq

ATAC-seq was performed as described before (Buenrostro et al. 2015). Briefly, mouse E14 cortex (6 WT, 5 Het, and 6 KO E14 cortex) or adult PFC (P60-P70) was dissected and gently homogenized in cold nuclear isolation buffer (10 mM Tris-HCl, pH 7.4, 10 mM NaCl, 3 mM MgCl2, 0.1% IGEPAL CA-630). Embryonic tissues were pooled across sexes, adult tissues included both sexes, balanced for genotype. Lysates were filtered through 40 µm mesh strainer. After spinning down, 100,000 nuclei were put into the tagmentation reaction for each sample. We had 6 WT, 5 Het and 6 KO cortex for embryonic experiments. For adult PFC experiments, we put

6 WT and 6 PFC into the pipeline. Tagmentation reaction was performed using Illumina Tagment DNA TDE1 Enzyme and Buffer Kit with 30 min incubation time at 37°C. Immediately following the tagmentation, we purified DNA fragments using QIAquick PCR Purification Kit. We took half amount of purified DNA fragments and added Illumina Nextera i5+i7 adapters with unique index to individual samples by PCR reaction (Phusion, primers seen in Key Resources Table, PCR program: 72°C for 5 min, 98°C for 30 s, 98°C for 10 s, 63°C for 30 s, 72°C for 1 min, repeat 3-5 for 8-10 cycles, and hold at 10°C). Generated libraries were purified using AMpure beads (1:1.8 dilution). We ran Tapestation for libraries and checked the nucleosome peaks pattern as quality control. Finally, libraries were submitted to GTAC Washington University School of Medicine for Novaseq aiming for 50M reads per sample.

DAR analysis

Raw reads were trimmed by Trimmomatic software to remove adapter sequence. We used FastQC to check reads quality before and after trimming. Then reads were mapped to mm10 genome by Bowtie2. We filtered out mitochondrial reads (Samtools), PCR duplicates (Picard), non-unique alignments (MAPQ > 30), and unmapped reads (Samtools). Then a series of QC metrics were examined to ensure ATAC experiments worked well, including insert size distribution, mitochondria reads percentage, non-redundant reads percentage, and TSS enrichment. To adjust read start sites, we shifted reads aligned to + strand by +4bp and reads aligned to - strand by -5 bp by bedtools and awk. After shifting, we merged bam files for all samples in one specific time stage (E14 or adult) together and performed peak calling by MACS2 with $q < 0.05$. Peaks were annotated by Homer software. In order to perform differential accessible region analysis, I derived peaks read counts from individual sample's shifted bam file using bedtools. With read counts, utilized edgeR package to identify DARs. Briefly, I first checked library size, read counts

distribution, Pearson correlation, and multidimensional scale plots and identified no obvious outlier sample. Then I normalized reads and removed unwanted variables using the RUVseq package. For E14 cortex ATAC-seq, I fitted the data into a nested interaction model to identify altered chromatin accessibility across all genotypes (WT, Het, and KO). And I considered peaks with the same significant fold change (FDR < .1) direction in Het and KO as true DARs. For adult PFC, a negative binomial generalized linear model was fitted and sex was counted as covariate when testing for DARs (FDR < .1). Heatmaps for DARs were generated by deepTools. TSS peaks were defined as ±1kb from TSS and all other peaks were considered non-TSS peaks. Metagene2 and ggplot2 were used to extract read depths for example loci and generate average coverage with 95% confidence intervals. MYT1L ChIP targets from Mall et al.'s Table S2 were mapped to ATAC-seq data sets by bedTools and I defined overlapping peaks between the two with 1kb maximum gap. Motif analysis was performed using Homer software on DARs (FDR < .1). I used more-accessible regions as background when finding motifs for less-accessible regions and vice versa.

RNA-seq

Embryonic cortex and adult PFC (P60-P70) was dissected out and RNA was extracted as described above. Embryonic tissues were pooled across sexes, adult Adult tissues included both sexes, balanced for genotype. Total RNA integrity was determined using Agilent 4200 Tapestation. Library preparation was performed with 10ng of total RNA with a RIN score greater than 8.0. ds-cDNA was prepared using the SMARTer Ultra Low RNA kit for Illumina Sequencing (Takara-Clontech) per manufacturer's protocol. cDNA was fragmented using a Covaris E220 sonicator using peak incident power 18, duty factor 20%, cycles per burst 50 for 120 seconds. cDNA was blunt ended, had an A base added to the 3' ends, and then had Illumina sequencing adapters ligated

to the ends. Ligated fragments were then amplified for 15 cycles using primers incorporating unique dual index tags. Fragments were sequenced on an Illumina NovaSeq-6000 using paired end reads extending 150 bases. Again, raw reads were trimmed by Trimmomatic software to remove adapter sequence and we used FastQC to check reads quality before and after trimming. rRNA reads were filtered out by Bowtie2. And filtered reads were mapped to the mouse mm10 genome by STAR. Read counts for genes were derived by HTSeq software for individual samples. We checked read counts distribution, junction saturation, library size, Pearson correlation and multidimensional scale plots to rule out any outliers. In the end, we were able to put 6 WT, 6 Het, 4 KO E14 cortex and 6 WT, 6 Het adult PFC into the DGE analysis pipeline.

Differential Gene Expression analysis

Similar to DAR analysis, we normalized raw counts and removed unwanted variables with the edgeR and RUVseq package. A nested interaction model was fitted to identify differential gene expression across genotypes for E14 cortex RNA-seq. DEGs with the same significant fold change direction in both Het and KO samples were considered as true MYT1L regulated genes and were subjected to downstream analysis. For adult PFC RNA-seq, we fitted the data to a negative binomial generalized linear model with sex as covariates. We applied cut-off FDR <.1 to define DEGs. Heatmaps for DEGs were generated by heatmap.2 function in R.

GO analysis

To perform GO analysis on DARs, we assigned DARs (FDR < .1) located within ±1kb from TSS to corresponding genes. GO analysis was performed using BiNGO in Cytoscape. p values were adjusted by Benjamini-Hochberg FDR correction and FDR < 0.05 cut-off was used to determine significant enrichments. The same software and corrected p value cut-off was applied to GO analysis on DEGs (FDR < .1) in RNA-seq.

GSEA analysis

GSEA was performed as described before (Subramanian et al. 2005) using GSEA v4.0.3 (https://www.gsea-msigdb.org/gsea/index.jsp). I first examined gene set collections H (Hallmark gene sets) and C2 (curated gene sets of online pathway databases) to understand how MYT1L loss affects different cellular processes in a comprehensive manner. Then I tested the expression changes of MYT1L ChIP targets, human "early-fetal" and "mid-fetal" genes (Kang et al. 2011; Katayama et al. 2016), MEF signature genes, induced neuron signature genes on E14 cortex and adult PFC expression data, Wnt signaling genes (MGI GO:0016055), and Notch signaling genes (MGI GO:0007219). Human gene IDs were converted into mouse gene IDs by BioMart (https://www.ensembl.org/biomart). All analysis was performed with "gene_set" as permutation type and 1,000 permutations. Significant enrichment was determined by FDR <. 1 cut-off.

Comparison between in vivo and in vitro RNA-seq

In vitro RNA-seq data were obtained from Mall et al., 2017 studies on MYT1L overexpression (OE) in MEF and shRNA knockdown (KD) in primary hippocampal neuron cultures (Mall et al., 2017). I defined genes that showed upregulation in OE but downregulation in KD as MYT1L induced genes, while genes getting downregulated in OE but upregulated in KD were considered as MYT1L repressed genes. Then, the hypergeometric test was performed to determine whether there is significant overlapping between DEGs from our *in vivo* RNA-seq experiments and previously reported MYT1L targeted genes *in vitro*. I also used R to investigate linear regression of DEGs' fold changes between *in vivo* and *in vitro* RNA-seq experiments.

Disease models and human genetic data sets enrichment

DEGs of different ID/ASC related mouse model were derived from CHD8 haploinsufficient cortex ($p < .05$ for E14.5, FDR < .1 for P77) (Gompers et al. 2017), KDM5C KO

frontal cortex ($p < 0.01$) (Iwase et al. 2016), CHD2 haploinsufficient embryonic cortex ($p < .05$) and P30 hippocampus (FDR < .1) (Y. J. Kim et al. 2018), PHF6 KO cortex (FDR < 0.05) (Cheng et al. 2018), FOXP1 KO hippocampus (FDR < 0.05) (Araujo et al. 2015), and POGZ cKO hippocampus (FDR < .05) (Suliman-Lavie et al. 2020). For human diseases genetic data sets, we downloaded ASC genes from SFARI (huamn module, gene score 1 and 2), ADHD genes from ADHDgene (http://adhd.psych.ac.cn/), ID genes from IDGenetics (http://www.ccgenomics.cn/IDGenetics/), SCZ genes from SZDB2.0 SNP data sets (http://www.szdb.org/), and Microcephaly genes from DisGeNET (https://www.disgenet.org/home/). Enrichment analysis was performed using the one-sided hypergeometric test and p values were adjusted by Benjamini-Hochberg correction.

Quantification and statistical analysis

Statistical analyses and graph plottings were performed using IBM SPSS Statistics (v.26), GraphPad Prism (v.8.2.1), and R (v.4.0.0). Prior to analyses, data was screened for missing values and fit of distributions with assumptions underlying univariate analysis. This included the Shapiro-Wilk test on z-score-transformed data and qqplot investigations for normality, Levene's test for homogeneity of variance, and boxplot and z-score (±3.29) investigation for identification of influential outliers. Means and standard errors were computed for each measure. Analysis of variance (ANOVA), including repeated measures or mixed models, was used to analyze data where appropriate. Sex was included as a biological variable in all analyses across all experiments. Simple main effects were used to dissect significant interactions. Where appropriate, the Greenhouse-Geisser or Huynh-Feldt adjustment was used to protect against violations of sphericity. Multiple pairwise comparisons were subjected to Bonferroni correction or Dunnett correction. One-sample t-tests were used to determine differences from chance. For data that did not fit

univariate assumptions, non-parametric tests were used or transformations were applied. For mouse behavior data, the square root transformation was applied to the USV and fear conditioning data. Chi-square or Fisher's exact tests were used to assess Myt1l mutation and sex association with categorical variables. Sex x genotype effects are reported where significant, otherwise data are reported and visualized collapsed for sex. The critical alpha value for all analyses was $p < .05$, unless otherwise stated. Figure schematics were generated using BioRender.

3.5 Acknowledgement

I thank Dr. Andrew Yoo, Dr. Brian Clark, Dr. Harrison Gabel, Dr. Kristen Kroll, Colin Florian, Nicole Hamagami, Diana Christian for technical assistance and scientific advice. Funding was provided by The Jakob Gene Fund, the Mallinckrodt Institute of Radiology at Washington University School of Medicine, McDonnell International Scholars Academy (J.C.), and the NIH: (R01MH107515, R01MH124808 to JDD, and NIH 5UL1TR002345 (ICTS) and P50 HD103525 (IDDRC)).

3.6 Figures and Tables

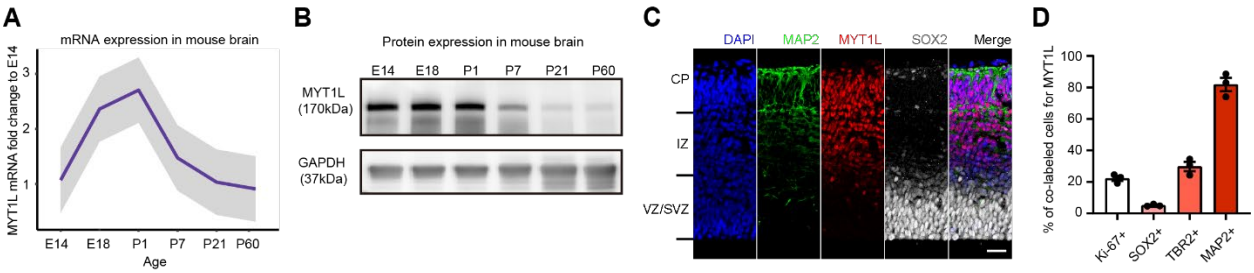

Figure 6: MYT1L's temporal and spatial expression pattern in the mouse brain.

(A) qRT-PCR revealed the trajectory of MYT1L mRNA expression across mouse brain development (n = 3). **(B)** Western blot showed a parallel trajectory of protein levels. **(C)** IF of MYT1L protein (red) revealed expression in MAP2+ (green) Cortical Plate (CP), intermediate zone (IZ), and a few in SOX2+ (white) progenitors in the Ventricular Zone/SubVentricular Zone (VZ/SVZ). Scale bar, 50 μm. **(D)** Quantification of MYT1L+ fraction within different cell types (n = 3).

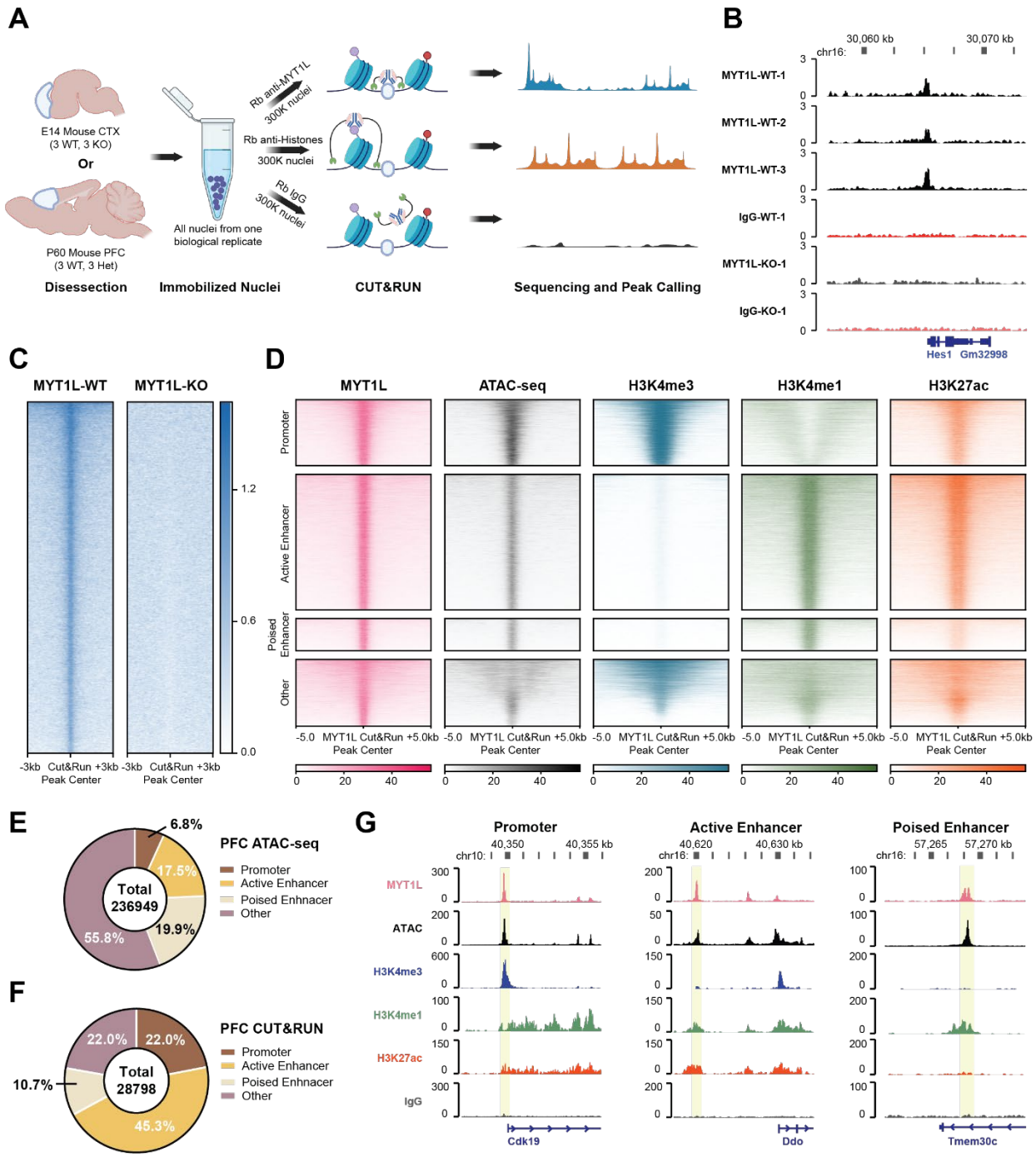

Figure 7: CUT&RUN identifies MYT1L specific binding targets in the mouse brain.

(A) Workflow of CUT&RUN experiments on E14 CTX and adult prefrontal Cortex (PFC). **(B)** Representative IGV tracks showing a reproducible MYT1L peak at the Hes1 promoter region in all 3 WT E14 biological replicates but not in IgG and KO samples. **(C)** Heatmaps of 20,305

MYT1L peaks called from the merged bam file. MYT1L CUT&RUN signals were diminished in the KO. **(D)** Heatmaps of CUT&RUN signals of MYT1L, IgG, and histones at MYT1L bound regions in PFC. **(E)** Annotations of PFC ATAC-seq peaks show the genome-wide distribution of promoters, active enhancers, and poised enhancers in open chromatin regions. **(F)** Annotations of MYT1L targets in PFC show MYT1L mainly binds to active enhancers. **(G)** Representative genome tracks of MYT1L bound promoter (left), active enhancer (middle), and poised enhancer (right).

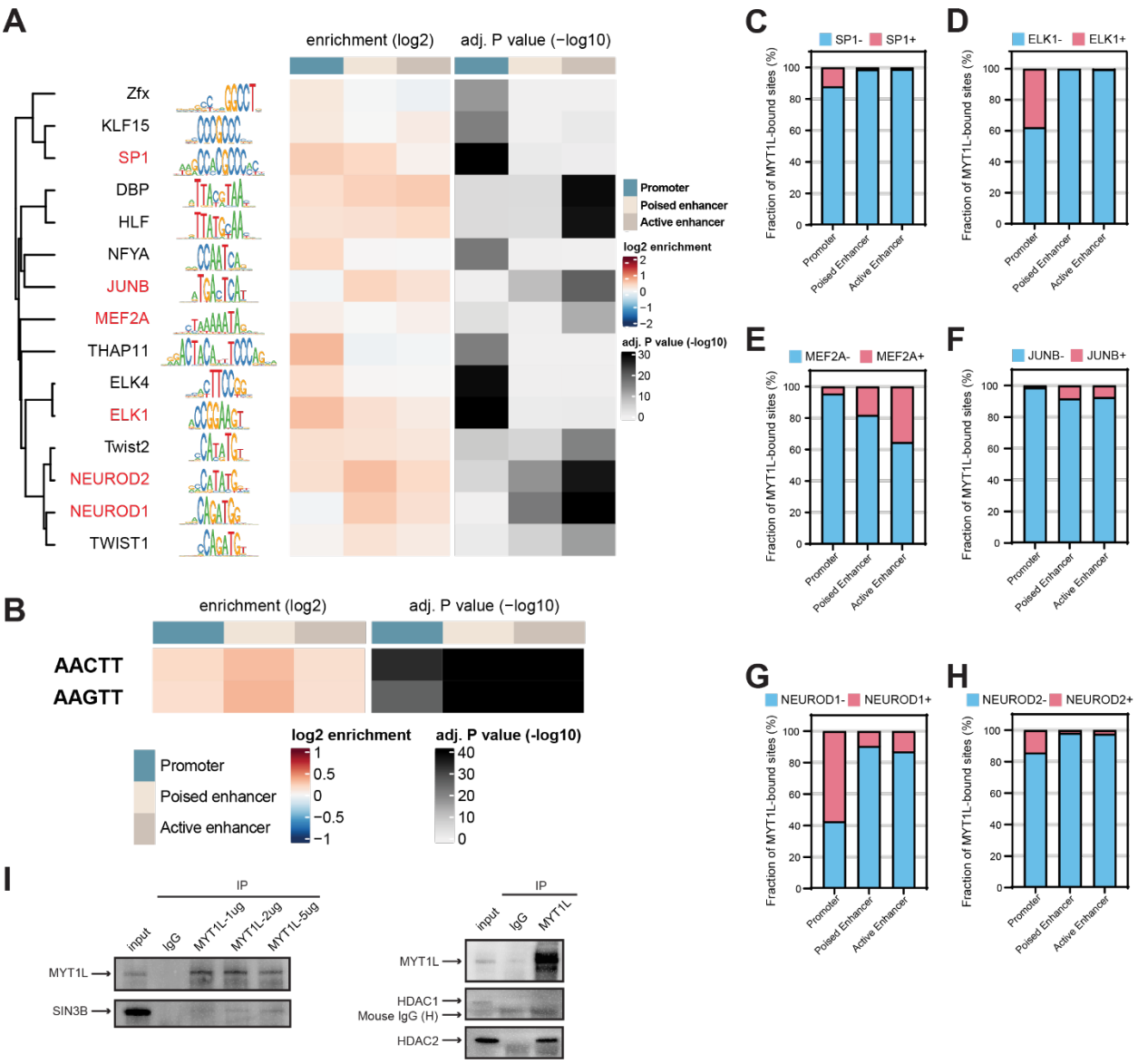

Figure 8: MYT1L co-occupies with different sets of TFs at promoter and enhancer regions. **(A)** monaLisa motif analysis revealed that MYT1L co-occupies with transcriptional activators such as ELK1 at promoter regions, while it co-occupies with neurogenic TFs such as MEF2A at enhancer regions. **(B)** Both MYT1L bound promoters and enhancers are significantly enriched for MYT1L core binding motif, AAGTT. **(C)** Overlapping between MYT1L Cut&Run targets and TFs ChIP-seq peaks showed that more MYT1L promoter targets were also bound by transcriptional activators like SP1 and **(D)** ELK1 than enhancer targets, while more enhancer

targets were bound by **(E)** the neurogenic TF MEF2A and **(F)** activity dependent gene JUNB. **(G)** NEUROD1 and **(H)** NEUROD2 have stronger presence at MYT1L promoter targets than enhancer targets. **(I)** MYT1L co-immunoprecipitated with SIN3B and HDAC2 but not with HDAC1/3 in WT mouse cortex.

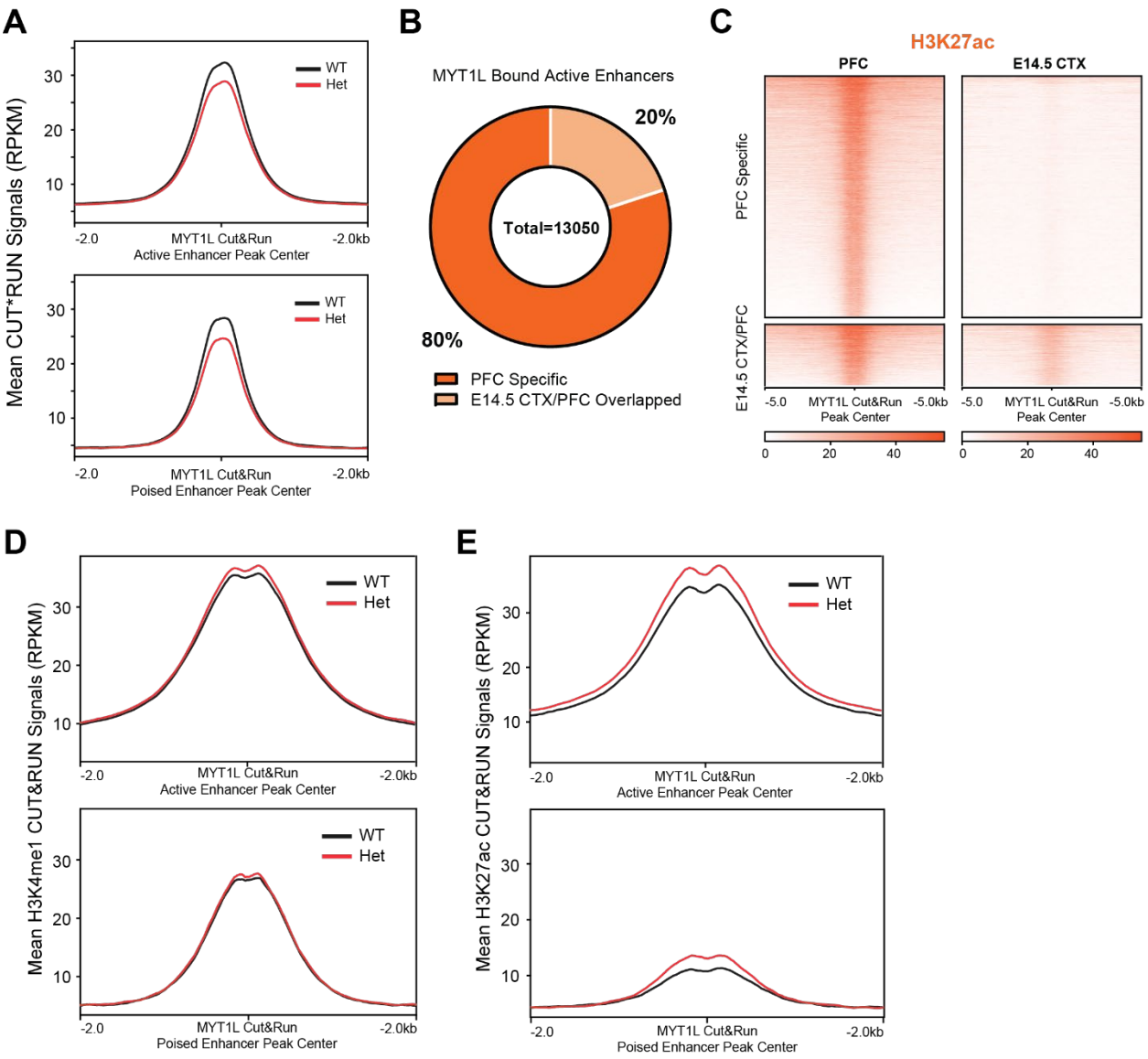

Figure 9: MYT1L suppresses enhancers activities by erasing active histone marks.

(A) Mean MYT1L CUT&RUN signals showed decreased MYT1L binding at enhancers in Het PFC. **(B)** Majority of MYT1L bound active enhancers are PFC specific. **(C)** Heatmaps of MYT1L bound active enhancers in PFC. **(D)** MYT1L loss increases its bound active enhancers but not poised enhancers' chromatin accessibility. **(E)** MYT1L loss increases H3K4me1 levels at MYT1L bound active enhancers but does not significantly increase H3K4me1 levels at MYT1L bound

poised enhancers. **(F)** MYT1L loss increases both its bound active and poised enhancers' H3K27ac levels.

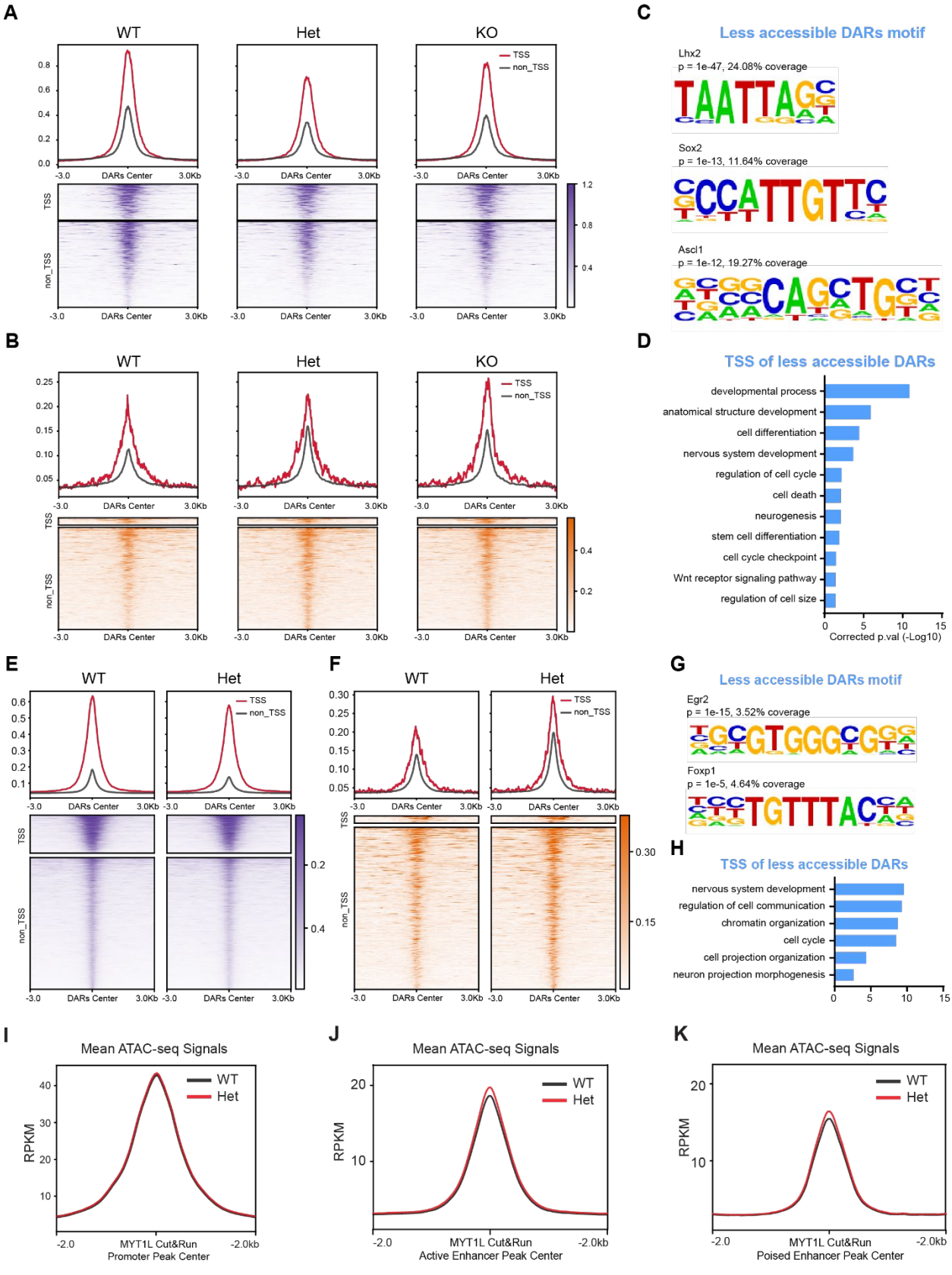
A
WT
Het
KO
TSS
non_TSS
DARs Center
3.0Kb
B
C
Less accessible DARs motif
Lhx2
p = 1e-47, 24.08% coverage
Sox2
p = 1e-13, 11.64% coverage
Ascl1
p = 1e-12, 19.27% coverage
D
TSS of less accessible DARs
developmental process
anatomical structure development
cell differentiation
nervous system development
regulation of cell cycle
cell death
neurogenesis
stem cell differentiation
cell cycle checkpoint
Wnt receptor signaling pathway
regulation of cell size
Corrected p.val (-Log10)
E
F
G
Less accessible DARs motif
Egr2
p = 1e-15, 3.52% coverage
Foxp1
p = 1e-5, 4.64% coverage
H
TSS of less accessible DARs
nervous system development
regulation of cell communication
chromatin organization
cell cycle
cell projection organization
neuron projection morphogenesis
I
Mean ATAC-seq Signals
RPKM
WT
Het
MYT1L Cut&Run
Promoter Peak Center
J
Active Enhancer Peak Center
K
Poised Enhancer Peak Center

Figure 10: MYT1L loss leads to chromatin accessibility changes in the mouse brain.

(A) Less and **(B)** more-accessible regions in *MYT1L* mutant E14 mouse cortex identified by ATAC-seq (FDR<.1). **(C)** Homer motif analysis on less-accessible DARs over more-accessible DARs. **(D)** GO analysis on less-accessible DARs associated genes showed the disruption of neurodevelopmental programming in mutants. **(E)** Less and **(F)** more-accessible regions in adult Het mouse PFC identified by ATAC-seq (FDR<.1). **(G)** Homer motif analysis on less-accessible DARs over more-accessible DARs. **(H)** GO analysis on DAR associated genes showed the dysregulation of neurodevelopmental programming in adult Het mouse PFC. **(I)** No chromatin accessibility change was observed at MYT1L bound promoters. **(J)** MYT1L loss increases its bound active enhancers but not **(K)** poised enhancers' chromatin accessibility.

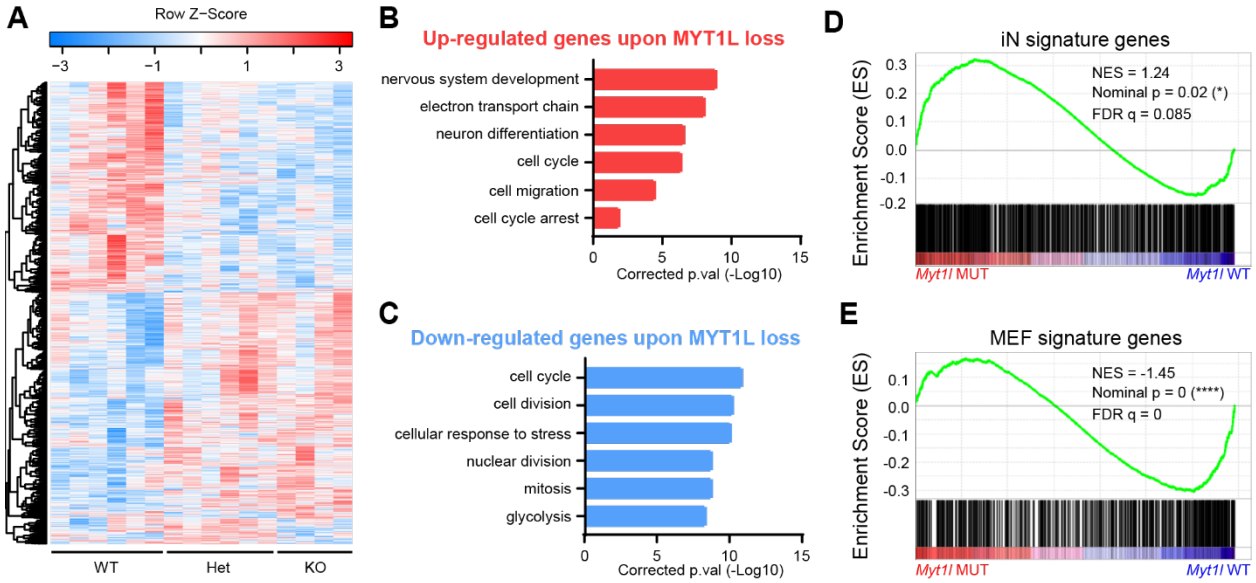

Figure 11: MYT1L leads to early activation of differentiation programs and repression of proliferation programs in the embryonic cortex.

(A) Heatmap for differential gene expression in mutants (FDR<.1). **(B)** GO analysis on DEGs revealed an upregulation of early neuronal differentiation pathways and **(C)** a downregulation of cell proliferation programs. **(D)** GSEA analysis found iN signature genes increased expression while **(E)** MEF genes decreased expression in mutant cortex.

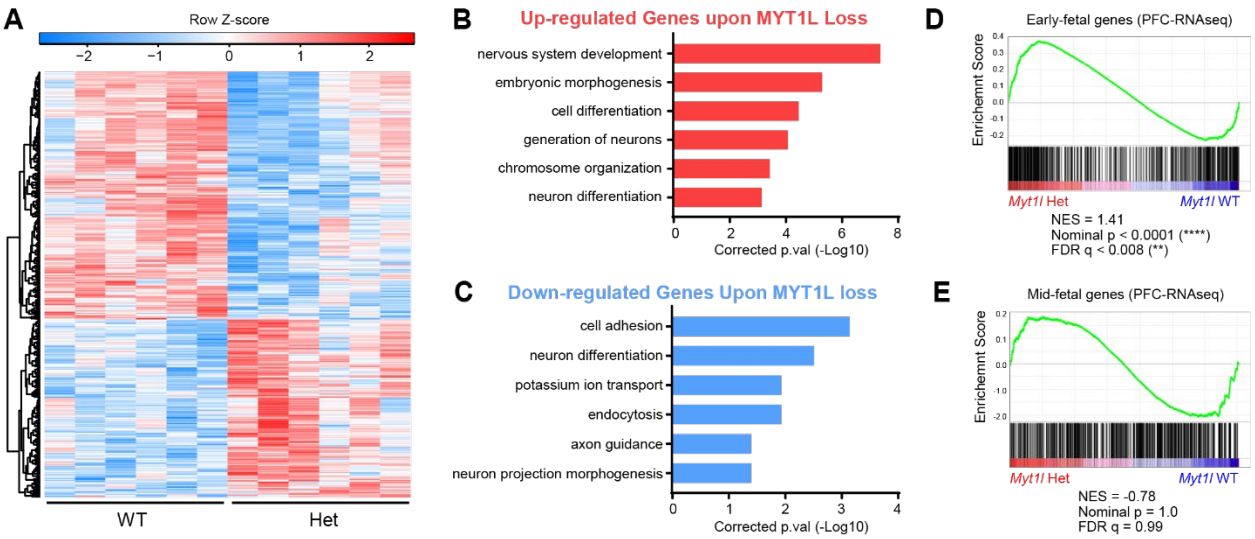

Figure 12: MYT1L loss leads to persistent activation of early neuronal development programs.

(A) Heatmap for differential gene expression in adult Het mouse PFC (FDR<.1). **(B)** GO analysis on DEGs revealed an upregulation of early neurodevelopmental pathways and **(C)** a down-regulation of neuron maturation and functions. **(D)** GSEA analysis found "early-fetal" genes increased their expression while **(E)** "mid-fetal" genes remained unchanged in adult Het mouse PFC compared.

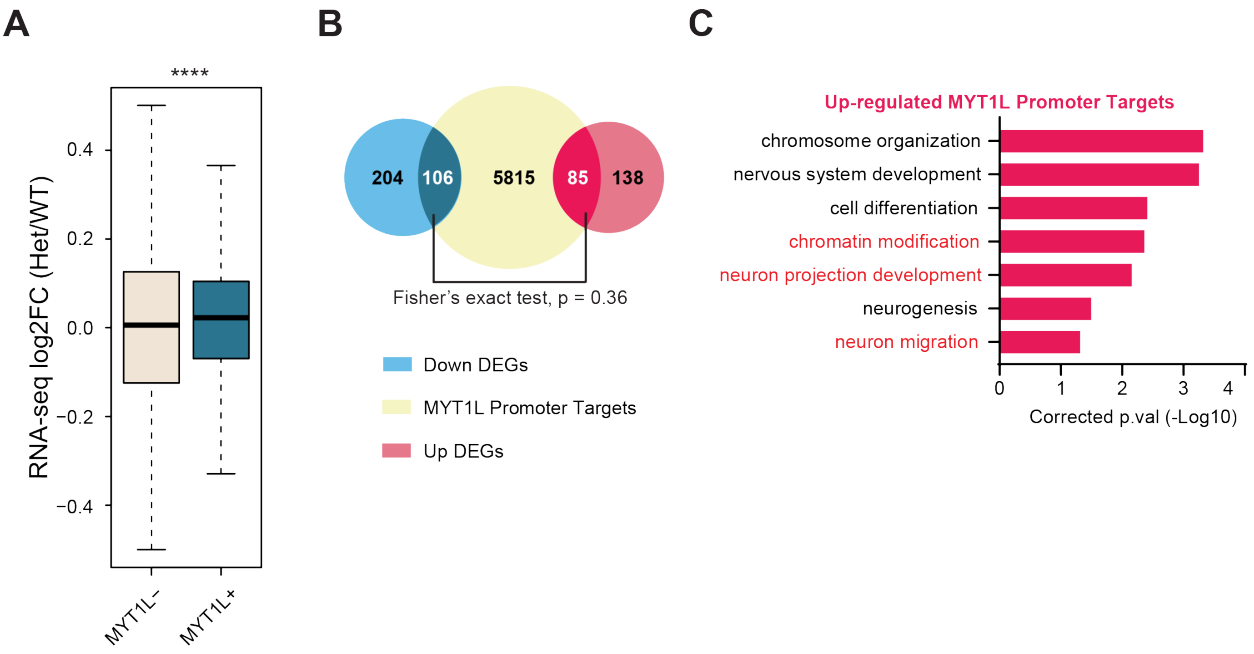

Figure 13: MYT1L directly binds to promoters that are associated with early neuronal development genes and suppresses their expression.

(A) MYT1L loss increases its promoter targets' expression in PFC. **(B)** Venn Diagram showing the overlaps among dDEGs, MYT1L Promoter targets, and uDEGs, and no biased overlap was observed (p = 0.36). **(C)** GO analysis on 85 uDEGs whose promoters are bound by MYT1L.

*See **Table S2** for statistical test details.*

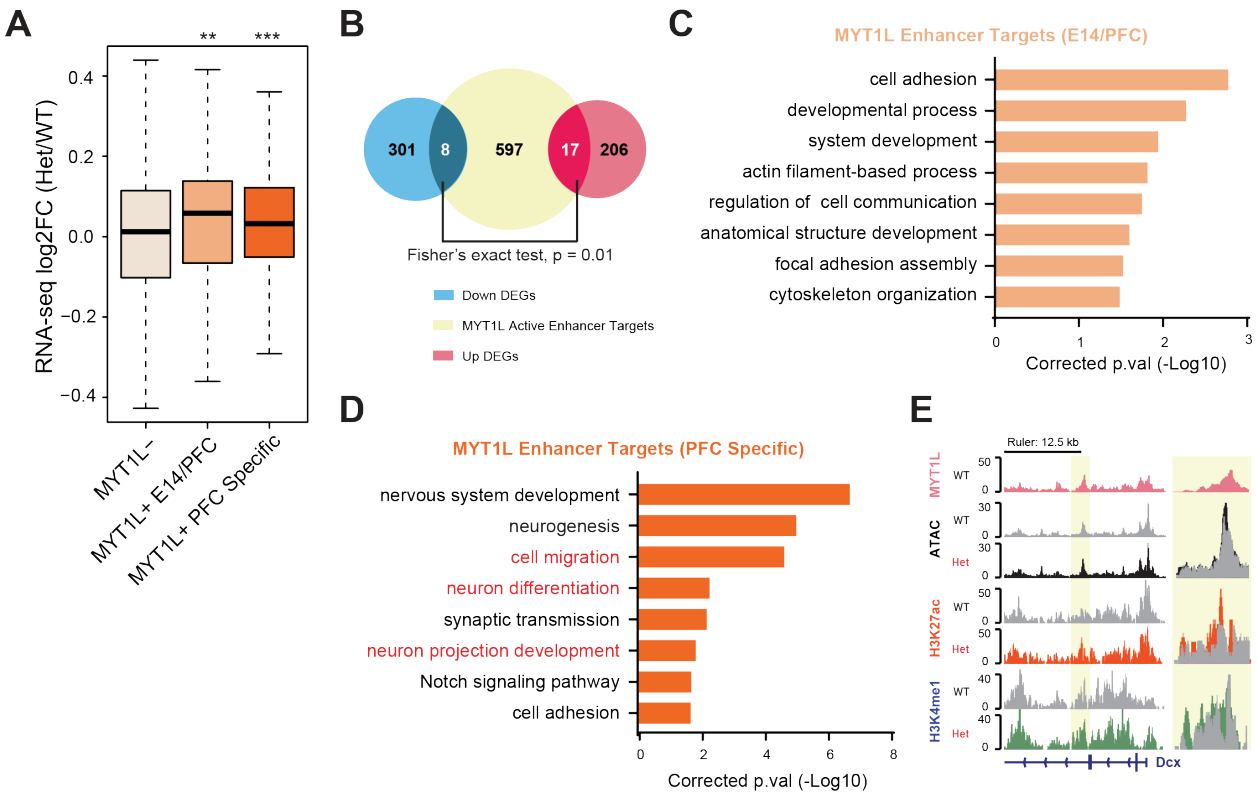

Figure 14: MYT1L suppresses enhancers that regulate neuronal migration and neuron projection development.

(A) MYT1L loss increases both its bound active and poised enhancers' H3K27ac levels. **(B)** MYT1L active enhancer target genes show increased expression in Het PFC. **(C)** Venn Diagram showing the overlaps among dDEGs, MYT1L active enhancer targets, and uDEGs, and there are more overlaps between MYT1L active enhancer targets and uDEGs than dDEGs (p = 0.01). **(D)** GO analysis on genes regulated by MYT1L bound E14 CTX/PFC overlapped active enhancers. **(I)** GO analysis on genes regulated by MYT1L bound PFC-specific active enhancers. **(E)** Representative genome browser track shows MYT1L-bound Dcx active enhancer has higher ATAC-seq signals, H3K4me1 and H3K27ac levels in Het PFC than WT. *p<0.05, **p<0.01, ***p<0.001, ****p<0.0001.

*See **Table S2** for statistical test details.*

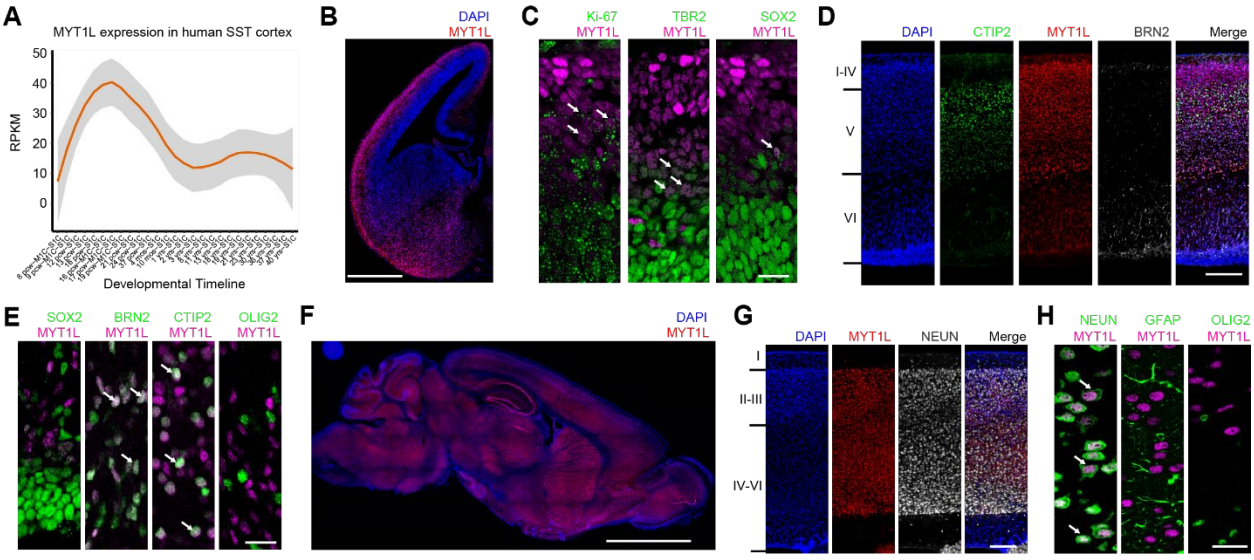

Supplemental Figure 6: MYT1L protein is expressed in neuronal lineages, peaking during neuronal maturation.

(A) MYT1L expression across human brain development (somatosensory cortex, data from BrainSpan, https://www.brainspan.org/) also showed peak expression during neuronal maturation, yet sustained expression in adulthood. **(B)** Coronal section of E14 brain immunofluorescence showed MYT1L expression in zones of maturing neurons throughout the brain. **(C)** Immunofluorescence of IZ (Intermediate Zone) in E14 showed transition from cycling (Ki-67+), SOX2, and TBR2 positive progenitors to MYT1L positive cells. Only a small portion of cells showed overlap of these makers. **(D)** MYT1L was expressed in neurons across upper (CTIP2+, green) and lower (BRN+, white) layers of the P1 mouse cortex, **(E)** but not in radial glia (SOX2+) and oligodendrocytes (OLIG2+). **(F)** Sagittal section of adult (P60) mouse brain immunofluorescence showed broad expression of MYT1L in cortex, hippocampus, hypothalamus, striatum, as well as cerebellum. **(G & H)** MYT1L staining in P60 mouse cortex showed its exclusive expression in neurons (NEUN+) but not in astrocytes (GFAP+) and oligodendrocytes (OLIG2+).

Scale bars, 500 μm in B, 20 μm in C, 250 μm in D, 20 μm in E, 3 Mm in F, 200 μm in G, 20 μm in H, and 50 μm in J.

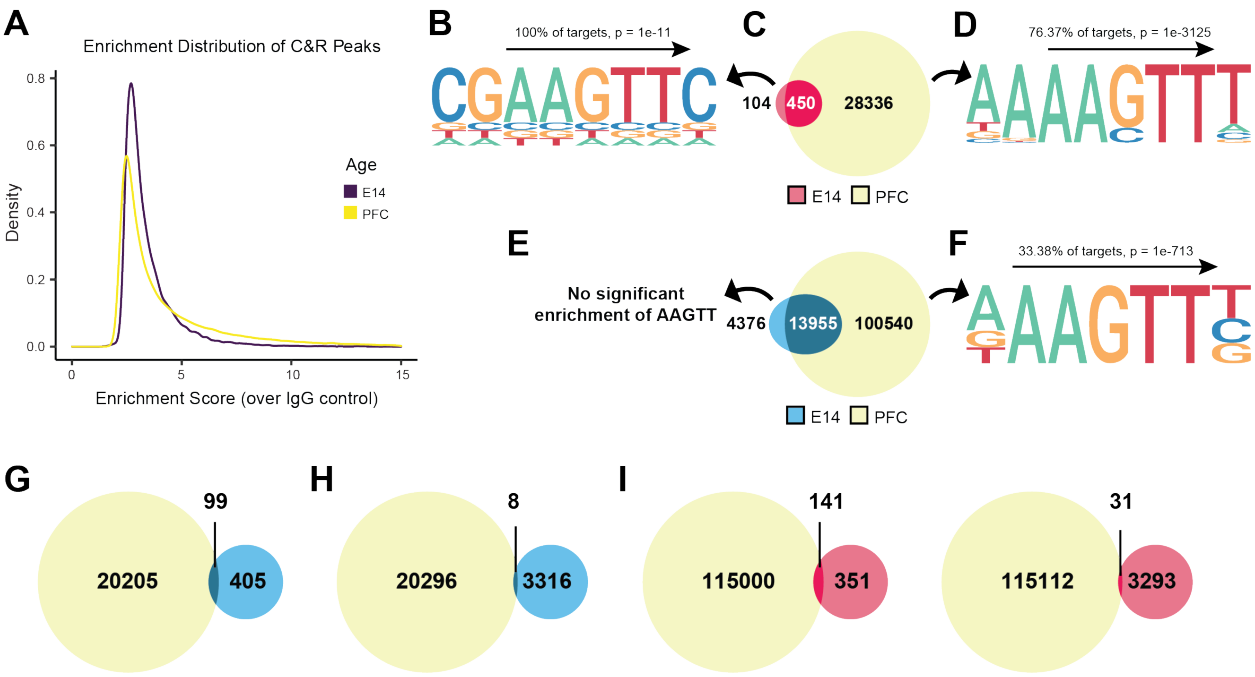

Supplemental Figure 7: CUT&RUN is more efficient for MYT1L binding profiling on P60 PFC than on E14 CTX.

(A) MYT1L CUT&RUN peaks called from the merged PFC alignment file showed decreased density of low enrichment peaks but increased density of high enrichment peaks compared to E14 CUT&RUN peaks. **(B)** Homer de novo motif finding shows significant enrichment of MYT1L core binding motif AAGTT in E14 CUT&RUN intersected peaks. **(C)** Overlaps between MYT1L PFC and E14 intersected CUT&RUN peaks. **(D)** Homer de novo motif finding shows significant enrichment of MYT1L core binding motif AAGTT in PFC CUT&RUN intersected peaks. **(E)** Overlaps between MYT1L PFC and E14 CTX CUT&RUN peaks called from the merged alignment file. **(F)** Homer de novo motif finding shows significant enrichment of MYT1L core binding motif AAGTT in PFC CUT&RUN peaks called from the merged alignment file. **(G)** No significant overlap was found between MYT1L E14 CTX CUT&RUN peaks called from the merged alignment file and MYT1L ChIP-seq peaks from the mouse E14 brain. **(H)** No significant overlap was found between MYT1L E14 CTX CUT&RUN peaks called from the merged

alignment file and MYT1L ChIP-seq peaks from MEFs overexpressing MYT1L, BRN2, and ASCL1. **(I)** No significant overlap was found between MYT1L PFC CUT&RUN peaks called from the merged alignment file and MYT1L ChIP-seq peaks from the mouse E14 brain. **(J)** No significant overlap was found between MYT1L PFC CUT&RUN peaks called from the merged alignment file and MYT1L ChIP-seq peaks from MEFs overexpressing MYT1L, BRN2, and ASCL1. Color code: CUT7RUN (yellow), MEFs ChIP-seq (blue), and E14 brain ChIP-seq (red).

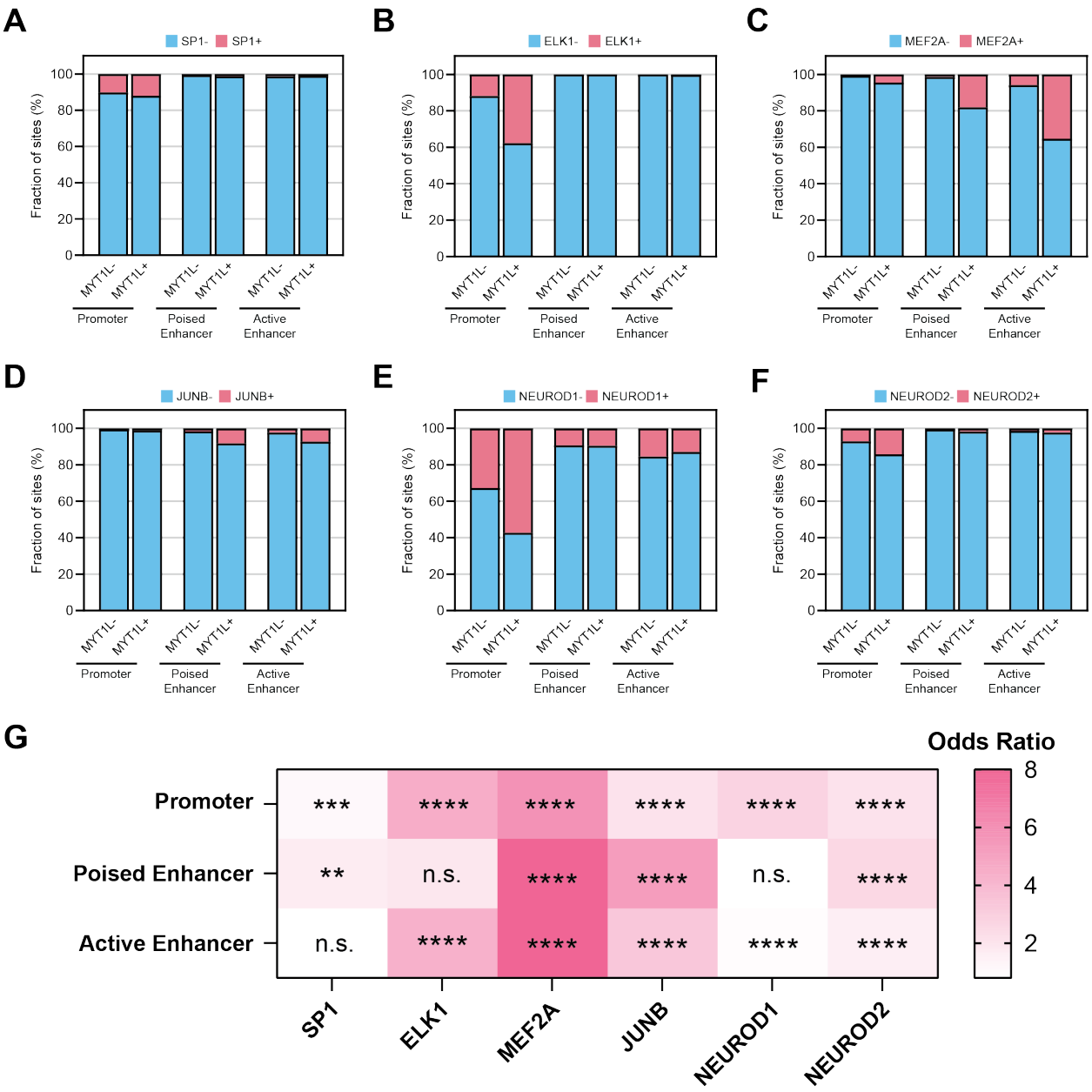

Supplemental Figure 8: MYT1L co-occupies with a different set of transcriptional factors at promoters and enhancers.

(A) MYT1L+ promoters have a significantly higher percentage of SP1 binding compared to MYT1L- promoters, while no obvious difference was observed in enhancers. The same pattern was observed for **(B)** ELK1 as well. **(C)** MYT1L+ enhancers have a significantly higher percentage of MEF2A binding compared to MYT1L- promoters, while no big difference was

observed in promoters. The same pattern was observed for **(D)** JUNB as well. **(E)** MYT1L+ promoters have a significantly higher percentage of NEUROD1 binding compared to MYT1L- promoters, while no obvious difference was observed in enhancers. The same pattern was observed for **(F)** NEUROD2 as well. **(G)** Fisher's exact test showed different TFs' enrichment in MYT1L+ over MYT1L- genomic regions. *p<0.05, **p<0.01, ***p<0.001, ****p<0.0001.

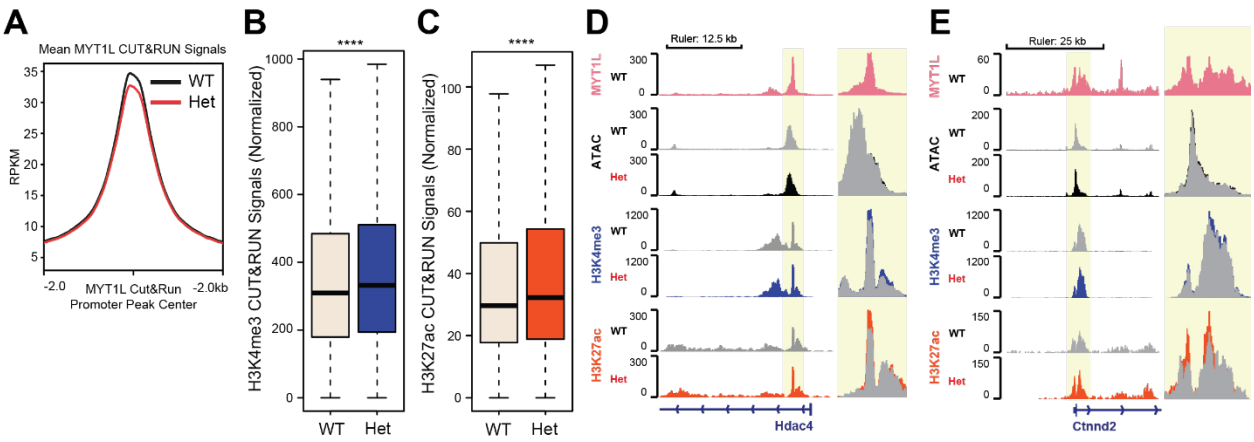

Supplemental Figure 9: MYT1L loss increases H3K4me3 and H3K27ac levels at promoters. **(A)** Mean MYT1L CUT&RUN signals showed decreased MYT1L binding at promoters in Het PFC. **(B)** MYT1L Het PFC has higher levels of H3K4me3 at MYT1L promoter targets compared to WTs. **(C)** MYT1L Het PFC has higher levels of H3K27ac at MYT1L promoter targets compared to WTs. **(D)** Representative genome browser track of MYT1L bound Hdac4 promoter. **(E)** Representative genome browser track of MYT1L bound Ctnnd2 promoter. *p<0.05, **p<0.01, ***p<0.001, ****p<0.0001.

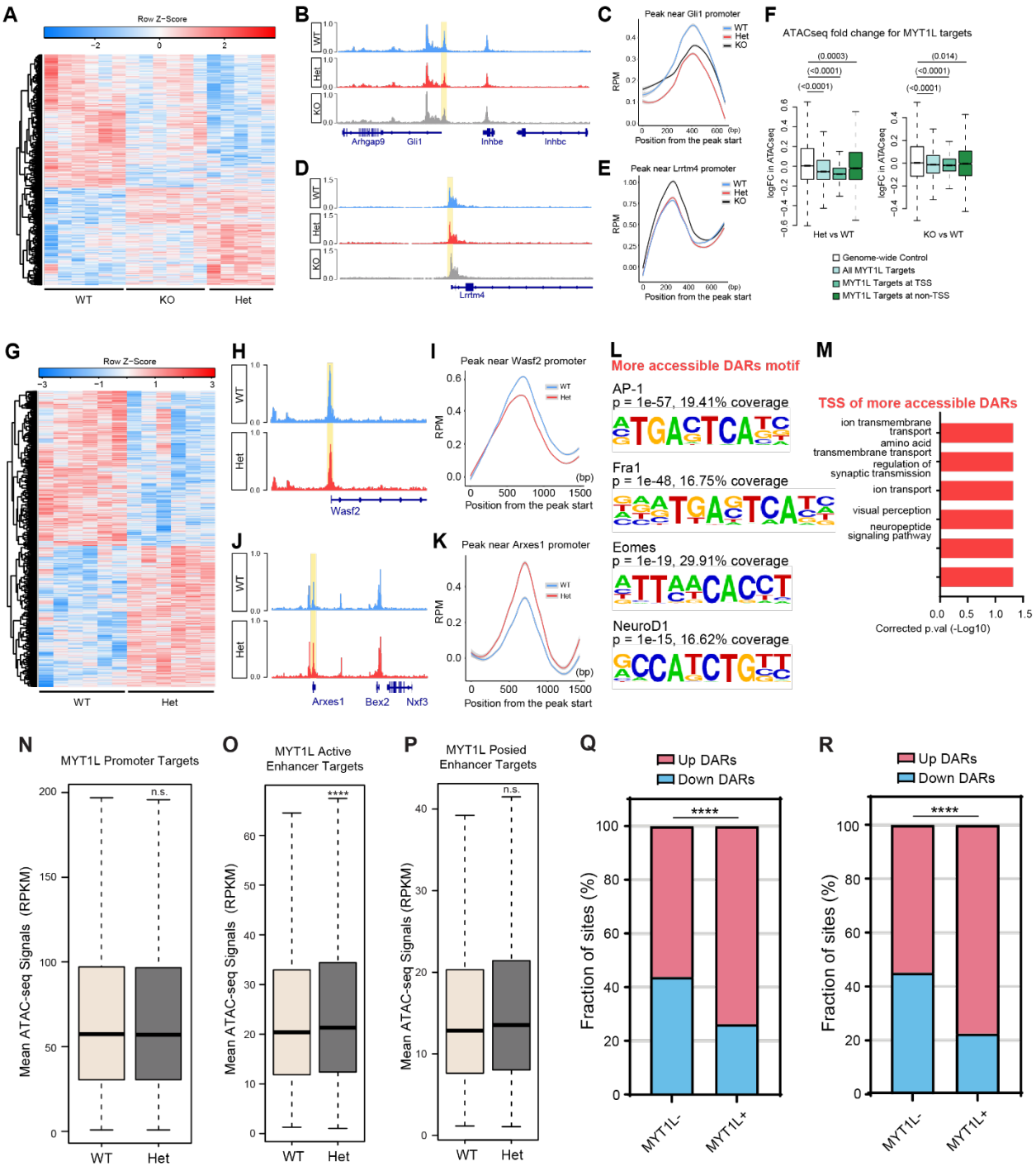

Supplemental Figure 10: Chromatin Accessibility analysis define molecular consequences of MYT1L loss in the developing and adult brain.

(A) Heatmap for differential accessible regions in mutants (FDR < .05). **(B)** Representative peak (50kb interval) and its **(C)** average coverage (lines) and 95% confidence interval (shading) across

biological replicates of less accessible DAR found in ATAC-seq (highlighted in yellow) near the Gli1 promoter region. **(D)** Representative peak (50kb interval) and its **(E)** average coverage (lines) and 95% confidence interval (shading) across biological replicates of more accessible DAR found in ATAC-seq (highlighted in yellow) near the Lrrtm4 promoter region. **(F)** ATAC-seq fold changes for MYT1L ChIP targets showed a loss of accessibility at MYT1L bound regions in both Het and KO E14 mice cortex. **(G)** Heatmap for differential accessible regions in Hets (FDR < .05). **(H)** Representative peak (50kb interval) and its **(I)** average coverage (lines) and 95% confidence interval (shading) across biological replicates of a DAR with less accessibility in Hets (highlighted in yellow) near the Wasf2 promoter region. **(J)** Representative peak (50kb interval) and its **(K)** average coverage (lines) and 95% confidence interval (shading) across biological replicates of a DAR that was more accessible in Hets (highlighted in yellow) near the Arxes1 promoter region. **(L)** Motif analysis comparing more-accessible DARs to less-accessible DARs. **(M)** GO analysis on DAR associated genes showed the dysregulation of neuronal functions in adult Het mouse PFC. **(N)** MYT1L loss did not alter its bound promoters' chromatin accessibility. **(O)** MYT1L loss increases its bound active (left) but not **(P)** poised (right) enhancers' chromatin accessibility. **(Q)** MYT1L bound active enhancer DARs have a higher percentage of DARs that increase accessibility than MYT1L unbound active enhancer DARs. **(R)** MYT1L bound poised enhancer DARs have a higher percentage of DARs that increase accessibility than MYT1L unbound poised enhancer DARs. *p<0.05, **p<0.01, ***p<0.001, ****p<0.0001.

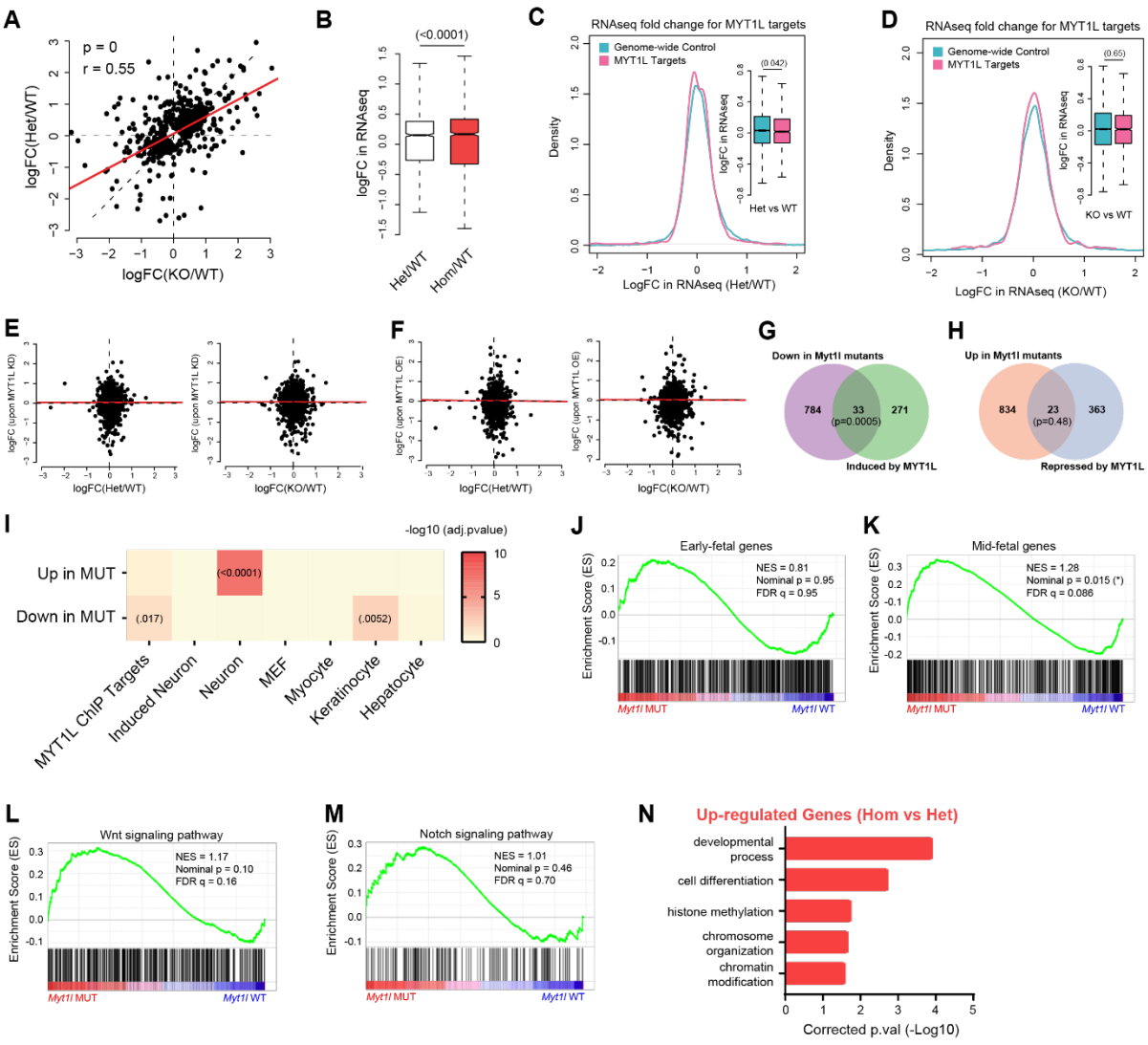

Supplemental Figure 11: Comparison of transcriptomic changes between *in vitro* overexpression and embryonic *in vivo* knockout models.

(A) Fold changes of DEGs correlated well between *Myt1l* Het and KO samples. Regression line is shown in red. **(B)** Total loss (KO) of MYT1L had larger effects on fold changes of DEGs compared to partial (Het) MYT1L loss. **(C)** RNA-seq fold changes for MYT1L targeted genes showed subtle downregulation in Het and **(D)** KO E14 CTX expression data sets. **(E)** Correlation of DEGs' expression changes between Het (left) / KO (right) CTX RNA-seq and primary hippocampal neuron culture MYT1L knockdown (KD) RNA-seq experiments. **(F)** Correlation of DEGs'

expression changes between Het (right) / KO (left) CTX RNA-seq and MYT1L OE RNA-seq experiments. **(G)** Venn diagram of overlap between downregulated DEGs in E14 CTX RNA-seq and MYT1L induced genes *in vitro*. **(H)** Venn diagram of overlap between upregulated DEGs in E14 CTX RNA-seq and MYT1L repressed genes *in vitro*. **(I)** Overlap of DEGs and different cell-type signature gene lists. Activated genes upon MYT1L loss significantly overlapped neuronal signature genes while genes decreasing expression overlapped with MYT1L embryonic ChIP targets and keratinocyte signature genes. **(J)** GSEA analysis revealed human "early fetal" genes are not categorically affected in mutants while **(K)** "mid-fetal" genes tended to be up-regulated in mutant E14 mouse cortex. **(L)** GSEA analysis showed no significant categorical shift of Wnt signaling and **(M)** Notch signaling pathway gene expression in *Myt1l* mutant CTX. **(N)** GO analysis revealed a further up-regulation of chromatin modification pathways in KO mice compared to Het.

Boxplots are plotted with thick horizontal lines as group medians, boxes 25th – 75th percentiles, and whiskers 1.5 x IQR. See ***Table S2*** *for statistical test details.*

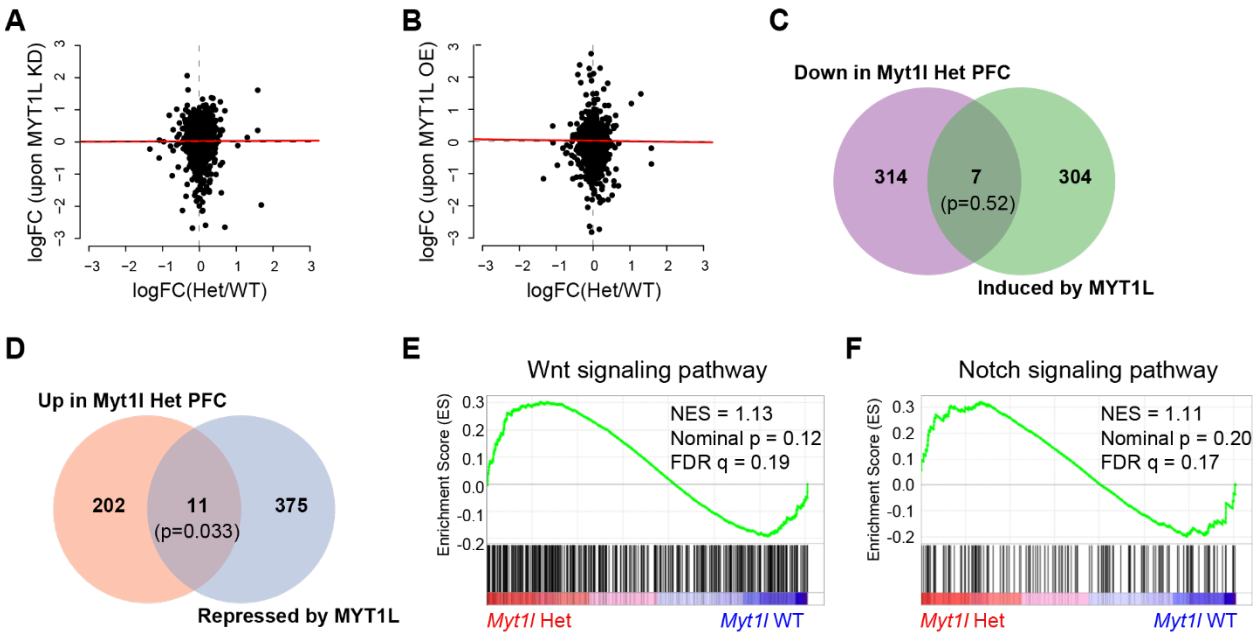

Supplemental Figure 12: Comparison of transcriptomic changes between *in vitro* overexpression and adult *in vivo* knockout models.

(A) Correlation of DEGs' expression changes between Het PFC RNA-seq and published primary hippocampal neuron culture MYT1L knockdown (KD) RNA-seq experiments. **(B)** Correlation of DEGs' expression changes between Het PFC RNA-seq and published MEF MYT1L overexpression (OE) RNA-seq experiments. **(C)** Overlap between downregulated DEGs in PFC RNA-seq and MYT1L induced genes *in vitro*. **(D)** Overlap between upregulated DEGs in PFC RNA-seq and MYT1L repressed genes *in vitro*. **(E)** GSEA analysis showed normal expression of Wnt signaling and **(F)** Notch signaling pathway in *Myt1l* Het PFC.

*See **Table S2** for statistical test details.*

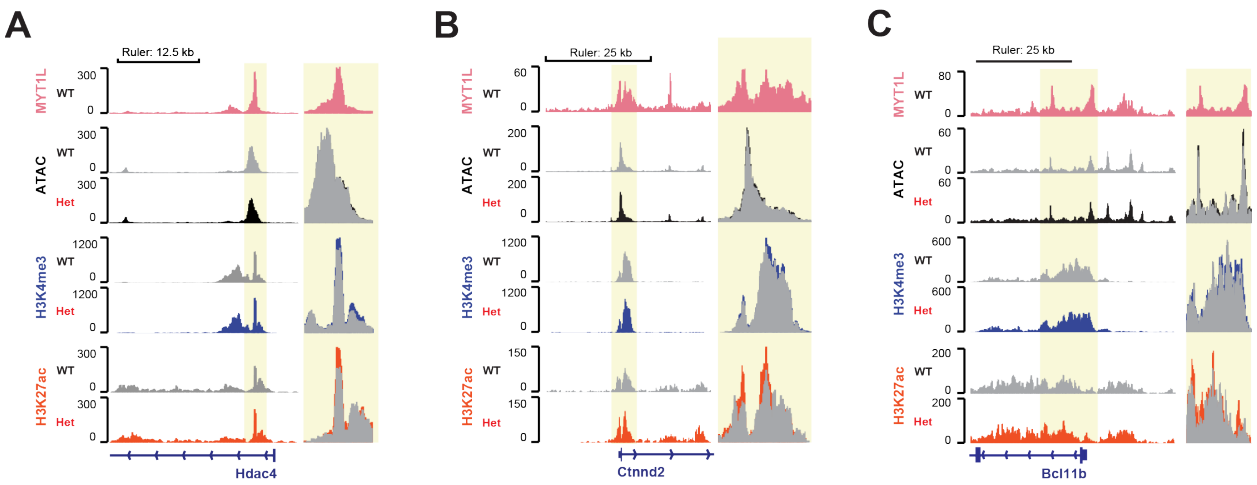

Supplemental Figure 13: Genome browser tracks of representative MYT1L bound promoters associated with neuronal developmental genes.

(A) Representative genome browser track shows MYT1L-bound *Bcl11b* promoter. **(B)** Representative genome browser track of MYT1L bound *Hdac4* promoter. **(C)** Representative genome browser track of MYT1L bound *Ctnnd2* promoter.

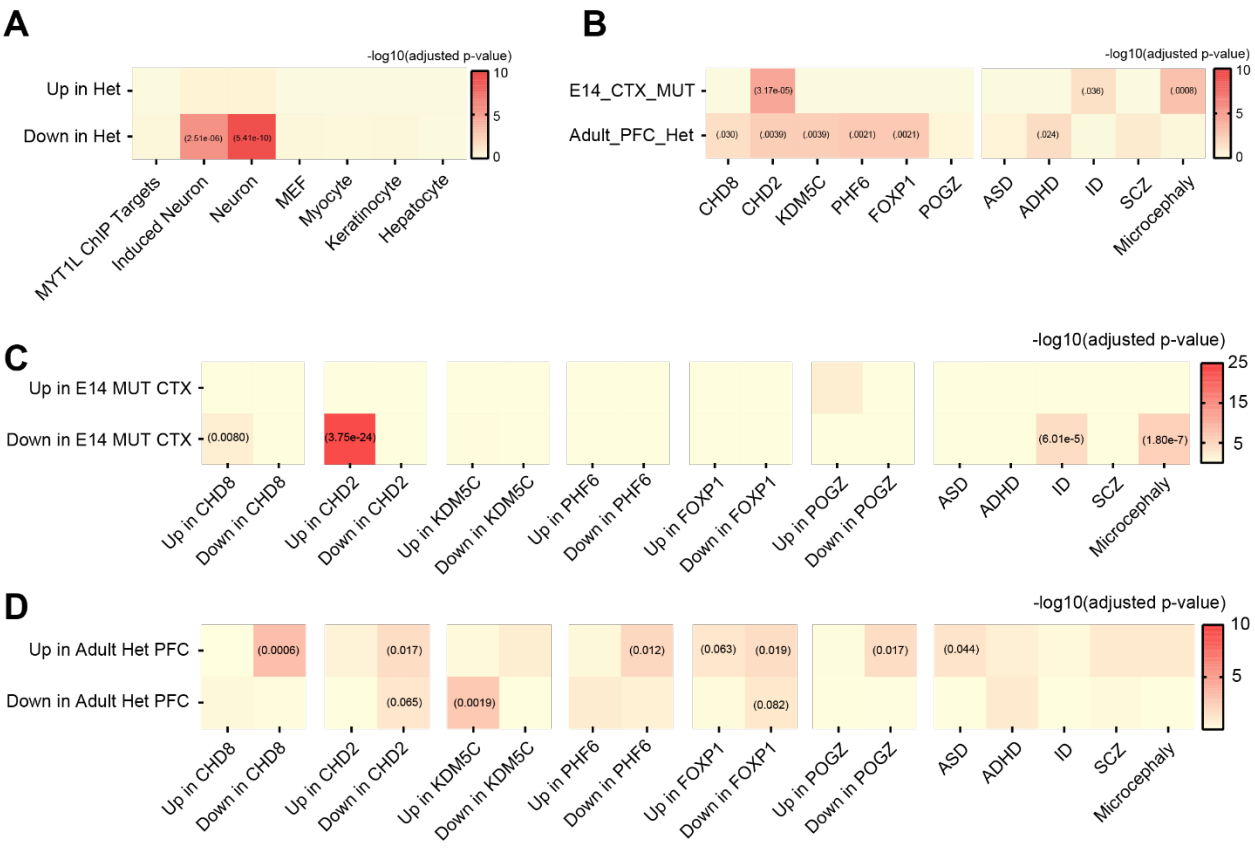

Supplemental Figure 14: DEGs in adult Het PFC are implicated in other ID/ASC mouse models and human genetic data sets.

(A) Repressed genes upon MYT1L loss in PFC significantly overlapped with induced neuron and neuronal signature genes. **(B)** MYT1L regulated genes were implicated in other ID/ASC mouse models and human genetic data sets. **(C-D)** MYT1L regulated genes were implicated in other ID/ASC mouse models and human genetic data sets.

*See **Table S2** for statistical test details.*

Supplemental Table 2. Statistical analyses for Chapter 3.

FIG	VARIABLE	COMPARISON	STATISTICAL TEST	OUTPUT
S9B	Normalized H3K4me3 signals	genotype	Mann-Whiteny U	p = 2.31e-06
S9C	Normalized H3K27ac signals	genotype	Mann-Whiteny U	p = 2.82e-08
S10F	ATAC fold changes in E14 Het CTX	control vs all ChIP targets	Mann-Whiteny U	p =2.86e-54
	ATAC fold changes in E14 Het CTX	control vs ChIP targets (tss)	Mann-Whiteny U	p =.8.97e-91
	ATAC fold changes in E14 Het CTX	control vs ChIP targets (non-tss)	Mann-Whiteny U	p =0.0003
	ATAC fold changes in E14 Hom CTX	control vs all ChIP targets	Mann-Whiteny U	p = 4.68e-09
	ATAC fold changes in E14 Hom CTX	control vs ChIP targets (tss)	Mann-Whiteny U	p = 5.86e-10
	ATAC fold changes in E14 Hom CTX	control vs ChIP targets (non-tss)	Mann-Whiteny U	p = 0.014
S10N	Normalized ATACseq signals	genotype	Mann-Whiteny U	p = 0.7634
S10O	Normalized ATACseq signals-Poised Enhancer	genotype	Mann-Whiteny U	p = 0.016
S10P	Normalized ATACseq signals-Active Enhancer	genotype	Mann-Whiteny U	p = 4.43e-08
S10Q	MYT1L positive DARs	MYT1L+/MYT1L-	Fisher's exact test	p < 0.0001
S10R	MYT1L positive DARs	MYT1L+/MYT1L-	Fisher's exact test	p < 0.0001
S11B	RNAseq fold changes	Het vs Hom	Kolmogorov-Smirnov test	p =8.84e-12
S11C	RNAseq fold changes in E14 Het CTX	control vs ChIP targets	Mann-Whiteny U	p =.059
S11D	RNAseq fold changes in E14 Hom CTX	control vs ChIP targets	Mann-Whiteny U	p =.65
S11G	DEGs in different RNA-seq experiments	Down in *Myt1l* mutants vs induced by MYT1L	Hypergeometirc mapping	p =.0005
S11H	DEGs in different RNA-seq experiments	Up in *Myt1l* mutants vs repressed by MYT1L	Hypergeometirc mapping	p =.48
S12C	DEGs in different RNA-seq experiments	Down in *Myt1l* mutants vs induced by MYT1L	Hypergeometirc mapping	p =.52
S12D	DEGs in different RNA-seq experiments	Up in *Myt1l* mutants vs repressed by MYT1L	Hypergeometirc mapping	p =.033

13A	RNAseq fold changes in PFC	control vs CUT&RUN targets	Mann-Whiteny U	p=3.25e-07
14A	RNAseq fold changes PFC/E14 Active Enhancer targets in PFC	control vs CUT&RUN	Mann-Whiteny U	p = 0.0077
	RNAseq fold changes PFC Active Enhancer targets in PFC	control vs CUT&RUN	Mann-Whiteny U	p = 0.0009

Chapter 4: Cellular Functions of MYT1L in the Mouse Brain across Development

Jiayang Chen, Mary E. Lambo, Nicole A. Fuhler, Dora R. Tabachnick, Lucy Tian, Kevin Noguchi, Keith B. Hengen, Susan E. Maloney, Joseph D. Dougherty

Adapted From:

A MYT1L syndrome mouse model recapitulates patient phenotypes and reveals altered brain development due to disrupted neuronal maturation

Chen, J., Lambo, M.E., Ge, X., Dearborn, J.T., Liu, Y., McCullough, K.B., Swift, R.G., Tabachnick, D.R., Tian, L., Noguchi, K., et al. (2021). A MYT1L syndrome mouse model recapitulates patient phenotypes and reveals altered brain development due to disrupted neuronal maturation. Neuron vol. 109,23 (2021): 3775-3792.e14.

And:

MYT1L is required for suppressing earlier neuronal development programs in the adult mouse brain

Chen, J., Fuhler, N.A., Noguchi, K., Dougherty, J.D. (2022). MYT1L is required for suppressing earlier neuronal development programs in the adult mouse brain. bioRxiv 2022.10.17.512591; doi: https://doi.org/10.1101/2022.10.17.512591, in revision, Genome Research

4.1 Introduction

The previous chapter stablished MYT1L's role in mediating cell proliferation and neuronal differentiation programs during CNS development on a molecular level. In this chapter, I sought to assess if this role is translated at the cellular and circuitry levels, and if cellular phenotypes line up with predictions from genetic studies. I first measured cell proliferation rates and the differentiation process in embryonic mouse cortex and compared how they were altered upon MYT1L loss. Then, synaptic functions as well as neuronal morphology in the juvenile mouse visual cortex were examined by electrophysiology and confocal microscopy. In addition, as indicated by multi-omics studies, histology was performed to test if MYT1L loss leads to cortical lamination anomalies. Lastly, based on current findings in this dissertation, I proposed molecular and cellular models of how MYT1L facilitates neuronal maturation and how MYT1L loss results in a smaller mouse brain, providing insights to human disease pathogenesis.

4.2 Results

4.2.1 MYT1L's functions during neuronal proliferation and differentiation in the developing mouse cortex

Precocious neuronal differentiation could reduce the progenitor pool and thus reduce cell production, resulting in a smaller brain. To validate the prediction from RNA-seq that MYT1L loss affects cell differentiation and proliferation, I first stained cell-stage markers in the E14 cortex (**Fig. 15A**). I found KOs have decreased apical progenitor (AP, SOX2+) density with normal intermediate progenitor (TBR2+) and postmitotic neuron (TBR1+) density compared with Hets and WTs (**Fig. 15C-E, S15A-C**). Even after normalizing SOX2+ cells to total cell number, there was still a trend towards fewer SOX2+ cells in KOs (**Fig. S15A,** p = .0528), indicating smaller AP

density can be independent of decreased total cell number (**Fig. 15B**). I also found the ratio of TBR2+/SOX2+ but not TBR1+/TBR2+ was increased in mutant mice (**Fig. S15D, E**). Overall, I saw a shift from early cell fate (SOX2+) to late cell fate (TBR2+/TBR1+) in *Myt1l* mutants (**Fig. 15F**), supporting the hypothesized precocious cell differentiation. Proliferating cells (Ki-67+) were also decreased in KOs (**Fig. 15G-I**), suggesting MYT1L loss affects cell proliferation. Therefore, I performed EdU labeling experiments to measure proliferation rates (**Fig. 15J**). I found that both Het and KO cortices have significantly fewer EdU+ cells (**Fig. 15K**), highlighting less proliferation in the mutant developing cortex.

Following mitosis, daughter cells either re-enter the cell cycle to expand the progenitor pool, or leave permanently and become neurons. Since decreased proliferation could be driven by a greater number of cells exiting the cell cycle, I quantified exiting by co-staining for recently proliferating cells (EdU+) that have lost Ki-67 (Q fraction; **Fig. 15L**) (Gompers et al. 2017). KOs had a significantly larger Q fraction (**Fig. 15M**). These results show that MYT1L loss perturbs cell proliferation and enhances cell cycle exit. This corresponds well to the RNA-seq, and provides the most parsimonious explanation for the smaller brains: precocious differentiation of some neural progenitors results in fewer proliferating cells and a decreased brain size in adults.

4.2.2 The roles of MYT1L in neuronal maturation and synaptic functions in the juvenile and adult mouse cortex

4.2.2.1 MYT1L haploinsufficiency disrupts postnatal neuronal physiology and spine maturity

Het mice showed deficits in transcriptional and chromatin states with a failure to achieve the mature profile of axonal development. Therefore, I asked whether this manifested in neurophysiological changes at the cellular level. In collaboration with the Hengen lab, I first

examined the passive membrane properties and cell morphology of layer 2/3 pyramidal neurons in the primary visual cortex (V1) at P21-23, an extensively studied system with similar cell types and mesoscale circuit connectivity to PFC (Oh et al. 2014; Tasic et al. 2018). Compared to age-matched WT neurons, Het neurons exhibited significantly depolarized resting membrane potentials (**Fig. 16A**), and decreased membrane resistance (**Fig. 16B**), which are changes that affect membrane excitability in opposite directions. We also observed a smaller time constant in Hets that was explained by the decrease in membrane resistance and capacitance (**Fig. 16C, D**), which could arise from a decrease in total cell surface area or altered ion channel composition. In total, MYT1L haploinsufficiency disrupts the passive physiological properties of pyramidal neurons.

To ask whether the change in capacitance was a direct result of cell surface area, I examined the somatic size of the patched neurons. We dye filled the patched neurons and examined them with confocal miscroscopy after the experiment. A previous shRNA study on differentiating NPCs revealed larger cell bodies yet decreased neurites (Kepa et al. 2017). Here, with controlled haploinsufficiency *in vivo*, I found that MYT1L loss changed neither neuron soma size (**Fig. 16E, S16A, B**) nor many dendritic morphological properties, including length, nodes, as well as complexity (**Fig. S16D-G**). I found a small but not significant decrease of total dendrite numbers in Het neurons (p=.054, **Fig. S16C**). Yet, branch analysis revealed no difference between Hets and WTs (**Fig. S16H, I**), and a Sholl analysis showed no differences in spatial aspects of dendritic morphology (**Fig. 16F, S16J**). These results indicate altered passive properties of Het neurons in juvenile visual cortex are not caused by morphological changes, but do not rule out the possibility of morphology changes in other brain regions.

I next asked whether MYT1L haploinsufficiency affects synaptic strength or numbers in these neurons. Thus, I measured miniature excitatory postsynaptic currents (mEPSCs, **Fig. S16K**). I saw no change in the frequency (**Fig. S16L**), but I did see a trend towards increased mean amplitude of mEPSCs across cells (**Fig. S16M**). More immature cortical neurons have larger mEPSCs (Desai et al. 2002). Investigating all individual mEPSC events revealed they were indeed shifted towards larger currents (**Fig. 16G**). Since excitation/inhibition (E/I) balance is often disrupted in NDDs (Gogolla et al. 2009; Nelson and Valakh 2015)(Gogolla, I also measured miniature inhibitory postsynaptic currents (mIPSC, **Fig. S16N**) to examine E/I balance in Het mice. With no change in mIPSC amplitude, there was a small decrease of mIPSC frequency, though not significant (p=.081) (**Fig. S16O, P**). I further looked at mEPSC and mIPSC charge and found that the distribution of charge carried by individual postsynaptic current events shifted towards increased excitation (p=.024) but decreased inhibition (p=.030) in Het neurons (**Fig. 16H, I**). These results suggest MYT1L loss leads to increased E/I ratio in the mouse brain. Morphologically, microscopic investigation of apical dendritic spine density and morphological maturity (**Fig. 16J**) revealed increased spine density (**Fig. 16K**) with decreased mature spines (mushroom) but increased immature spines (thin and stubby) in Hets (**Fig. 16L, M**). Neurons generate excessive spines during development and spine numbers decrease via pruning afterwards (Bhatt, Zhang, and Gan 2009). Thus, increased spine density again indicated disrupted maturation of Het neurons. However, we did not see mEPSC frequency increase in Het neurons, suggesting extra spines may be immature or non-functional.

4.2.2.2 MYT1L loss alters the ratio of deep/upper layer neurons in mouse cortex

A previous *in vitro* study has shown MYT1L knockdown increased the ratio of deep layer (DL)/upper layer (UL) numbers (Heavner et al. 2020). Also, my *in vivo* data suggest there is an

upregulation of a master deep layer neuron regulator, CTIP2, in Het PFC. Thus, I first investigated whether MYT1L constitutive Het knockouts, mimicking the gene dose of MYT1L Syndrome patients, can also result in similar phenotypes in mice. First, I re-evaluated the RNA-seq dataset from MYT1L mutant E14 CTX and *Myt1l* heterozygous (Het) PFC. With Gene Set Enrichment Analysis (GSEA), I found there is a significantly increased expression of deep layer (DL) neuron signature genes in mutant E14 CTX compared with WT (**Fig. 17A**), while upper layer (UL) neuron signature genes remain unchanged (**Fig. 17B**), though UL genes would not yet normally be expressed by E14, thus this may not be conclusive. The expression of DL genes is even more significantly up-regulated in the adult Het PFC (**Fig. 17C**), and UL genes demonstrate significant down-regulation (**Fig. 17D**), suggesting the impact of MYT1L loss on DL and UL gene expression continues even after brain development, and is not a transient effect. As DL neurons are in an earlier neurodevelopmental trajectory than UL upper layer neurons, such an up-regulation of DL neuron genes upon MYT1L loss emphasizes MYT1L's repressive effects on neurodevelopment programs throughout development.

One possible explanation for the adult RNA-seq pattern is that Hets have more DL neurons. Thus, to test this hypothesis and examine MYT1L's role in regulating neuronal localization *in vivo*, I performed staining of the P60 Het cortex with neuronal layer specific markers (**Fig. 17E, F**). As expected, I found that Het mice have reduced brain weights compared with WT littermates (**Fig. 17G**), consistent with previous findings. Consistent with my hypothesis, I found Het cortices have increased deep layer neuron (labeled by CTIP2 protein, encoded by the *Bcl11b* gene) density compared with WT littermates (**Fig. 17E, H**). On the other hand, upper layer neurons (labeled by BRN2, encoded by the *Pou3f2 gene*) did not show altered density in Het cortices (**Fig. 17F, I**). In the RNA-seq, MYT1L loss did incur much smaller effects on upper layer neuron genes (**Fig. 17B,**

D), which might not be distinguishable by immunochemistry experiments. In sum, both RNA-seq and immunochemistry validation experiments showed MYT1L loss also altered the ratio of DL/UL neurons in the adult mouse cortex.

4.3 Discussion

4.3.1 A model of how MYT1L orchestrates neuronal development in the mouse brain

MYT1L has been shown to repress non-neuronal genes to facilitate neuronal differentiation in MEF reprogramming. Integrating MYT1L CUT&RUN and multi-omics data, I defined an additional role for MYT1L in repressing earlier neuronal development programs in the adult mouse CTX. I proposed that MYT1L normally binds to both promoter and enhancer regions in postmitotic but immature neurons, recruits the SIN3B repressor complex containing HDAC2, and erases active histone marks to suppress earlier neuronal development genes (**Fig. 18A**) once the early neuronal development phase is complete. Shutting down earlier neuronal programs may allow postmitotic neurons to further mature to their final neuronal identities. Indeed, MYT1L Het PFC showed aberrant activation of promoters, enhancers, and thus gene expression associated with early neuronal development (**Fig. 13, 14**), suggesting neurons are trapped in an immature stage. This epigenetic alteration may explain the disrupted transcriptional, morphological, and electrophysiological properties observed in this model. Loss of such suppression on early neuron developmental programs can lead to not only neuronal immaturity in the adult brain, but also early activation of neuronal differentiation programs during the development. Consequently, in this MYT1L Syndrome mouse model, precocious neuronal differentiation from progenitors to immature neurons was observed upon MYT1L loss in developing cortex. This results in fewer

proliferating cells, slower proliferating rate, fewer total neurons generated, and ultimately microcephaly in adults (**Fig. 18B**).

4.3.2 Summary

In this chapter, I validated genetic findings from Chapter 3 that MYT1L loss leads to decreased cell proliferation and precocious neuronal differentiation, echoing its repressive roles on earlier neuronal development programs. I also performed functional studies on synaptic transmission as well as neuronal morphology in the juvenile mouse visual cortex and showed that MYT1L haploinsufficiency disrupted normal neuronal maturation in terms of synaptic connections. Furthermore, lamination by histology I demonstrated that MYT1L takes part in organizing cortical, consistent with *in vitro* studies as well as *in vivo* genetics. Lastly, integrating both molecular and cellular studies that I have performed in this dissertation, I proposed models of how MYT1L regulates neuronal development and how its LoF leads to adult mouse microcephaly, shedding light on some aspects of the human MYT1L Syndrome's etiology.

4.4 Materials and Methods

4.4.1 Animal models

All procedures using mice were approved by the Institutional Care and Use Committee at Washington University School of Medicine. All mice used in this study were bred and maintained in the vivarium at Washington University in St. Louis in individually ventilated (36.2 x 17.1 x 13 cm) or static (28.5 x 17.5 x 12 cm; post-weaning behavior only) translucent plastic cages with corncob bedding and *ad libitum* access to standard lab diet and water. Animals were kept at 12/12 hour light/dark cycle, and room temperature (20-22°C) and relative humidity (50%) were controlled automatically. For all experiments, adequate measures were taken to minimize any pain

or discomfort. Breeding pairs for experimental cohorts comprised *Myt1l* Hets and wild type C57BL/6J mice (JAX Stock No. 000664) to generate male and female *Myt1l* Het and WT littermates. For embryonic CUT&RUN, *Myt1l* Het x Het breeding pairs were used to generate *Myt1l* WT and homozygous mutant littermates. Animals were weaned at P21, and group-housed by sex and genotype, until tissue harvest at P60 of age. Biological replicates for all experiments were sex and genotype balanced.

4.4.2 Method Details

Immunofluorescence

Mice brains were dissected out at different developmental stages and fixed in 4% paraformaldehyde (PFA) overnight at 4°C. After gradient sucrose dehydration and O.C.T. compound embedding, brains were sectioned using Leica Cryostat (15 μm for E14 brains and 30 μm for postnatal brains). Antigen retrieval was performed by boiling sections in 95°C 10 nM sodium citrate (pH 6.0, 0.05% Tween-20) for 10 mins. Then, sections were incubated in the blocking buffer (5% normal donkey serum, 0.1% Triton X-100 in PBS) at RT for 1 hour. Primary antibodies, including anti-MYT1L (1:500, 25234-1-AP, Proteintech), anti-MAP2 (1:200, #188044, SYSY), anti-SOX2 (1:200, sc-17320, Santa Cruz), anti-TBR2 (1:400, AB15894, Millipore), anti-Ki-67 (1:500, #14-5698-82, Invitrogen), anti-CTIP2 (1:500, ab18465, Abcam), anti-BRN2 (1:500, sc-393324, Santa Cruz), anti-NEUN (1:500, #12943, Cell Signaling), anti-GFAP (1:500, ab53554, Abcam), anti-OLIG2 (1:200, AF2418, R&D Systems), and anti-TBR1 (1:500, ab31940, Abcam) were used to detect different cell markers. Next, sections were incubated in fluorescence conjugated secondary antibodies, including donkey anti-rabbit (Alexa 488, 546, and 647, Invitrogen), donkey anti-mouse (Alexa 546, Invitrogen), donkey anti-chicken (Alexa 488, Jackson ImmunoResearch), donkey anti-rat (Alexa 488 and 647, Invitrogen), and donkey anti-goat

(Alexa 488 and 647, Jackson ImmunoResearch) at 1:500 dilution for 2 hours in RT. Images were captured under Zeiss Confocal Microscope or Zeiss Axio Scan Slide Scanner and cell counting was performed using ImageJ. In order to compare cell numbers of different cell types across genotypes, we had 5 WT, 6 Het, and 5 KO E14 brains for cell counting experiments. And we had 6 WT, 6 Het, and 5 KO E14 brains to quantify the Ki-67 positive cells.

EdU labeling

I performed intraperitoneal injection on E14 timed-pregnant females with EdU solution (50mg/kg). For the cell proliferation assay, I waited for 1.5 hours before harvesting embryonic brains. Brains were dissected and fixed with 4% PFA at 4°C overnight. Then I dehydrated and sectioned brains into 15 μm sections on glass slides as described in the immunofluorescence section. Those sections were subjected to EdU detection assay using Click-iT EdU Cell Proliferation Kit for Imaging Alexa Fluor-594 (Invitrogen) with manufacturer instructions. 4 animals per genotype were used for the cell proliferation assay.

For the cell cycle existing assay, I waited for 20 hours before harvesting brains. The same procedure was conducted on fixed brains to get 15 μm sections. Then, antigen retrieval was performed by boiling sections in 95°C 10 nM sodium citrate (pH 6.0, 0.05% Tween-20) for 10 mins. Brain sections were first incubated with anti-Ki-67 primary antibody and Alexa488-fluorescence conjugated secondary antibody before EdU detection assay. EdU+/Ki67+ cells represent neuronal progenitors that remained in the cell cycle, while EdU+/Ki67- cells represent differentiating progenitors that exited the cell cycle. I calculated the Q fraction values as the ratio between EdU+/Ki67- cells and total EdU+ cells to assess the portion of cells starting differentiation within the 20-hour time window. All images were captured under Zeiss Confocal Microscope and

cell counting was performed using ImageJ. 4 animals per genotype were used for cell cycle existing assay.

Slice Preparation

Coronal brain slices (325 μm) containing V1 were obtained as previously described (Lambo and Turrigiano, 2013) using chilled (1°C) standard artificial CSF (ACSF). ACSF was continuously oxygenated and contained the following (in mm): 126 NaCl, 3 KCl, 2 MgSO4, 1 NaHPO4, 25 NaHCO3, 2 CaCl2, and 14 Dextrose. Slices were cut on a Leica VT1000S vibratome and incubated on a semipermeable membrane covered by room temperature oxygenated standard ACSF.

Slice Electrophysiology

V1m was identified, and whole-cell patch-clamp recordings obtained from layer 2/3 pyramidal neurons, as previously described (Lambo and Turrigiano 2013). In brief, V1m was identified using the mouse brain atlas after adjusting for the lambda-bregma distance for age. The shape and morphology of the white matter were used to identify V1m. Neurons were visualized with a 40× water-immersion objective using infrared-differential interference contrast optics. Internal recording solution contained (mm): 20 KCl, 100 K-gluconate, 10 HEPES, 4 Mg-ATP, 0.3 Na-GTP, 10 phosphocreatine, and 0.4% biocytin. For AMPA miniature EPSC (mEPSC) recordings, neurons were voltage-clamped to −70 mV in standard ACSF containing TTX (0.2 μm), APV (50 μm), and picrotoxin (20 μm) and warmed to 33°C. For AMPA miniature IPSC (mIPSC) recordings, internal recording solution contained (mM): 120 KCl, 10 HEPES, 4 Mg-ATP, 0.3 Na-GTP, 2.5 phosphocreatine, and 0.2% biocytin. Neurons were voltage-clamped to -70 mV in standard ACSF containing TTX (0.2 μm), APV (50 μm), and DNQX (20 μm). For all recordings, Neurons were excluded from analyses if the resting membrane potential was more positive than

−50 mV, input resistance was <40 MΩ, series resistance was >20 MΩ, or if any of these parameters changed by >20% during the recording. Pyramidal neurons were identified by the presence of an apical dendrite and tear-drop shaped soma and morphology was confirmed by post hoc reconstruction of biocytin fills, as described previously (Desai et al., 2002). All physiology data were analyzed using Clampfit (Molecular Devices) and custom software written in Python (available at github.com/hengenlab). We recorded 24 neurons from 9 WT animals and 22 neurons from 9 Het animals to compare the passive properties as well as mEPSC (100 events for each recorded neuron) activities across genotypes. We also recorded the mIPSC of 17 neurons from 5 WT animals and 22 neurons from 5 Het animals to assess the E/I balance.

Neuronal Morphology Analysis

Brain slices from slice electrophysiology were subjected to histochemical analysis using NEUN antibody to confirm neuron identity and streptavidin Alex Fluor-568 (Invitrogen) to label injected biocytin for morphology assessment. Stained sections were mounted in cell gasket with SlowFade Diamond Antifade Mountant (Invitrogen). Images for neuronal body and dendrites were taken under Zeiss LSM 880 Airyscan Confocal Microscope. I used Neurolucida 360 (https://www.mbfbioscience.com/neurolucida360) to trace the neuronal body (15 neurons from 8 WT animals, 14 neurons from 8 Het animals) and dendrites (10 neurons from 5 WT animals, 10 neurons from 6 Het animals) and count different types of dendritic spines (10 neurons from 4 WT animals, 7 neurons from 4 Het animals). Branch analysis and Sholl analysis were performed using Neurolucida Explorer (https://www.mbfbioscience.com/neurolucida-explorer). Then I exported measurements for soma surface area, soma volume, total dendrite number, total dendritic length, average dendrite length, dendrite node number, and complexity ([Sum of the terminal orders + Number of terminals] * [Total dendritic length / Number of primary dendrites]), branch number,

branch length, total spine density, and density of different spine subtypes to compare neuron morphological maturation between Hets and WTs.

Gene Set Enrichment Analysis (GSEA)

GSEA was performed as described before (Subramanian et al. 2005) using GSEA v4.2.3 (https://www.gsea-msigdb.org/gsea/index.jsp). Deep layer neuron and upper layer neuron gene lists were obtained from Heavner et al., 2020. All analysis was performed with "gene_set" as permutation type and 1,000 permutations. Significant enrichment was determined by FDR < 0.1 cut-off.

Histopathology

Mice (5 WTs and 5 Hets for BRN2 staining, 7 WTs and 6 Hets for CTIP2 staining, sex balanced, at the age of P60) were deeply anesthetized and transcardially perfused with 4% paraformaldehyde in PBS. Whole brains were weighed and serially sectioned in the coronal plane at 75 μm using a vibratome and immunolabeled for either CTIP2 (a marker for cortical layers V/VI) or BRN2 (a marker for cortical layers II-IV). For each antibody, a set consisting of every eighth section was isolated and slide mounted. After drying overnight, antigen retrieval was performed by immersing in citrate buffer (pH 6.0) and pressure cooking for 10 minutes. The slides were then quenched in 3% hydrogen peroxide in absolute methanol for 10 minutes, immersed for 1 hour in a blocking solution (2% bovine serum albumin, 0.2% dry milk, 0.8% TX-100 in PBS), and incubated overnight with a 1:500 dilution of either Ctip2 (CAT#ab18465; Abcam, Burlington, MA) or Brn2 (CAT#sc-393324; Santa Cruz, Dallas, TX). The next morning, Ctip2 or Brn2 incubated sections were reacted with appropriate biotinylated secondary antibody for 1 hour (B7139; Sigma-Aldrich, St. Louis, MO; 1:200 or BA-9200; Vector Labs, Burlingame, CA; 1:200 respectively). The sections were then reacted with an avidin-biotin conjugate (ABC kit) for 1 hour and visualized

using the chromogen VIP (Vectastatin Elite ABC kit and Vector VIP kits; Vector Labs, Burlingame, CA).

Stereology

After immunolabeling, Ctip2 or Brn2 positive neurons were stereologically quantified using Stereoinvestigator Software (v 2019.1.3, MBF Bioscience, Williston, Vermont, USA) running on a Dell Precision Tower 5810 computer connected to a QImaging 2000R camera and a Labophot-2 Nikon microscope with electronically driven motorized stage. A rater, blind to treatment, stereologically quantified the number of positively stained cells using the unbiased optical fractionator method. To restrict counting to cortical regions with six layers, cell counts were performed on sections where the corpus callosum was visible and only in the neocortex (this excludes the allocortex, piriform, entorhinal, and retrosplenial cortices). Since each antibody labels specific cortical layers, volumes were calculated for only layers V-VI for Ctip2 and I-IV for Brn2 (Brn2 did label cells in layers V-VI but these were not counted). Finally, a density was calculated by dividing the total number of positive cells by total volume for each antibody. Since maternal care, litter size, and other factors can cause litter effects, data were normalized by dividing each value by the average of the wild-type animals within each litter.

Statistical analysis

Statistical analyses and data graphing were performed using GraphPad Prism (v.8.2.1), and R(v.4.0.0). Prior to analyses, data was screened for missing values and for the fit of distributions with assumptions underlying univariate analysis. Means and standard errors were computed for each measure. Analysis of variance (ANOVA), including repeated measures or mixed models, was used to analyze data where appropriate. One-sample *t*-tests were used to determine differences from chance. For data that did not fit univariate assumptions, non-parametric tests were used or

transformations were applied. Fisher's exact tests were used to assess MYT1L bound and unbound DAR distributions. Mann–Whitney U test was used to examine gene expression, ATAC-seq signal, and histone enrichment differences among groups. Multiple pairwise comparisons were subjected to Bonferroni correction or Dunnett correction. Figure schematics were generated using BioRender.

4.5 Acknowledgement

I thank Dr. Andrew Yoo, Dr. Brian Clark, Dr. Harrison Gabel, Dr. Kristen Kroll, Florian Colin, Nicole Hamagami, Diana Christian for technical assistance and scientific advice. Funding was provided by The Jakob Gene Fund, the Mallinckrodt Institute of Radiology at Washington University School of Medicine, McDonnell International Scholars Academy (J.C.), and the NIH: (R01MH107515, R01MH124808 to JDD, and NIH 5UL1TR002345 (ICTS) and P50 HD103525 (IDDRC)).

4.6 Figures and Tables

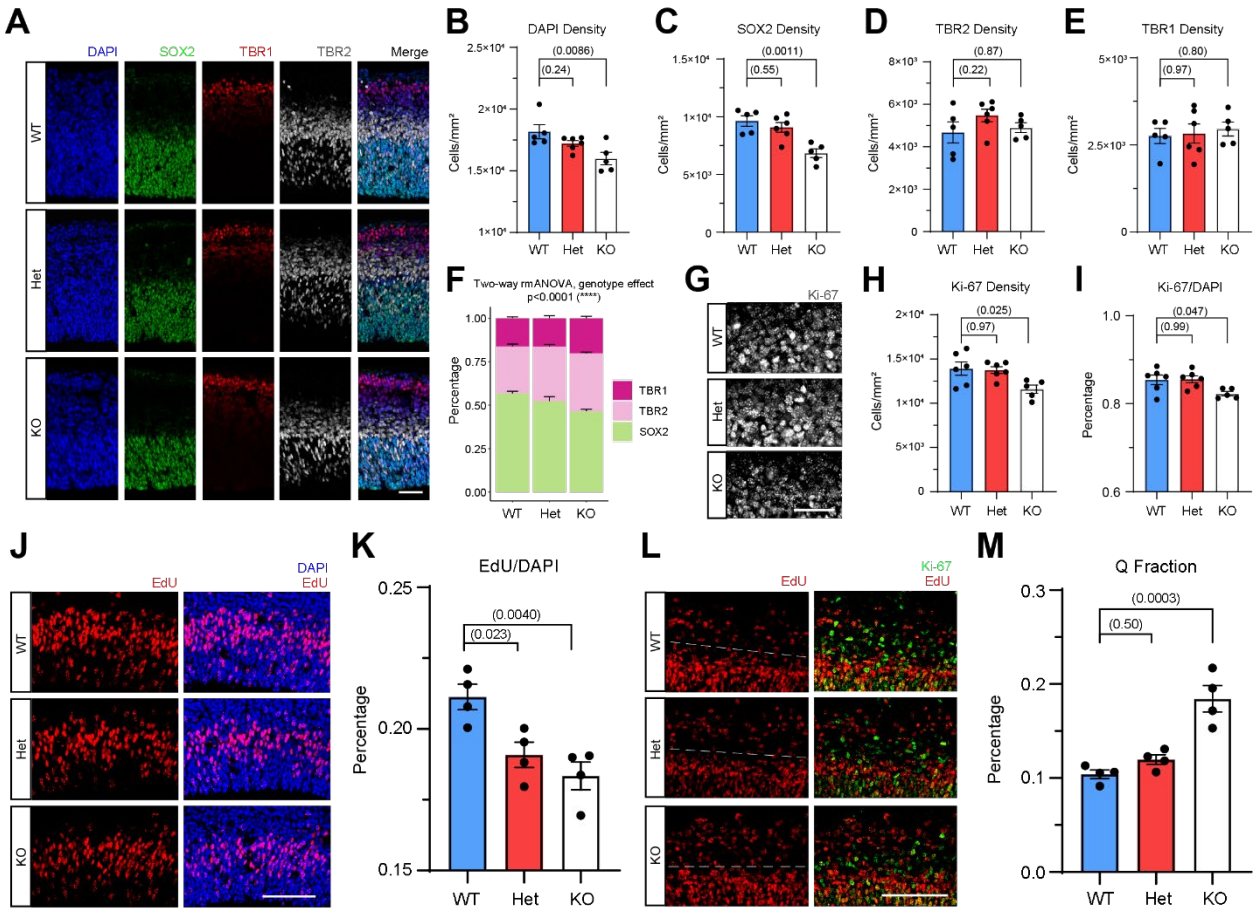

Figure 15: MYT1L loss disrupts progenitor proliferation by precocious cell cycle exit.

(A) IF for nuclei (DAPI, blue), apical progenitors (SOX2, green), intermediate progenitors (TBR2, grey) and postmitotic neurons (TBR1, red) in the E14 mouse cortex. **(B)** KO mouse cortex had significantly less cellular density, **(C)** less apical progenitors, with normal **(D)** intermediate progenitors and **(E)** postmitotic neurons. **(F)** *Myt1l* mutants have significantly more early cell stage populations but less later cell stage population. **(G-I)** KO mice have less proliferating cells compared with Het and WT littermates. **(J, K)** EdU labeling for a 1.5-hour window found decreased cell proliferation rate in mutant mouse cortex compared with WT. **(L)** Co-staining for Ki-67 and EdU (20-hours after labeling) experiments found **(M)** a larger Q fraction value in KO

but not in Het mouse cortex. White dash lines in **(L)** indicate the border where proliferating cells started to exit the cell cycle and differentiate.

*Data are represented as mean ± SEM. Scale bars, 25 μm in **A**, 50 μm in **G**, 100 μm in **J&L**. See **Table S3** for statistical test details.*

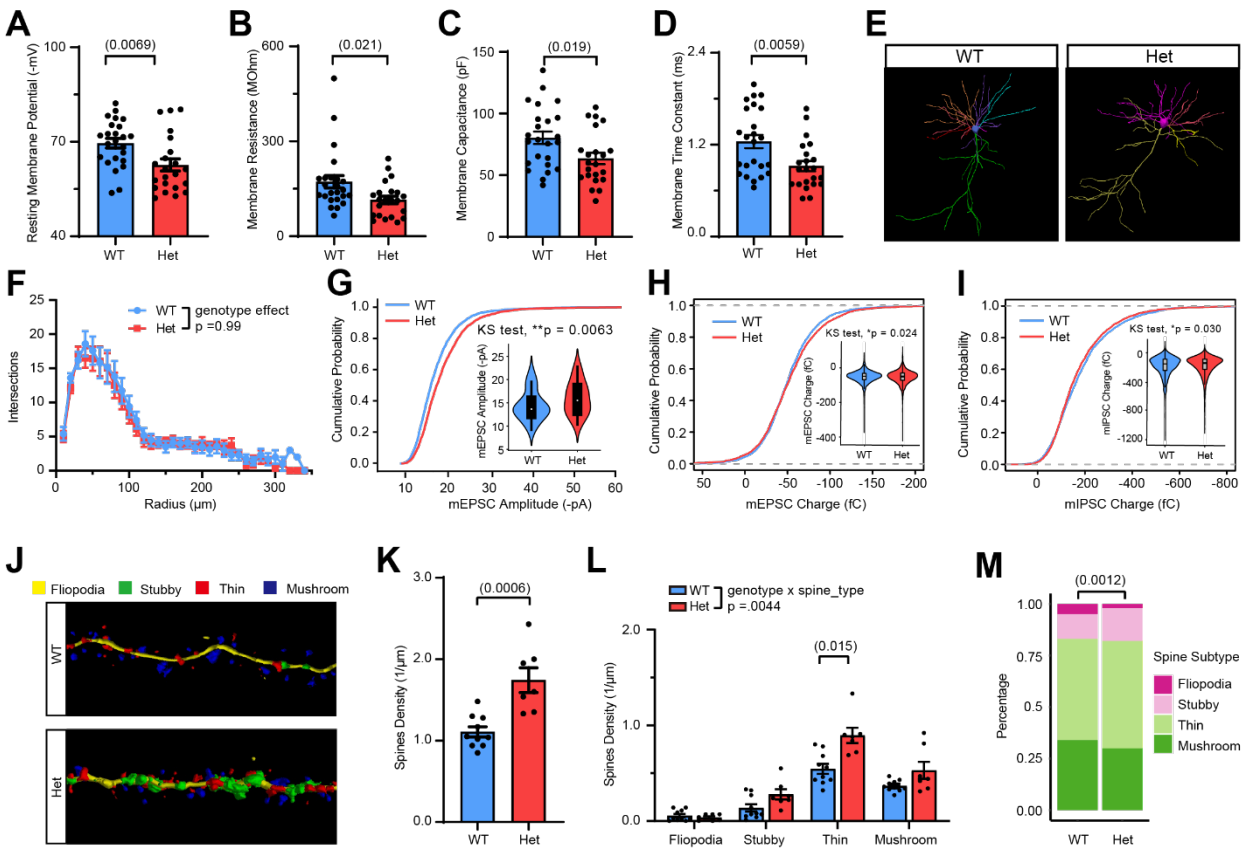

Figure 16: MYT1L haploinsufficiency disrupts baseline neuronal properties and dendritic spine maturity but not neuronal morphology.

(A) MYT1L loss led to less negative membrane potential, **(B)** reduced membrane resistance, **(C)** decreased membrane capacitance, and **(D)** smaller membrane time constant in cortical pyramidal neurons. **(E)** Neuronal soma and dendrites tracing in Neurolucida. **(F)** Sholl analysis found no dendrite complexity change across genotypes. **(G)** Het neurons showed increased mEPSC amplitudes distribution compared with WT neurons. **(H)** Analysis on individual events of mEPSC and mIPSC found that the charges of Het neurons' mEPSC are slightly larger , **(I)** while mIPSC are slightly smaller. **(J)** Representative images of spine tracing and subtypes identification using Neurolucida. **(K)** Het neurons had more apical spines with **(L)** general increase in different spine

subtypes. **(M)** Het neurons had a higher percentage of immature spines (Stubby, Thin) but less mature spines (Mushroom) compared with WT.

*Data are represented as mean ± SEM. See **Table S3** for statistical test details.*

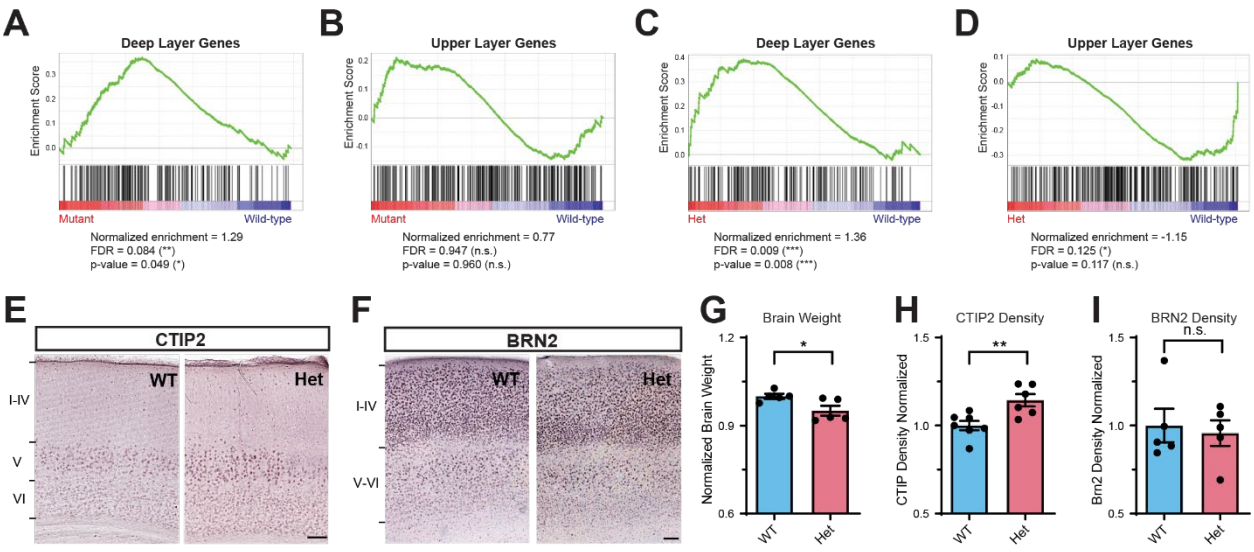

Figure 17: MYT1L controls cortical neuron layer specification.

(A) GSEA showed an up-regulation of DL genes in MYT1L mutant E14 CTX. **(B)** UL genes showed no significant change in MYT1L mutant E14 CTX. **(C)** GSEA showed an up-regulation of DL genes in MYT1L Het P60 PFC. **(D)** UL genes showed subtle but significant down-regulation in MYT1L Het P60 PFC. **(E)** Representative images of CTIP2 staining on the P60 mouse cortex. **(F)** Representative images of BRN2 staining on the P60 mouse cortex. **(G)** MYT1L Het mice have reduced brain weights compared to WTs. **(H)** MYT1L Het mice have increased CTIP2+ neuron density in cortex. (I) BRN2+ neuron density remains the same between Hets and WTs. *p<0.05, **p<0.01.

Scale bar, 100 μM. Data were represented as Mean±SEM. See ***Table S3*** *for statistical test details.*

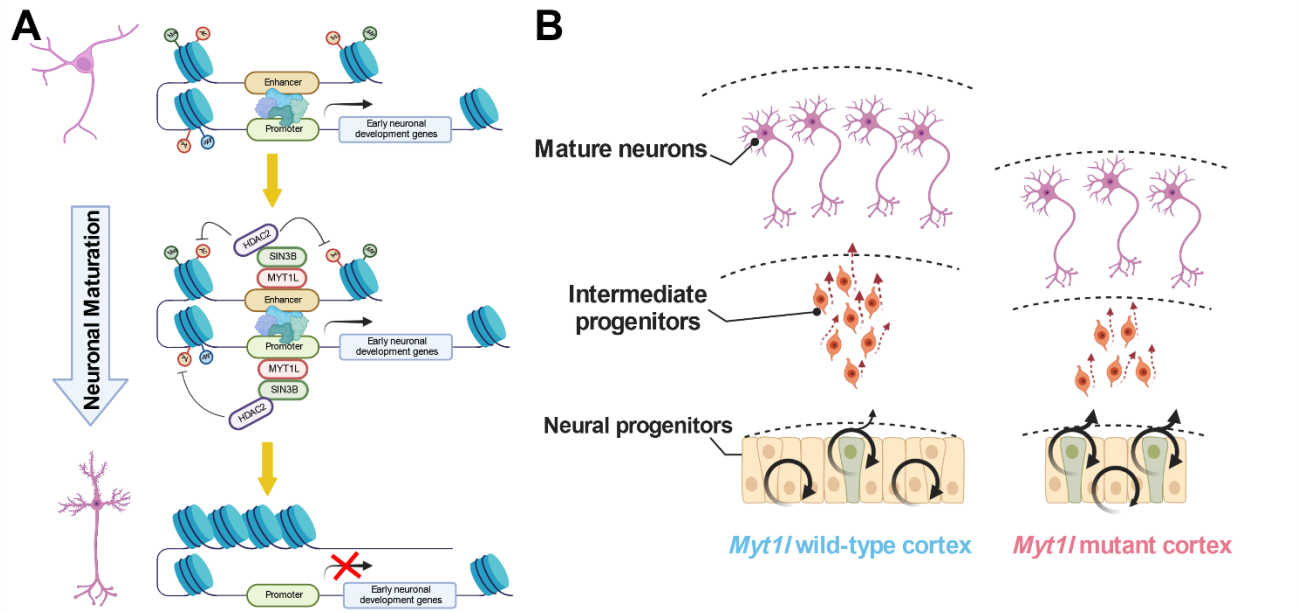

Figure 18: The models of MYT1L's molecular and cellular functions.

(A) The model for MYT1L repressing early neuronal development programs to facilitate neuronal maturation. **(B)** The diagram shows a hypothesized mechanism of microcephaly in Myt1l mutant mice at E14.

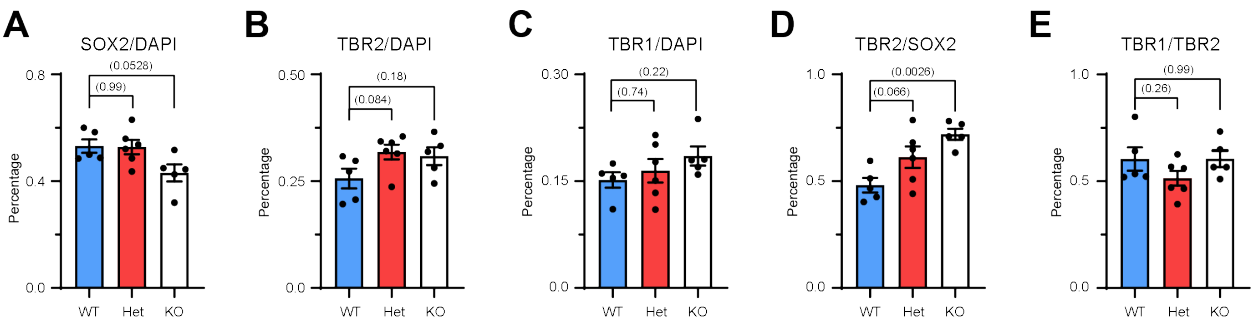

Supplemental Figure 15: MYT1L loss disrupts progenitor proliferation by precocious cell cycle exit.

(A) MYT1L KO mice tended to have decreased SOX2(+) cells density compared to WT and Het (p = 0.0528) littermates after normalizing to total cell number. **(B)** MYT1L loss did not change normalized TBR2(+) and **(C)** TBR1(+) cell density. **(D)** MYT1L loss altered early progenitor differentiation as shown by TBR2(+)/SOX2(+) ratio. **(E)** MYT1L loss did not alter late progenitor differentiation as shown by TBR1(+)/TBR2(+) ratio.

Data are represented as mean ± SEM and one-way ANOVA was performed with Dunnett correction. See ***Table S3*** *for statistical test details.*

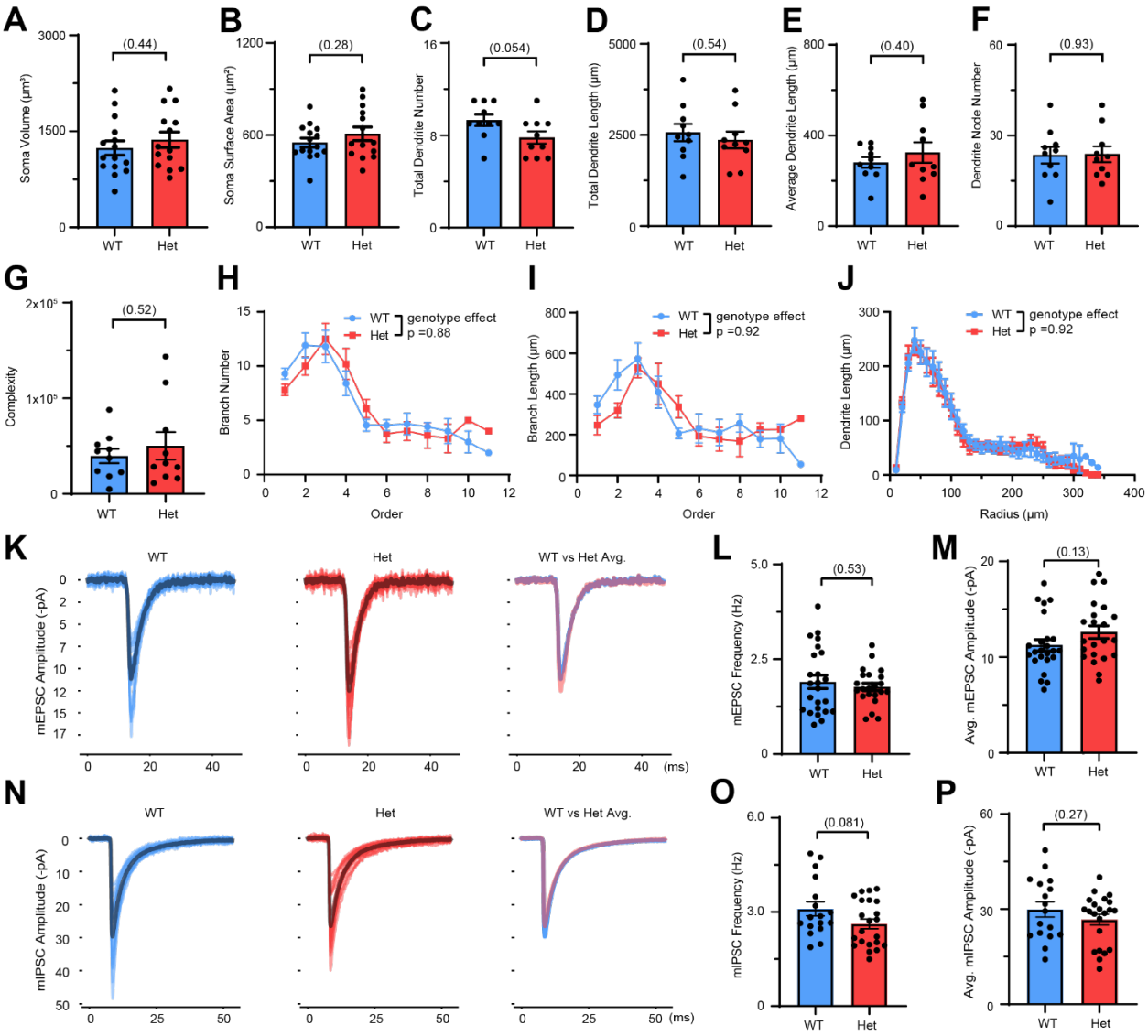

Supplemental Figure 16: MYT1L haploinsufficiency disrupts baseline neuronal properties and dendritic spine maturity but not neuronal morphology.

(A) *Myt1l* Het cortical pyramidal neurons had the same soma volume, **(B)** and soma surface area as WT. **(C)** *Myt1l* Het cortical pyramidal neurons had slightly fewer dendrite numbers compared to WT. **(D)** *Myt1l* Het cortical pyramidal neurons had the same total dendritic length, **(E)** average dendrite length, **(F)** dendrite node number, **(G)** and dendrite complexity as WT. **(H)** Branch analysis showed no branch number and **(I)** length change in Het neurons. **(J)** Sholl analysis found no dendrite length change across genotypes. **(K)** Overlapped individual mEPSC events of WT

(left) neurons, Het (middle) neurons, and averaged mEPSC events (right, blue for WT, red for Het). **(L)** MYT1L loss did not change mEPSC frequency of Het neurons. **(M)** Het neurons have non-significant slightly increased average mEPSC amplitude. **(N)** Overlapped individual mIPSC events of WT (left) neurons, Het (middle) neurons, and averaged mIPSC events (right, blue for WT, red for Het). **(O)** MYT1L loss slightly decreased mIPSC frequency with no influence on **(P)** amplitudes of Het neurons compared to WT.

*Data are represented as mean ± SEM. See **Table S3** for statistical test details.*

Supplemental Table 3. Statistical analyses for Chapter 4.

FIG	VARIABLE	COMPARISON	STATISTICAL TEST	OUTPUT
15B	DAPI density	genotype	One-way ANOVA	F(2,13)=5.852, *p*=.015
	DAPI density	Het vs WT	Dunnett's multiple comparison	*p* =.24
	DAPI density	Hom vs WT	Dunnett's multiple comparison	*p* =.0086
15C	SOX2 density	genotype	One-way ANOVA	F(2,13)=11.69, *p*=.0012
	SOX2 density	Het vs WT	Dunnett's multiple comparison	*p* =.55
	SOX2 density	Hom vs WT	Dunnett's multiple comparison	*p* =.0011
15D	TBR2 density	genotype	One-way ANOVA	F(2,13)=1.415, *p*=.28
	TBR2 density	Het vs WT	Dunnett's multiple comparison	*p* =.22
	TBR2 density	Hom vs WT	Dunnett's multiple comparison	*p* =.87
15E	TBR1 density	genotype	One-way ANOVA	F(2,13)=1.514, *p*=.85
	TBR1 density	Het vs WT	Dunnett's multiple comparison	*p* =.97
	TBR1 density	Hom vs WT	Dunnett's multiple comparison	*p* =.80
15F	Ki-67 density	genotype	Two-way rmANOVA	F(2,13)=80.63, *p*< .0001
15H	Ki-67 density	genotype	One-way ANOVA	F(2,14)=4.836, *p*=.025
	Ki-67 density	Het vs WT	Dunnett's multiple comparison	*p* =.97
	Ki-67 density	Hom vs WT	Dunnett's multiple comparison	*p* =.025
15I	Ki-67/DAPI	genotype	One-way ANOVA	F(2,14)=4.225, *p*=.037
	Ki-67/DAPI	Het vs WT	Dunnett's multiple comparison	*p* =.99
	Ki-67/DAPI	Hom vs WT	Dunnett's multiple comparison	*p* =.047
15K	EdU/DAPI	genotype	One-way ANOVA	F(2,9)=9.664, *p*=.0057

	EdU/DAPI	Het vs WT	Dunnett's multiple comparison	p =.023
	EdU/DAPI	Hom vs WT	Dunnett's multiple comparison	p =.0040
15L	Ki-67(-)/EdU(+)	genotype	One-way ANOVA	F(2,9)=22.44, p=.0003
	Ki-67(-)/EdU(+)	Het vs WT	Dunnett's multiple comparison	p =.50
	Ki-67(-)/EdU(+)	Hom vs WT	Dunnett's multiple comparison	p =.0003
S15A	SOX2/DAPI	genotype	One-way ANOVA	F(2,13)=3.968, p=.045
	SOX2/DAPI	Het vs WT	Dunnett's multiple comparison	p =.99
	SOX2/DAPI	Hom vs WT	Dunnett's multiple comparison	p =.053
S15B	TBR2/DAPI	genotype	One-way ANOVA	F(2,13)=2.660, p=.11
	TBR2/DAPI	Het vs WT	Dunnett's multiple comparison	p =.84
	TBR2/DAPI	Hom vs WT	Dunnett's multiple comparison	p =.17
S15C	TBR1/DAPI	genotype	One-way ANOVA	F(2,13)=1.368, p=.30
	TBR1/DAPI	Het vs WT	Dunnett's multiple comparison	p =.74
	TBR1/DAPI	Hom vs WT	Dunnett's multiple comparison	p =.22
S15D	TBR2/SOX2	genotype	One-way ANOVA	F(2,13)=8.196, p=.0050
	TBR2/SOX3	Het vs WT	Dunnett's multiple comparison	p =.65
	TBR2/SOX4	Hom vs WT	Dunnett's multiple comparison	p =.0026
S15R	TBR2/SOX2	genotype	One-way ANOVA	F(2,13)=1.579, p=.24
	TBR2/SOX3	Het vs WT	Dunnett's multiple comparison	p =.26
	TBR2/SOX4	Hom vs WT	Dunnett's multiple comparison	p =.99
16A	Resting membrane potential	genotype	One sample t test	t(44) =2.837, p =.0069
16B	Mmebrane capacitance	genotype	One sample t test	t(44) =2.429, p =.019

16C	Mmebrane resistance	genotype	One sample t test	t(44) =2.462, *p* =.018
16D	Membrane constant	genotype	One sample t test	t(44) =2.983, *p* =.0059
16F	Intersection	genotype x radius	Linear mixed model	F(26,331)=.5450, *p*=.97
16G	mEPSC amplitude distribution	genotype	Kolmogorov-Smirnov test	*p* =.0063
16H	mEPSC charge distribution	genotype	Kolmogorov-Smirnov test	*p* =.024
16I	mIPSC charge distribution	genotype	Kolmogorov-Smirnov test	*p* =.030
16K	Total spine denisty	genotype	One sample t test	t(15) =4.358, *p* =.0006
16L	Spine subtypes density	genotype x spine_type	Two-way rmANOVA	F(3,45)=5.0005, *p*=.0044
	Fliopodia density	genotype	Bonferroni's multiple comparison	*p* >.99
	Stubby density	genotype	Bonferroni's multiple comparison	*p* =.22
	Thin density	genotype	Bonferroni's multiple comparison	*p* =.015
	Mushroom density	genotype	Bonferroni's multiple comparison	*p* =.49
16M	Spine subtypes percentafe	genotype x spine_type	Two-way rmANOVA	F(1,15)=15.85, *p*=.0012
S16A	Soma volume	genotype	One sample t test	t(27) =.7861, *p* =.44
S16B	Soma surface area	genotype	One sample t test	t(27) =1.099, *p* =.28
S16C	Dendrite number	genotype	One sample t test	t(18) =2.060, *p* =.054
S16D	Total dendrite length	genotype	One sample t test	t(18) =0.6199, *p* =.54
S16E	Average dendrite length	genotype	One sample t test	t(18) =0.8655, *p* =.40
S16F	Dendrite node number	genotype	One sample t test	t(18) =0.07893, *p* =.94
S16G	Dendrite complexity	genotype	One sample t test	t(18) =0.6609, *p* =.52
S16H	Branch number	genotype	Linear mixed model	F(1,18)=.02542, *p*=.88
S16I	Branch length	genotype	Linear mixed model	F(1,18)=.01161, *p*=.92

S16J	Total dendrite length	genotype	Linear mixed model	F(1,18)=.009661, *p*=.92
S16L	mEPSC frequency	genotype	One sample t test	t(44) =.6273, *p* =.53
S16M	mEPSC amplitude	genotype	One sample t test	t(44) =1.527, *p* =.13
S16O	mEPSC frequency	genotype	One sample t test	t(37) =1.794, *p* =.081
S16P	mEPSC amplitude	genotype	One sample t test	t(37) =1.125, *p* =.27
17G	Brain Weight	genotype	One sample t test	t(8)=2.665, *p* =.0286
17H	CTIP2	genotype	One sample t test	t(11)=3.337, p =.0066
17I	BRN2	genotype	Mann-Whiteny U	*p* =.8413

Chapter 5: Conclusions and Future Directions

Jiayang Chen

5.1 Significance

Here, we generated a model of *Myt1l* mutation to address the role of MYT1L protein during CNS development and to comprehensively characterize the first mammalian model of MYT1L Syndrome. We confirmed that the frameshift mutation results in haploinsufficiency, ruling out a truncated protein-based mechanism. The lowered protein level leads to physical and behavioral anomalies, many of which reflect observations in patients, including microcephaly, thinned white-matter, obesity, hyperactivity, and social deficits. This indicates that these mice are a robust model of the disorder and may enable preclinical and mechanistic studies that are not possible in humans.

Utilizing this mouse model, I established a CUT&RUN technique for mapping MYT1L binding targets in the mouse brain across development. Although mouse E14 CTX MYT1L CUT&RUN lacks sensitivity due to the small proportion of postmitotic neurons where MYT1L is primarily expressed, I demonstrated CUT&RUN signals were completely absent in KO cortex, confirming excellent antibody specificity. With this clean system, I generated a high-quality map of MYT1L binding in the adult mouse PFC. This map has improved target number and MYT1L core binding motif enrichment compared to ChIP-seq studies, and especially recovers many enhancers bound by MYT1L. Furthermore, as previous MYT1L binding profiling studies have all focused on the embryonic brain or *in vitro* systems, this study will be the first mapping of MYT1L in the adult mammalian brain, suggesting that MYT1L is a neuronal TF not only important for development but also for adult CNS functions.

In Chapter 3, I also performed parallel studies on histone modifications, chromatin accessibility, and transcriptomics at the same ages and developmental time points as the MYT1L CUT&RUN. Such simultaneous measurements offered great opportunities for us to assess the direct and indirect functions of MYT1L and long-term consequences of MYT1L loss in the mouse

brain. Interestingly, I showed that MYT1L can directly activate and repress gene expression, with transcriptomic suppression as its primary role. This is echoed by LoF studies using the *Myt1l* knockout mouse line generated in this dissertation, which demonstrated elevated chromatin accessibility, gain of active histone modification marks (H3K27ac & H3K4me1/3), and increased number of up-regulated DEGs over down-regulated DEGs. In addition, with motif analysis, cross dataset comparison, and Co-IP, I was able to identify potential molecular mechanisms underlying such diverse roles of MYT1L, which likely co-binds with different co-factors to exerts distinct effects on transcription in a context dependent manner. Coupled with bulk ATAC-seq and RNA-seq data, I defined a novel role of MYT1L in directly suppressing earlier neuronal development programs in the mouse brain to facilitate neuronal differentiation and maintain neuronal identity. Loss of MYT1L during embryonic brain development, consequently, results in early activation of neuronal differentiation programs and insufficient proliferation. Likewise, in the adult brain, there is a consistent activation of developmental genes (e.g., *Eomes, Dcx*) and a lack of proper neuronal function gene expression (e.g., *Gipc1*, *Vamp2*). Such comprehensive multi-omic studies on MYT1L LoF shed light on the molecular mechanisms underlying some aspects of this syndrome and guide the downstream phenotyping experiments on cellular and circuit levels.

Despite consensus findings on MYT1L's role in facilitating neuronal differentiation both *in vitro* and now *in vivo*, how MYT1L does so remains poorly understood. Unlike the repressive effects of MYT1L overexpression on non-neuronal genes described in the transdifferentiation system (Mall et al. 2017), I found no obvious activation of non-neuronal genes upon MYT1L loss. Likewise, I observed no obvious MYT1L binding at promoters of non-neural genes (e.g., liver, fibroblasts) in the *in vivo* CUT&RUN data, in contrast to the ChIP-seq data in trans-differentiated cells. Identical effects on different targets between *in vitro* and *in vivo* systems again indicate

MYT1L's repressive functions are context dependent, and ectopic expression of MYT1L might change its functions from those under physiological conditions.

The etiology of human NDDs is extremely complicated and multi-factorial. Despite the heterogeneity, many forms of NDDs do share some common disrupted genes and dysregulated pathways (Parikshak et al. 2013; Sahin and Sur 2015; Voineagu et al. 2011). This is also reflected in our MYT1L Syndrome mouse model as it has similar dysregulated genes to other NDD mouse models and different types of human disease datasets. One interesting finding to note is that, for those overlapped genes, they were dysregulated in an opposite direction between *Myt1l* mutant mice and other NDD mouse models. This suggests that genes implicated in different NDD models are pathogenic when dysregulated in either direction. In summary, the current genetic dataset from MYT1L Syndrome mouse model opens a new window for understanding various forms of human NDDs.

Finally, I conducted a series of cellular and circuitry experiments to validate genetic findings and explore cellular mechanisms for MYT1L LoF phenotypes. Developmental studies revealed that MYT1L loss indeed decreases cell proliferation rates and triggers precocious neuronal differentiation in embryonic mouse cortex. In Het juvenile mice, V1 neurons have aberrant morphologies and electrical properties, suggesting disrupted synaptic functions. Furthermore, I found MYT1L loss leads to disrupted adult cortical neuron layer specification. In Het PFC, DL neurons, which have earlier developmental specification compared to UL neurons, showed increased corresponding gene expression and total cell number. These results line up well with genetic findings and define a mechanism for aspects of the syndrome. Specifically, the syndrome's microcephaly appears to be due to precocious differentiation of progenitors to

immature neurons. The most parsimonious interpretation is that loss of proliferating progenitors results in insufficient expansion of progenitor pools and thus, a smaller brain.

5.2 Future Directions

Adult *Myt1l* Het mice displayed multifaceted brain anatomical and behavior phenotypes. However, since MYT1L is expressed throughout development and in all postmitotic neurons, the germline knockout mouse model will not allow us to further pinpoint the critical period and neuronal subtype(s) responsible for phenotypes that we observed in the adult Het mice. Therefore, *Myt1l* conditional knockout (cKO) mice are needed to parse out developmental effects on adult phenotypes. For example, crossing *Myt1l* cKO mice with Nestin-Cre (Dubois et al. 2006) and Baf53b-Cre (Zhan et al. 2015) lines will delete MYT1L starting from stem cells and postmitotic neurons respectively. By assessing the phenotypic differences between the two crossings and comparing them with germline knockout mice, we can ask at what time point MYT1L is necessary for which aspect of brain development. In addition, Cre-lines with cell-type specificity, like Gad2-Cre for interneurons (Taniguchi et al. 2011) and AVP-Cre (Mieda et al. 2015) for AVP-positive neurons, will enable functional studies of MYT1L in different neuronal subtypes and various brain regions. These experiments will potentially provide guidance to future human disease intervention as well as drug delivery time and targets.

Although MYT1L CUT&RUN on E14 CTX showed excellent specificity, the profiling efficiency is far from optimal. This may be due to the fixed number of nuclei put into the reaction and low percentage of neurons at this age. Consequently, although most of the E14 peaks from both peak calling methods can be recovered in PFC experiments, it is hard to tell if the unique peaks from two developmental time points are derived from differential bindings of MYT1L at different ages, or rather a CUT&RUN sensitivity difference. In addition, we cannot precisely

associate multi-omics datasets from E14 CTX with MYT1L targets, making it hard to distinguish MYT1L's direct and indirect functions on early neuronal development. There are multiple options available to tackle the problem. First, CUT&RUN on more homogenous cell populations can be a direct solution. In order to get homogenous cell populations, nuclei sorting by NeuN or primary neuron cultures can be used as the CUT&RUN starting materials so that other non-neuronal cell types are filtered out beforehand. Second, single cell TF-DNA interaction profiling assays (Cammack et al. 2020; Moudgil et al. 2020; Bartosovic, Kabbe, and Castelo-Branco 2021) can also solve the problem by measuring TF binding in different cell types simultaneously. However, it can be technically challenging to apply single cell work flows on mouse brain tissue, and protocol optimization is definitely needed to determine whether the current MYT1L antibodies are compatible or not.

Evidence has suggests that MYT1L functions as both activator and repressor (Mall et al. 2017; Chen et al. 2021; Manukyan et al. 2018). To explain these two faces of MYT1L, a "ready-set-go" model has been proposed, where MYT1L co-operates with different co-factors to control neuronal gene transcription (Chen et al. 2022). Our study identified several co-factor candidates for MYT1L *in vivo*, including both transcriptional activators (SP1 and ELK1) and repressors (SIN3B), providing important hints for developing future models of how MYT1L tunes neuronal gene expression at different gene classes. With a comprehensive map of MYT1L targets generated in this study, high throughput techniques, including massive parallel reporter assays (MPRA) (Mulvey, Lagunas, and Dougherty 2021), can be leveraged in the future to further examine the motif and cofactor requirements at MYT1L targets for repression and activation respectively.

We also noticed that not all targets bound by MYT1L responded with a uniform magnitude to MYT1L heterozygosity, and this may shed some light on the phenotype in MYT1L Het mice

and haploinsufficient patients. Determining why certain MYT1L-bound genes are specifically sensitive to MYT1L levels will be another important future direction. It is interesting to note that neurite outgrowth genes, which are often disrupted, may be more dependent on neural activity dependent gene expression than other processes. Given that MYT1L often co-binds with activity dependent genes like *Fos* and *Jun* at enhancers, it may be that MYT1L is needed to turn off activity-dependent signals like these after their activation. If so, this would fit with an earlier theory suggesting IDD/ASC may be a general consequence of mistimed activity-dependent gene expression (Ebert and Greenberg 2013). This model would require further manipulations to assess its predictions in MYT1L syndrome models. For example, the monocular deprivation paradigm (Krahe and Guido 2011) can be utilized to study how MYT1L LoF interacts with visual experiences to affect visual cortex development using RNA-seq and circuit based approaches.

Finally, given that MYT1L is important for suppressing earlier neuronal developmental programs, genetic and cellular studies can be performed following a more precise developmental timeline. The same set of experiments as in this dissertation can also be performed on neonatal mouse brains since neurons are undergoing critical steps of maturation, including migration, projection, and apoptosis. Alternatively, single cell RNA-seq or spatial transcriptomic techniques (Ståhl et al. 2016; Rosenberg et al. 2018) will help assess functions of MYT1L across different developmental stages and cell types within the same brain tissue.

5.3 Summary

Collectively, in my thesis work, I developed a mouse model to understand the consequences of *Myt1l* mutation *in vivo*, inspired by a patient with a stop-gain resulting in ID, ASC, and ADHD. This mouse model mimics many common clinical phenotypes, making it a great resource for well-powered preclinical studies of potential therapeutics for MYT1L Syndrome.

Using this mouse line, I also mapped MYT1L binding targets via CUT&RUN and defined a function in suppressing earlier neuronal development programs in the mouse brain. Furthermore, I provided detailed investigations on MYT1L functions from the molecular to cellular and circuit levels, which can advance our understanding of the complex neuronal development programs in both physiological and pathological conditions. In all, this thesis work delineates functions of MYT1L during mammalian brain development and unravels how *Myt1l* mutations contribute to human disease pathogenesis.

References

Adzhubei, Ivan A., Steffen Schmidt, Leonid Peshkin, Vasily E. Ramensky, Anna Gerasimova, Peer Bork, Alexey S. Kondrashov, and Shamil R. Sunyaev. 2010. "A Method and Server for Predicting Damaging Missense Mutations." *Nature Methods* 7 (4): 248–49. https://doi.org/10.1038/nmeth0410-248.

Araujo, Daniel J., Ashley G. Anderson, Stefano Berto, Wesley Runnels, Matthew Harper, Simon Ammanuel, Michael A. Rieger, et al. 2015. "FoxP1 Orchestration of ASD-Relevant Signaling Pathways in the Striatum." *Genes & Development* 29 (20): 2081–96. https://doi.org/10.1101/gad.267989.115.

Arlotta, Paola, Bradley J. Molyneaux, Jinhui Chen, Jun Inoue, Ryo Kominami, and Jeffrey D. Macklis. 2005. "Neuronal Subtype-Specific Genes That Control Corticospinal Motor Neuron Development In Vivo." *Neuron* 45 (2): 207–21. https://doi.org/10.1016/j.neuron.2004.12.036.

Bainor, Anthony J., Siddharth Saini, Alexander Calderon, Raquel Casado-Polanco, Belén Giner-Ramirez, Claudia Moncada, David J. Cantor, Amanda Ernlund, Larisa Litovchick, and Gregory David. 2018. "The HDAC-Associated Sin3B Protein Represses DREAM Complex Targets and Cooperates with APC/C to Promote Quiescence." *Cell Reports* 25 (10): 2797-2807.e8. https://doi.org/10.1016/j.celrep.2018.11.024.

Barski, Artem, Suresh Cuddapah, Kairong Cui, Tae-Young Roh, Dustin E. Schones, Zhibin Wang, Gang Wei, Iouri Chepelev, and Keji Zhao. 2007. "High-Resolution Profiling of Histone Methylations in the Human Genome." *Cell* 129 (4): 823–37. https://doi.org/10.1016/j.cell.2007.05.009.

Bartosovic, Marek, and Gonçalo Castelo-Branco. 2022. “Multimodal Chromatin Profiling Using Nanobody-Based Single-Cell CUT&Tag.” *Nature Biotechnology*, December, 1–12. https://doi.org/10.1038/s41587-022-01535-4.

Bartosovic, Marek, Mukund Kabbe, and Gonçalo Castelo-Branco. 2021. “Single-Cell CUT&Tag Profiles Histone Modifications and Transcription Factors in Complex Tissues.” *Nature Biotechnology* 39 (7): 825–35. https://doi.org/10.1038/s41587-021-00869-9.

Bhatt, D. Harshad, Shengxiang Zhang, and Wen-Biao Gan. 2009. “Dendritic Spine Dynamics.” *Annual Review of Physiology* 71 (1): 261–82. https://doi.org/10.1146/annurev.physiol.010908.163140.

Black, Joshua C., Capucine Van Rechem, and Johnathan R. Whetstine. 2012. “Histone Lysine Methylation Dynamics: Establishment, Regulation, and Biological Impact.” *Molecular Cell* 48 (4): 491–507. https://doi.org/10.1016/j.molcel.2012.11.006.

Blanchet, Patricia, Martina Bebin, Shaam Bruet, Gregory M. Cooper, Michelle L. Thompson, Benedicte Duban-Bedu, Benedicte Gerard, et al. 2017. “MYT1L Mutations Cause Intellectual Disability and Variable Obesity by Dysregulating Gene Expression and Development of the Neuroendocrine Hypothalamus.” Edited by Zornitza Stark. *PLOS Genetics* 13 (8): e1006957. https://doi.org/10.1371/journal.pgen.1006957.

Borrie, Sarah C., Hilde Brems, Eric Legius, and Claudia Bagni. 2017. “Cognitive Dysfunctions in Intellectual Disabilities: The Contributions of the Ras-MAPK and PI3K-AKT-MTOR Pathways.” *Annual Review of Genomics and Human Genetics* 18 (1): 115–42. https://doi.org/10.1146/annurev-genom-091416-035332.

Bourgeron, Thomas. 2015. “From the Genetic Architecture to Synaptic Plasticity in Autism Spectrum Disorder.” *Nature Reviews Neuroscience* 16 (9): 551–63. https://doi.org/10.1038/nrn3992.

Boyle, Coleen A., Sheree Boulet, Laura A. Schieve, Robin A. Cohen, Stephen J. Blumberg, Marshalyn Yeargin-Allsopp, Susanna Visser, and Michael D. Kogan. 2011. “Trends in the Prevalence of Developmental Disabilities in US Children, 1997–2008.” *Pediatrics* 127 (6): 1034–42. https://doi.org/10.1542/peds.2010-2989.

Bozzi, Yuri, and Michela Fagiolini. 2020. “Animal Models of Neurodevelopmental Disorders.” *Neuroscience*, Animal Models of Neurodevelopmental Disorders, 445 (October): 1–2. https://doi.org/10.1016/j.neuroscience.2020.09.007.

Buenrostro, Jason, Beijing Wu, Howard Chang, and William Greenleaf. 2015. “ATAC-Seq: A Method for Assaying Chromatin Accessibility Genome-Wide.” *Current Protocols in Molecular Biology / Edited by Frederick M. Ausubel ... [et Al.]* 109 (January): 21.29.1-21.29.9. https://doi.org/10.1002/0471142727.mb2129s109.

Cammack, Alexander J., Arnav Moudgil, Jiayang Chen, Michael J. Vasek, Mark Shabsovich, Katherine McCullough, Allen Yen, et al. 2020. “A Viral Toolkit for Recording Transcription Factor–DNA Interactions in Live Mouse Tissues.” *Proceedings of the National Academy of Sciences* 117 (18): 10003–14. https://doi.org/10.1073/pnas.1918241117.

Carullo, Nancy V. N., and Jeremy J. Day. 2019. “Genomic Enhancers in Brain Health and Disease.” *Genes* 10 (1): 43. https://doi.org/10.3390/genes10010043.

Chen, Jiayang, Mary E. Lambo, Xia Ge, Joshua T. Dearborn, Yating Liu, Katherine B. McCullough, Raylynn G. Swift, et al. 2021. “A MYT1L Syndrome Mouse Model

Recapitulates Patient Phenotypes and Reveals Altered Brain Development Due to Disrupted Neuronal Maturation." *Neuron*, October. https://doi.org/10.1016/j.neuron.2021.09.009.

Chen, Jiayang, Allen Yen, Colin P. Florian, and Joseph D. Dougherty. 2022. "MYT1L in the Making: Emerging Insights on Functions of a Neurodevelopmental Disorder Gene." *Translational Psychiatry* 12 (1): 1–8. https://doi.org/10.1038/s41398-022-02058-x.

Cheng, Cheng, Pan-Yue Deng, Yoshiho Ikeuchi, Carla Yuede, Daofeng Li, Nicholas Rensing, Ju Huang, et al. 2018. "Characterization of a Mouse Model of Börjeson-Forssman-Lehmann Syndrome." *Cell Reports* 25 (6): 1404-1414.e6. https://doi.org/10.1016/j.celrep.2018.10.043.

Coursimault, Juliette, Anne-Marie Guerrot, Michelle M. Morrow, Catherine Schramm, Francisca Millan Zamora, Anita Shanmugham, Shuxi Liu, et al. 2021. "MYT1L-Associated Neurodevelopmental Disorder: Description of 40 New Cases and Literature Review of Clinical and Molecular Aspects." *Human Genetics*, November. https://doi.org/10.1007/s00439-021-02383-z.

———. 2022. "MYT1L-Associated Neurodevelopmental Disorder: Description of 40 New Cases and Literature Review of Clinical and Molecular Aspects." *Human Genetics* 141 (1): 65–80. https://doi.org/10.1007/s00439-021-02383-z.

Creyghton, Menno P., Albert W. Cheng, G. Grant Welstead, Tristan Kooistra, Bryce W. Carey, Eveline J. Steine, Jacob Hanna, et al. 2010. "Histone H3K27ac Separates Active from Poised Enhancers and Predicts Developmental State." *Proceedings of the National Academy of Sciences* 107 (50): 21931–36. https://doi.org/10.1073/pnas.1016071107.

Dapson, RW. 2007. “Macromolecular Changes Caused by Formalin Fixation and Antigen Retrieval.” *Biotechnic & Histochemistry* 82 (3): 133–40. https://doi.org/10.1080/10520290701567916.

De Rubeis, Silvia, Xin He, Arthur P. Goldberg, Christopher S. Poultney, Kaitlin Samocha, A. Ercument Cicek, Yan Kou, et al. 2014. “Synaptic, Transcriptional and Chromatin Genes Disrupted in Autism.” *Nature* 515 (7526): 209–15. https://doi.org/10.1038/nature13772.

Desai, Niraj S., Robert H. Cudmore, Sacha B. Nelson, and Gina G. Turrigiano. 2002. “Critical Periods for Experience-Dependent Synaptic Scaling in Visual Cortex.” *Nature Neuroscience* 5 (8): 783–89. https://doi.org/10.1038/nn878.

Drozd, Małgorzata, Barbara Bardoni, and Maria Capovilla. 2018. “Modeling Fragile X Syndrome in Drosophila.” *Frontiers in Molecular Neuroscience* 11 (April): 124. https://doi.org/10.3389/fnmol.2018.00124.

Dubois, Nicole C., Denise Hofmann, Kostas Kaloulis, J.m. Bishop, and Andreas Trumpp. 2006. “Nestin-Cre Transgenic Mouse Line Nes-Cre1 Mediates Highly Efficient Cre/LoxP Mediated Recombination in the Nervous System, Kidney, and Somite-Derived Tissues.” *Genesis* 44 (8): 355–60. https://doi.org/10.1002/dvg.20226.

Ebert, Daniel H., and Michael E. Greenberg. 2013. “Activity-Dependent Neuronal Signalling and Autism Spectrum Disorder.” *Nature* 493 (7432): 327–37. https://doi.org/10.1038/nature11860.

Francés, Lorena, Javier Quintero, Alberto Fernández, Antoni Ruiz, Jessica Caules, Gabriella Fillon, Amaia Hervás, and C. Virgínia Soler. 2022. “Current State of Knowledge on the Prevalence of Neurodevelopmental Disorders in Childhood According to the DSM-5: A

Systematic Review in Accordance with the PRISMA Criteria." *Child and Adolescent Psychiatry and Mental Health* 16 (1): 27. https://doi.org/10.1186/s13034-022-00462-1.

Gao, Tianshun, and Jiang Qian. 2020. "EnhancerAtlas 2.0: An Updated Resource with Enhancer Annotation in 586 Tissue/Cell Types across Nine Species." *Nucleic Acids Research* 48 (D1): D58–64. https://doi.org/10.1093/nar/gkz980.

Gogolla, Nadine, Jocelyn J. LeBlanc, Kathleen B. Quast, Thomas C. Südhof, Michela Fagiolini, and Takao K. Hensch. 2009. "Common Circuit Defect of Excitatory-Inhibitory Balance in Mouse Models of Autism." *Journal of Neurodevelopmental Disorders* 1 (2): 172–81. https://doi.org/10.1007/s11689-009-9023-x.

Gompers, Andrea L., Linda Su-Feher, Jacob Ellegood, Nycole A. Copping, M. Asrafuzzaman Riyadh, Tyler W. Stradleigh, Michael C. Pride, et al. 2017. "Germline Chd8 Haploinsufficiency Alters Brain Development in Mouse." *Nature Neuroscience* 20 (8): 1062–73. https://doi.org/10.1038/nn.4592.

Gopalan, Sneha, and Thomas G. Fazzio. 2022. "Multi-CUT&Tag to Simultaneously Profile Multiple Chromatin Factors." *STAR Protocols* 3 (1): 101100. https://doi.org/10.1016/j.xpro.2021.101100.

Gopalan, Sneha, Yuqing Wang, Nicholas W. Harper, Manuel Garber, and Thomas G. Fazzio. 2021. "Simultaneous Profiling of Multiple Chromatin Proteins in the Same Cells." *Molecular Cell* 81 (22): 4736-4746.e5. https://doi.org/10.1016/j.molcel.2021.09.019.

Guy, Jacky, Brian Hendrich, Megan Holmes, Joanne E. Martin, and Adrian Bird. 2001. "A Mouse Mecp2-Null Mutation Causes Neurological Symptoms That Mimic Rett Syndrome." *Nature Genetics* 27 (3): 322–26. https://doi.org/10.1038/85899.

Hayakawa, Tomohiro, Yasuko Ohtani, Noriyo Hayakawa, Kaori Shinmyozu, Motoki Saito, Fuyuki Ishikawa, and Jun-ichi Nakayama. 2007. “RBP2 Is an MRG15 Complex Component and Down-Regulates Intragenic Histone H3 Lysine 4 Methylation.” *Genes to Cells* 12 (6): 811–26. https://doi.org/10.1111/j.1365-2443.2007.01089.x.

Heavner, Whitney E., Shaoyi Ji, James H. Notwell, Ethan S. Dyer, Alex M. Tseng, Johannes Birgmeier, Boyoung Yoo, Gill Bejerano, and Susan K. McConnell. 2020. “Transcription Factor Expression Defines Subclasses of Developing Projection Neurons Highly Similar to Single-Cell RNA-Seq Subtypes.” *Proceedings of the National Academy of Sciences* 117 (40): 25074–84. https://doi.org/10.1073/pnas.2008013117.

Hedges, S. Blair. 2002. “The Origin and Evolution of Model Organisms.” *Nature Reviews Genetics* 3 (11): 838–49. https://doi.org/10.1038/nrg929.

Heintzman, Nathaniel D., Gary C. Hon, R. David Hawkins, Pouya Kheradpour, Alexander Stark, Lindsey F. Harp, Zhen Ye, et al. 2009. “Histone Modifications at Human Enhancers Reflect Global Cell-Type-Specific Gene Expression.” *Nature* 459 (7243): 108–12. https://doi.org/10.1038/nature07829.

Hu, Jian, Allen L. Ho, Liang Yuan, Baoli Hu, Sujun Hua, Soyoon Sarah Hwang, Jianhua Zhang, et al. 2013. “Neutralization of Terminal Differentiation in Gliomagenesis.” *Proceedings of the National Academy of Sciences* 110 (36): 14520–27. https://doi.org/10.1073/pnas.1308610110.

Iwase, Shigeki, Emily Brookes, Saurabh Agarwal, Aimee I Badeaux, Hikaru Ito, Christina N Vallianatos, Giulio Srubek Tomassy, et al. 2016. “A Mouse Model of X-Linked Intellectual Disability Associated with Impaired Removal of Histone Methylation.” *Cell Reports* 14 (5): 1000–1009. https://doi.org/10.1016/j.celrep.2015.12.091.

Jiang, Youhang, Victor C. Yu, Frank Buchholz, Shawn O'Connell, Simon J. Rhodes, Carlos Candeloro, Yu-Rong Xia, Aldons J. Lusis, and Michael G. Rosenfeld. 1996. "A Novel Family of Cys-Cys, His-Cys Zinc Finger Transcription Factors Expressed in Developing Nervous System and Pituitary Gland." *Journal of Biological Chemistry* 271 (18): 10723–30. https://doi.org/10.1074/jbc.271.18.10723.

Johnson, David S., Ali Mortazavi, Richard M. Myers, and Barbara Wold. 2007. "Genome-Wide Mapping of in Vivo Protein-DNA Interactions." *Science* 316 (5830): 1497–1502. https://doi.org/10.1126/science.1141319.

Jumper, John, Richard Evans, Alexander Pritzel, Tim Green, Michael Figurnov, Olaf Ronneberger, Kathryn Tunyasuvunakool, et al. 2021. "Highly Accurate Protein Structure Prediction with AlphaFold." *Nature* 596 (7873): 583–89. https://doi.org/10.1038/s41586-021-03819-2.

Jung, Youngsook L., Lovelace J. Luquette, Joshua W.K. Ho, Francesco Ferrari, Michael Tolstorukov, Aki Minoda, Robbyn Issner, et al. 2014. "Impact of Sequencing Depth in ChIP-Seq Experiments." *Nucleic Acids Research* 42 (9): e74. https://doi.org/10.1093/nar/gku178.

Kameyama, Toshiki, Fumio Matsushita, Yuzo Kadokawa, and Tohru Marunouchi. 2011. "Myt/NZF Family Transcription Factors Regulate Neuronal Differentiation of P19 Cells." *Neuroscience Letters* 497 (2): 74–79. https://doi.org/10.1016/j.neulet.2011.04.033.

Kang, Hyo Jung, Yuka Imamura Kawasawa, Feng Cheng, Ying Zhu, Xuming Xu, Mingfeng Li, André M. M. Sousa, et al. 2011. "Spatio-Temporal Transcriptome of the Human Brain." *Nature* 478 (7370): 483–89. https://doi.org/10.1038/nature10523.

Karczewski, Konrad J., Laurent C. Francioli, Grace Tiao, Beryl B. Cummings, Jessica Alföldi, Qingbo Wang, Ryan L. Collins, et al. 2020. "The Mutational Constraint Spectrum Quantified from Variation in 141,456 Humans." *Nature* 581 (7809): 434–43. https://doi.org/10.1038/s41586-020-2308-7.

Katayama, Yuta, Masaaki Nishiyama, Hirotaka Shoji, Yasuyuki Ohkawa, Atsuki Kawamura, Tetsuya Sato, Mikita Suyama, Toru Takumi, Tsuyoshi Miyakawa, and Keiichi I. Nakayama. 2016. "CHD8 Haploinsufficiency Results in Autistic-like Phenotypes in Mice." *Nature* 537 (7622): 675–79. https://doi.org/10.1038/nature19357.

Kaya-Okur, Hatice S., Derek H. Janssens, Jorja G. Henikoff, Kami Ahmad, and Steven Henikoff. 2020. "Efficient Low-Cost Chromatin Profiling with CUT&Tag." *Nature Protocols* 15 (10): 3264–83. https://doi.org/10.1038/s41596-020-0373-x.

Kaya-Okur, Hatice S., Steven J. Wu, Christine A. Codomo, Erica S. Pledger, Terri D. Bryson, Jorja G. Henikoff, Kami Ahmad, and Steven Henikoff. 2019. "CUT&Tag for Efficient Epigenomic Profiling of Small Samples and Single Cells." *Nature Communications* 10 (1): 1930. https://doi.org/10.1038/s41467-019-09982-5.

Kazdoba, Tatiana M., Prescott T. Leach, Jill L. Silverman, and Jacqueline N. Crawley. 2014. "Modeling Fragile X Syndrome in the Fmr1 Knockout Mouse." *Intractable & Rare Diseases Research* 3 (4): 118–33. https://doi.org/10.5582/irdr.2014.01024.

Kepa, Agnieszka, Lourdes Martinez Medina, Susanne Erk, Deepak P Srivastava, Alinda Fernandes, Roberto Toro, Sabine Lévi, et al. 2017. "Associations of the Intellectual Disability Gene MYT1L with Helix–Loop–Helix Gene Expression, Hippocampus Volume and Hippocampus Activation During Memory Retrieval." *Neuropsychopharmacology* 42 (13): 2516–26. https://doi.org/10.1038/npp.2017.91.

Kim, Jin G., Regina C. Armstrong, Denes v. Agoston, Alexandra Robinsky, Claudia Wiese, James Nagle, and Lynn D. Hudson. 1997. “Myelin transcription factor 1 (Myt1) of the oligodendrocyte lineage, along with a closely related CCHC zinc finger, is expressed in developing neurons in the mammalian central nervous system.” *Journal of Neuroscience Research* 50 (2): 272–90. https://doi.org/10.1002/(SICI)1097-4547(19971015)50:2<272::AID-JNR16>3.0.CO;2-A.

Kim, Young J., Sattar Khoshkhoo, Jan C. Frankowski, Bingyao Zhu, Saad Abbasi, Sunyoung Lee, Ye Emily Wu, and Robert F. Hunt. 2018. “Chd2 Is Necessary for Neural Circuit Development and Long-Term Memory.” *Neuron* 100 (5): 1180-1193.e6. https://doi.org/10.1016/j.neuron.2018.09.049.

Krahe, Thomas E., and William Guido. 2011. “Homeostatic Plasticity in the Visual Thalamus by Monocular Deprivation.” *Journal of Neuroscience* 31 (18): 6842–49. https://doi.org/10.1523/JNEUROSCI.1173-11.2011.

Lambo, Mary E., and Gina G. Turrigiano. 2013. “Synaptic and Intrinsic Homeostatic Mechanisms Cooperate to Increase L2/3 Pyramidal Neuron Excitability during a Late Phase of Critical Period Plasticity.” *Journal of Neuroscience* 33 (20): 8810–19. https://doi.org/10.1523/JNEUROSCI.4502-12.2013.

Lieschke, Graham J., and Peter D. Currie. 2007. “Animal Models of Human Disease: Zebrafish Swim into View.” *Nature Reviews Genetics* 8 (5): 353–67. https://doi.org/10.1038/nrg2091.

Ligt, Joep de, Marjolein H. Willemsen, Bregje W.M. van Bon, Tjitske Kleefstra, Helger G. Yntema, Thessa Kroes, Anneke T. Vulto-van Silfhout, et al. 2012. “Diagnostic Exome

Sequencing in Persons with Severe Intellectual Disability." *New England Journal of Medicine* 367 (20): 1921–29. https://doi.org/10.1056/NEJMoa1206524.

Loid, Petra, Riikka Mäkitie, Alice Costantini, Heli Viljakainen, Minna Pekkinen, and Outi Mäkitie. 2018. "A Novel MYT1L Mutation in a Patient with Severe Early-Onset Obesity and Intellectual Disability." *American Journal of Medical Genetics Part A* 176 (9): 1972–75. https://doi.org/10.1002/ajmg.a.40370.

Lu, Leina, Xiaoxiao Liu, Wei-Kai Huang, Paola Giusti-Rodríguez, Jian Cui, Shanshan Zhang, Wanying Xu, et al. 2020. "Robust Hi-C Maps of Enhancer-Promoter Interactions Reveal the Function of Non-Coding Genome in Neural Development and Diseases." *Molecular Cell* 79 (3): 521-534.e15. https://doi.org/10.1016/j.molcel.2020.06.007.

Machlab, Dania, Lukas Burger, Charlotte Soneson, Filippo M Rijli, Dirk Schübeler, and Michael B Stadler. 2022. "MonaLisa: An R/Bioconductor Package for Identifying Regulatory Motifs." *Bioinformatics* 38 (9): 2624–25. https://doi.org/10.1093/bioinformatics/btac102.

Malik, Athar N., Thomas Vierbuchen, Martin Hemberg, Alex A. Rubin, Emi Ling, Cameron H. Couch, Hume Stroud, et al. 2014. "Genome-Wide Identification and Characterization of Functional Neuronal Activity–Dependent Enhancers." *Nature Neuroscience* 17 (10): 1330–39. https://doi.org/10.1038/nn.3808.

Mall, Moritz, Michael S. Kareta, Soham Chanda, Henrik Ahlenius, Nicholas Perotti, Bo Zhou, Sarah D. Grieder, et al. 2017. "Myt1l Safeguards Neuronal Identity by Actively Repressing Many Non-Neuronal Fates." *Nature* 544 (7649): 245–49. https://doi.org/10.1038/nature21722.

Mansfield, Patricia, John N. Constantino, and Dustin Baldridge. 2020. "MYT1L A Systematic Review of Genetic Variation Encompassing Schizophrenia and Autism." *American*

Journal of Medical Genetics Part B: Neuropsychiatric Genetics 183 (4): 227–33. https://doi.org/10.1002/ajmg.b.32781.

Manukyan, Arkadi, Izabela Kowalczyk, Tiffany A. Melhuish, Agata Lemiesz, and David Wotton. 2018. "Analysis of Transcriptional Activity by the Myt1 and Myt1l Transcription Factors." *Journal of Cellular Biochemistry* 119 (6): 4644–55. https://doi.org/10.1002/jcb.26636.

Matsushita, Fumio, Toshiki Kameyama, Yuzo Kadokawa, and Tohru Marunouchi. 2014. "Spatiotemporal Expression Pattern of Myt/NZF Family Zinc Finger Transcription Factors during Mouse Nervous System Development: Expression of *NZF* S in Neural Development." *Developmental Dynamics* 243 (4): 588–600. https://doi.org/10.1002/dvdy.24091.

Meers, Michael P, Terri D Bryson, Jorja G Henikoff, and Steven Henikoff. 2019. "Improved CUT&RUN Chromatin Profiling Tools." Edited by Stephen Parker and Detlef Weigel. *ELife* 8 (June): e46314. https://doi.org/10.7554/eLife.46314.

Meers, Michael P., Geneva Llagas, Derek H. Janssens, Christine A. Codomo, and Steven Henikoff. 2022. "Multifactorial Profiling of Epigenetic Landscapes at Single-Cell Resolution Using MulTI-Tag." *Nature Biotechnology*, October, 1–9. https://doi.org/10.1038/s41587-022-01522-9.

Melhuish, Tiffany A., Izabela Kowalczyk, Arkadi Manukyan, Ying Zhang, Anant Shah, Roger Abounader, and David Wotton. 2018. "Myt1 and Myt1l Transcription Factors Limit Proliferation in GBM Cells by Repressing YAP1 Expression." *Biochimica et Biophysica Acta. Gene Regulatory Mechanisms* 1861 (11): 983–95. https://doi.org/10.1016/j.bbagrm.2018.10.005.

Mieda, Michihiro, Daisuke Ono, Emi Hasegawa, Hitoshi Okamoto, Ken-ichi Honma, Sato Honma, and Takeshi Sakurai. 2015. “Cellular Clocks in AVP Neurons of the SCN Are Critical for Interneuronal Coupling Regulating Circadian Behavior Rhythm.” *Neuron* 85 (5): 1103–16. https://doi.org/10.1016/j.neuron.2015.02.005.

Moudgil, Arnav, Michael N. Wilkinson, Xuhua Chen, June He, Alexander J. Cammack, Michael J. Vasek, Tomás Lagunas, et al. 2020. “Self-Reporting Transposons Enable Simultaneous Readout of Gene Expression and Transcription Factor Binding in Single Cells.” *Cell* 182 (4): 992-1008.e21. https://doi.org/10.1016/j.cell.2020.06.037.

Mullin, A. P., A. Gokhale, A. Moreno-De-Luca, S. Sanyal, J. L. Waddington, and V. Faundez. 2013. “Neurodevelopmental Disorders: Mechanisms and Boundary Definitions from Genomes, Interactomes and Proteomes.” *Translational Psychiatry* 3 (12): e329–e329. https://doi.org/10.1038/tp.2013.108.

Mulvey, Bernard, Tomás Lagunas, and Joseph D. Dougherty. 2021. “Massively Parallel Reporter Assays: Defining Functional Psychiatric Genetic Variants Across Biological Contexts.” *Biological Psychiatry*, Disentangling Psychiatric Polygenicity, 89 (1): 76–89. https://doi.org/10.1016/j.biopsych.2020.06.011.

Naruse, Yoshihisa, Tsutomu Aoki, Takuya Kojima, and Nozomu Mori. 1999. “Neural Restrictive Silencer Factor Recruits MSin3 and Histone Deacetylase Complex to Repress Neuron-Specific Target Genes.” *Proceedings of the National Academy of Sciences* 96 (24): 13691–96. https://doi.org/10.1073/pnas.96.24.13691.

Nelson, Sacha B., and Vera Valakh. 2015. “Excitatory/Inhibitory Balance and Circuit Homeostasis in Autism Spectrum Disorders.” *Neuron* 87 (4): 684–98. https://doi.org/10.1016/j.neuron.2015.07.033.

Nishibuchi, Gohei, Yukimasa Shibata, Tomohiro Hayakawa, Noriyo Hayakawa, Yasuko Ohtani, Kaori Sinmyozu, Hideaki Tagami, and Jun-ichi Nakayama. 2014. "Physical and Functional Interactions between the Histone H3K4 Demethylase KDM5A and the Nucleosome Remodeling and Deacetylase (NuRD) Complex *." *Journal of Biological Chemistry* 289 (42): 28956–70. https://doi.org/10.1074/jbc.M114.573725.

Oh, Seung Wook, Julie A. Harris, Lydia Ng, Brent Winslow, Nicholas Cain, Stefan Mihalas, Quanxin Wang, et al. 2014. "A Mesoscale Connectome of the Mouse Brain." *Nature* 508 (7495): 207–14. https://doi.org/10.1038/nature13186.

Parenti, Ilaria, Luis G. Rabaneda, Hanna Schoen, and Gaia Novarino. 2020. "Neurodevelopmental Disorders: From Genetics to Functional Pathways." *Trends in Neurosciences* 43 (8): 608–21. https://doi.org/10.1016/j.tins.2020.05.004.

Parikshak, Neelroop N., Rui Luo, Alice Zhang, Hyejung Won, Jennifer K. Lowe, Vijayendran Chandran, Steve Horvath, and Daniel H. Geschwind. 2013. "Integrative Functional Genomic Analyses Implicate Specific Molecular Pathways and Circuits in Autism." *Cell* 155 (5): 1008–21. https://doi.org/10.1016/j.cell.2013.10.031.

Park, Peter J. 2009. "ChIP–Seq: Advantages and Challenges of a Maturing Technology." *Nature Reviews Genetics* 10 (10): 669–80. https://doi.org/10.1038/nrg2641.

Perlman, Robert L. 2016. "Mouse Models of Human Disease: An Evolutionary Perspective." *Evolution, Medicine, and Public Health* 2016 (1): 170–76. https://doi.org/10.1093/emph/eow014.

Romm, Elena, Joseph A. Nielsen, Jin G. Kim, and Lynn D. Hudson. 2005. "Myt1 Family Recruits Histone Deacetylase to Regulate Neural Transcription." *Journal of Neurochemistry* 93 (6): 1444–53. https://doi.org/10.1111/j.1471-4159.2005.03131.x.

Ronan, Jehnna L., Wei Wu, and Gerald R. Crabtree. 2013. “From Neural Development to Cognition: Unexpected Roles for Chromatin.” *Nature Reviews Genetics* 14 (5): 347–59. https://doi.org/10.1038/nrg3413.

Rosenberg, Alexander B., Charles M. Roco, Richard A. Muscat, Anna Kuchina, Paul Sample, Zizhen Yao, Lucas T. Graybuck, et al. 2018. “Single-Cell Profiling of the Developing Mouse Brain and Spinal Cord with Split-Pool Barcoding.” *Science* 360 (6385): 176–82. https://doi.org/10.1126/science.aam8999.

Sahin, Mustafa, and Mriganka Sur. 2015. “Genes, Circuits, and Precision Therapies for Autism and Related Neurodevelopmental Disorders.” *Science* 350 (6263): aab3897. https://doi.org/10.1126/science.aab3897.

Sanders, Stephan J. 2015. “First Glimpses of the Neurobiology of Autism Spectrum Disorder.” *Current Opinion in Genetics & Development*, Molecular and genetic bases of disease, 33 (August): 80–92. https://doi.org/10.1016/j.gde.2015.10.002.

Satterstrom, F. Kyle, Jack A. Kosmicki, Jiebiao Wang, Michael S. Breen, Silvia De Rubeis, Joon-Yong An, Minshi Peng, et al. 2020. “Large-Scale Exome Sequencing Study Implicates Both Developmental and Functional Changes in the Neurobiology of Autism.” *Cell* 180 (3): 568-584.e23. https://doi.org/10.1016/j.cell.2019.12.036.

Sessa, Alessandro, Luca Fagnocchi, Giuseppina Mastrototaro, Luca Massimino, Mattia Zaghi, Marzia Indrigo, Stefano Cattaneo, et al. 2019. “SETD5 Regulates Chromatin Methylation State and Preserves Global Transcriptional Fidelity during Brain Development and Neuronal Wiring.” *Neuron* 104 (2): 271-289.e13. https://doi.org/10.1016/j.neuron.2019.07.013.

Skene, Peter J., Jorja G. Henikoff, and Steven Henikoff. 2018. “Targeted in Situ Genome-Wide Profiling with High Efficiency for Low Cell Numbers.” *Nature Protocols* 13 (5): 1006–19. https://doi.org/10.1038/nprot.2018.015.

Skene, Peter J, and Steven Henikoff. 2017. “An Efficient Targeted Nuclease Strategy for High-Resolution Mapping of DNA Binding Sites.” Edited by Danny Reinberg. *ELife* 6 (January): e21856. https://doi.org/10.7554/eLife.21856.

Solomon, Mark J., Pamela L. Larsen, and Alexander Varshavsky. 1988. “Mapping ProteinDNA Interactions in Vivo with Formaldehyde: Evidence That Histone H4 Is Retained on a Highly Transcribed Gene.” *Cell* 53 (6): 937–47. https://doi.org/10.1016/S0092-8674(88)90469-2.

Ståhl, Patrik L., Fredrik Salmén, Sanja Vickovic, Anna Lundmark, José Fernández Navarro, Jens Magnusson, Stefania Giacomello, et al. 2016. “Visualization and Analysis of Gene Expression in Tissue Sections by Spatial Transcriptomics.” *Science* 353 (6294): 78–82. https://doi.org/10.1126/science.aaf2403.

Straub, Loreen, Brian T. Bateman, Sonia Hernandez-Diaz, Cassandra York, Barry Lester, Katherine L. Wisner, Christopher J. McDougle, et al. 2022. “Neurodevelopmental Disorders Among Publicly or Privately Insured Children in the United States.” *JAMA Psychiatry* 79 (3): 232–42. https://doi.org/10.1001/jamapsychiatry.2021.3815.

Subramanian, Aravind, Pablo Tamayo, Vamsi K. Mootha, Sayan Mukherjee, Benjamin L. Ebert, Michael A. Gillette, Amanda Paulovich, et al. 2005. “Gene Set Enrichment Analysis: A Knowledge-Based Approach for Interpreting Genome-Wide Expression Profiles.” *Proceedings of the National Academy of Sciences* 102 (43): 15545–50. https://doi.org/10.1073/pnas.0506580102.

Suliman-Lavie, Reut, Ben Title, Yahel Cohen, Nanako Hamada, Maayan Tal, Nitzan Tal, Galya Monderer-Rothkoff, et al. 2020. “Pogz Deficiency Leads to Transcription Dysregulation and Impaired Cerebellar Activity Underlying Autism-like Behavior in Mice.” *Nature Communications* 11 (1): 5836. https://doi.org/10.1038/s41467-020-19577-0.

Taniguchi, Hiroki, Miao He, Priscilla Wu, Sangyong Kim, Raehum Paik, Ken Sugino, Duda Kvitsani, et al. 2011. “A Resource of Cre Driver Lines for Genetic Targeting of GABAergic Neurons in Cerebral Cortex.” *Neuron* 71 (6): 995–1013. https://doi.org/10.1016/j.neuron.2011.07.026.

Tasic, Bosiljka, Zizhen Yao, Lucas T. Graybuck, Kimberly A. Smith, Thuc Nghi Nguyen, Darren Bertagnolli, Jeff Goldy, et al. 2018. “Shared and Distinct Transcriptomic Cell Types across Neocortical Areas.” *Nature* 563 (7729): 72–78. https://doi.org/10.1038/s41586-018-0654-5.

Tian, Bing, Jun Yang, and Allan R. Brasier. 2012. “Two-Step Cross-Linking for Analysis of Protein–Chromatin Interactions.” In *Transcriptional Regulation: Methods and Protocols*, edited by Ales Vancura, 105–20. Methods in Molecular Biology. New York, NY: Springer. https://doi.org/10.1007/978-1-61779-376-9_7.

Tomaz, Diogo Miguel Rosa. 2016. “Insights on the Function of MyT1L in Ascl1 Mediated Neuronal Reprogramming,” January. https://repositorio.ul.pt/handle/10451/25009.

Varadi, Mihaly, Stephen Anyango, Mandar Deshpande, Sreenath Nair, Cindy Natassia, Galabina Yordanova, David Yuan, et al. 2022. “AlphaFold Protein Structure Database: Massively Expanding the Structural Coverage of Protein-Sequence Space with High-Accuracy Models.” *Nucleic Acids Research* 50 (D1): D439–44. https://doi.org/10.1093/nar/gkab1061.

Vierbuchen, Thomas, Austin Ostermeier, Zhiping P. Pang, Yuko Kokubu, Thomas C. Südhof, and Marius Wernig. 2010a. “Direct Conversion of Fibroblasts to Functional Neurons by Defined Factors.” *Nature* 463 (7284): 1035–41. https://doi.org/10.1038/nature08797.

———. 2010b. “Direct Conversion of Fibroblasts to Functional Neurons by Defined Factors.” *Nature* 463 (7284): 1035–41. https://doi.org/10.1038/nature08797.

Voineagu, Irina, Xinchen Wang, Patrick Johnston, Jennifer K. Lowe, Yuan Tian, Steve Horvath, Jonathan Mill, Rita M. Cantor, Benjamin J. Blencowe, and Daniel H. Geschwind. 2011. “Transcriptomic Analysis of Autistic Brain Reveals Convergent Molecular Pathology.” *Nature* 474 (7351): 380–84. https://doi.org/10.1038/nature10110.

Wang, Tianyun, Hui Guo, Bo Xiong, Holly A. F. Stessman, Huidan Wu, Bradley P. Coe, Tychele N. Turner, et al. 2016. “De Novo Genic Mutations among a Chinese Autism Spectrum Disorder Cohort.” *Nature Communications* 7 (1): 13316. https://doi.org/10.1038/ncomms13316.

Wapinski, Orly L., Thomas Vierbuchen, Kun Qu, Qian Yi Lee, Soham Chanda, Daniel R. Fuentes, Paul G. Giresi, et al. 2013. “Hierarchical Mechanisms for Direct Reprogramming of Fibroblasts to Neurons.” *Cell* 155 (3): 621–35. https://doi.org/10.1016/j.cell.2013.09.028.

Windheuser, Isabelle C., Jessica Becker, Kirsten Cremer, Hela Hundertmark, Laura M. Yates, Elisabeth Mangold, Sophia Peters, et al. 2020. “Nine Newly Identified Individuals Refine the Phenotype Associated with *MYT1L* Mutations.” *American Journal of Medical Genetics Part A* 182 (5): 1021–31. https://doi.org/10.1002/ajmg.a.61515.

Wu, Steven J., Scott N. Furlan, Anca B. Mihalas, Hatice S. Kaya-Okur, Abdullah H. Feroze, Samuel N. Emerson, Ye Zheng, et al. 2021. “Single-Cell CUT&Tag Analysis of

Chromatin Modifications in Differentiation and Tumor Progression." *Nature Biotechnology* 39 (7): 819–24. https://doi.org/10.1038/s41587-021-00865-z.

Xie, Donghua, Ruoyu Duan, Chen Li, Zhiqun Xie, Aihua Wang, Lili Xiong, Jianhui Wei, et al. 2022. "Study on the Economic Burden of Neurodevelopmental Diseases on Patients With Genetic Diagnosis." *Frontiers in Public Health* 10. https://www.frontiersin.org/articles/10.3389/fpubh.2022.887796.

Yasumura, Akira, Mikimasa Omori, Ayako Fukuda, Junichi Takahashi, Yukiko Yasumura, Eiji Nakagawa, Toshihide Koike, et al. 2019. "Age-Related Differences in Frontal Lobe Function in Children with ADHD." *Brain and Development* 41 (7): 577–86. https://doi.org/10.1016/j.braindev.2019.03.006.

Zhan, Xiaoming, Mou Cao, Andrew S. Yoo, Zilai Zhang, Lei Chen, Gerald R. Crabtree, and Jiang I. Wu. 2015. "Generation of BAF53b-Cre Transgenic Mice with Pan-Neuronal Cre Activities." *Genesis* 53 (7): 440–48. https://doi.org/10.1002/dvg.22866.

Appendix

Table 1: Key Resource Table

REAGENT or RESOURCE	SOURCE	IDENTIFIER
Antibodies		
Rabbit anti-MYT1L	Proteintech	25234-1-AP
Rabbit anti-MYT1L	Millipore	ABE2915
Guinea pig anti-MAP2	Synaptic Systems	#188044
Goat anti-SOX2	Santa Cruz	sc-17320
Mouse anti-SIN3B	Santa Cruz	sc-13145
Mouse anti-HDAC1	Santa Cruz	sc-81598
Mouse anti-HDAC2	Santa Cruz	sc-9959
Chicken anti-TBR2	Millipore	AB15894
Rat anti-TBR2	Invitrogen	#14-4875-82
Rat anti-Ki67	Invitrogen	# 14-5698-82
Rat anti-CTIP2	Abcam	ab18465
Mouse anti-BRN2	Santa Cruz	sc-393324
Rabbit anti-NEUN	Cell Signaling	#12943
Goat anti-GFAP	Abcam	ab53554
Goat anti-OLIG2	R&D Systems	AF2418
Rabbit anti-TBR1	Abcam	ab31940
Mouse anti-GAPDH	Sigma	G8795

Donkey anti-rabbit, Alexa Fluor 488	Invitrogen	A-21206
Donkey anti-rabbit, Alexa Fluor 546	Invitrogen	A10040
Donkey anti-rabbit, Alexa Fluor 647	Invitrogen	A-31573
Donkey anti-chicken, Alexa Fluor 488	Jackson Immuno Research	#703-545-155
Donkey anti-rat, Alexa Fluor 488	Invitrogen	A48269
Donkey anti-rat, Alexa Fluor 647	Invitrogen	A48272
Donkey anti-muose, Alexa Fluor 546	Invitrogen	A10036
Donkey anti-goat, Alexa Fluor 488	Jackson Immuno Research	705-546-147
Donkey anti-goat, Alexa Fluor 647	Jackson Immuno Research	705-605-003
Goat anti-mouse IgG (H+L)-HRP conjugate	Bio-Rad	#1706516
Goat anti-rabbit IgG (H+L)-HRP conjugate	Millipore	AP307P
Oligonucleotides		
Myt1l S710fsX founder screening	This dissertation	F(5'-3'): GGCCTAACCACACTGTCCTC; R(5'-3'): CACAAGTTAGGGCTGGAGGG
Myt1l S710fsX PCR genotyping (WT)	This dissertation	F(5'-3'): ATGTCGCAGTAGCCAAGTC; R(5'-3'): TCTTGCTACACGTGCTACT
Myt1l S710fsX PCR genotyping (Mut)	This dissertation	F(5'-3'): ATGTCGCAGTAGCCAAGTC; R(5'-3'): TCTTGCTACACGTACTGGA

Myt1l S710fsX Sanger sequencing	This dissertation	F(5'-3'): ACCTGTTAGTCACATGAGG; R(5'-3'): TGGTGGAGATGCCTATCTC
1st PCR for illumina sequencing	This dissertation	F(5'-3'): GTGACTGGAGTTCAGACGTGTGCTCTTCCGATCT CAAGCGGTACTGCAAGAATG; R(5'-3'): ACACTCTTTCCCTACACGACGCTCTTCCGATCTC TGTGGCATTTCACGACAAC
2nd PCR for illumina sequencing_001	This dissertation	F(5'-3'): AATGATACGGCGACCACCGAGATCTACACTCTTT CCCTACACGACGCTCTTCCGATCT; R(5'-3'): CAAGCAGAAGACGGCATACGAGATACCGGTGTC GTGACTGGAGTTCAGACGTGTGCTCTTCCGA
2nd PCR for illumina sequencing_002	This dissertation	F(5'-3'): AATGATACGGCGACCACCGAGATCTACACTCTTT CCCTACACGACGCTCTTCCGATCT; R(5'-3'): CAAGCAGAAGACGGCATACGAGATAAGAGATGT GTGACTGGAGTTCAGACGTGTGCTCTTCCGA
2nd PCR for illumina sequencing_003	This dissertation	F(5'-3'): AATGATACGGCGACCACCGAGATCTACACTCTTT CCCTACACGACGCTCTTCCGATCT; R(5'-3'): CAAGCAGAAGACGGCATACGAGATCTTCACACA GTGACTGGAGTTCAGACGTGTGCTCTTCCGA
2nd PCR for illumina sequencing_004	This dissertation	F(5'-3'): AATGATACGGCGACCACCGAGATCTACACTCTTT CCCTACACGACGCTCTTCCGATCT; R(5'-3'): CAAGCAGAAGACGGCATACGAGATCAAATCGGA GTGACTGGAGTTCAGACGTGTGCTCTTCCGA
2nd PCR for illumina sequencing_005	This dissertation	F(5'-3'): AATGATACGGCGACCACCGAGATCTACACTCTTT CCCTACACGACGCTCTTCCGATCT; R(5'-3'): CAAGCAGAAGACGGCATACGAGATGGTCCCTAA GTGACTGGAGTTCAGACGTGTGCTCTTCCGA
2nd PCR for illumina sequencing_006	This dissertation	F(5'-3'): AATGATACGGCGACCACCGAGATCTACACTCTTT CCCTACACGACGCTCTTCCGATCT; R(5'-3'): CAAGCAGAAGACGGCATACGAGATCCTTCTGTG GTGACTGGAGTTCAGACGTGTGCTCTTCCGA
2nd PCR for illumina sequencing_007	This dissertation	F(5'-3'): AATGATACGGCGACCACCGAGATCTACACTCTTT CCCTACACGACGCTCTTCCGATCT; R(5'-3'): CAAGCAGAAGACGGCATACGAGATTCCGTATTA GTGACTGGAGTTCAGACGTGTGCTCTTCCGA
2nd PCR for illumina sequencing_008	This dissertation	F(5'-3'): AATGATACGGCGACCACCGAGATCTACACTCTTT CCCTACACGACGCTCTTCCGATCT; R(5'-3'):

		CAAGCAGAAGACGGCATACGAGATACTTGGGCA GTGACTGGAGTTCAGACGTGTGCTCTTCCGA
2nd PCR for illumina sequencing_009	This dissertation	F(5'-3'): AATGATACGGCGACCACCGAGATCTACACTCTTT CCCTACACGACGCTCTTCCGATCT; R(5'-3'): CAAGCAGAAGACGGCATACGAGATTCCTCCAAA GTGACTGGAGTTCAGACGTGTGCTCTTCCGA
2nd PCR for illumina sequencing_010	This dissertation	F(5'-3'): AATGATACGGCGACCACCGAGATCTACACTCTTT CCCTACACGACGCTCTTCCGATCT; R(5'-3'): CAAGCAGAAGACGGCATACGAGATTAGCAAAAC GTGACTGGAGTTCAGACGTGTGCTCTTCCGA
MYT1L qPCR	This dissertation	F(5'-3'): ACTATCAAGCAGCGAGCCAG; R(5'-3'): CATGTCAGCCTCCATCTGGG
GAPDH qPCR	This dissertation	F(5'-3'): AGGTCGGTGTGAACGGATTTG; R(5'-3'): GGGGTCGTTGATGGCAACA
ATAC-seq i5 adapter_001	This dissertation	AATGATACGGCGACCACCGAGATCTACACGTAA GGAGTCGTCGGCAGCGTCAGATGTG
ATAC-seq i5 adapter_002	This dissertation	AATGATACGGCGACCACCGAGATCTACACCTCT CTATTCGTCGGCAGCGTCAGATGTG
ATAC-seq i5 adapter_003	This dissertation	AATGATACGGCGACCACCGAGATCTACACTATC CTCTTCGTCGGCAGCGTCAGATGTG
ATAC-seq i7 adapter_001	This dissertation	ACATCTCCGAGCCCACGAGACTAAGGCGAATCT CGTATGCCGTCTTCTGCTTG
ATAC-seq i7 adapter_002	This dissertation	ACATCTCCGAGCCCACGAGACCGTACTAGATCT CGTATGCCGTCTTCTGCTTG
ATAC-seq i7 adapter_003	This dissertation	ACATCTCCGAGCCCACGAGACAGGCAGAAATCT CGTATGCCGTCTTCTGCTTG
ATAC-seq i7 adapter_004	This dissertation	ACATCTCCGAGCCCACGAGACTCCTGAGCATCTC GTATGCCGTCTTCTGCTTG
ATAC-seq i7 adapter_005	This dissertation	ACATCTCCGAGCCCACGAGACGGACTCCTATCTC GTATGCCGTCTTCTGCTTG
ATAC-seq i7 adapter_006	This dissertation	ACATCTCCGAGCCCACGAGACTAGGCATGATCT CGTATGCCGTCTTCTGCTTG
ATAC-seq i7 adapter_007	This dissertation	ACATCTCCGAGCCCACGAGACCTCTCTACATCTC GTATGCCGTCTTCTGCTTG
ATAC-seq i7 adapter_008	This dissertation	ACATCTCCGAGCCCACGAGACCAGAGAGGATCT CGTATGCCGTCTTCTGCTTG
ATAC-seq i7 adapter_009	This dissertation	ACATCTCCGAGCCCACGAGACGCTACGCTATCTC GTATGCCGTCTTCTGCTTG
ATAC-seq i7 adapter_010	This dissertation	ACATCTCCGAGCCCACGAGACCGAGGCTGATCT CGTATGCCGTCTTCTGCTTG
ATAC-seq i7 adapter_011	This dissertation	ACATCTCCGAGCCCACGAGACGTAGAGGAATCT CGTATGCCGTCTTCTGCTTG

ATAC-seq i7 adapter_012	This dissertation	ACATCTCCGAGCCCACGAGACGTCGTGATATCTC GTATGCCGTCTTCTGCTTG
ATAC-seq i7 adapter_013	This dissertation	ACATCTCCGAGCCCACGAGACACCACTGTATCTC GTATGCCGTCTTCTGCTTG
ATAC-seq i7 adapter_014	This dissertation	ACATCTCCGAGCCCACGAGACTGGATCTGATCTC GTATGCCGTCTTCTGCTTG
ATAC-seq i7 adapter_015	This dissertation	ACATCTCCGAGCCCACGAGACCCGTTTGTATCTC GTATGCCGTCTTCTGCTTG
ATAC-seq i7 adapter_016	This dissertation	ACATCTCCGAGCCCACGAGACTGCTGGGTATCTC GTATGCCGTCTTCTGCTTG
ATAC-seq i7 adapter_017	This dissertation	ACATCTCCGAGCCCACGAGACAGGTTGGGATCT CGTATGCCGTCTTCTGCTTG
ATAC-seq i7 adapter_018	This dissertation	ACATCTCCGAGCCCACGAGACAAGAGGCAATCT CGTATGCCGTCTTCTGCTTG
CUT&RUN i5 adapter_11	This dissertation	AATGATACGGCGACCACCGAGATCTACACCGCG GTTCACACTCTTTCCCTACACGACGCTCTTCCGA TCT
CUT&RUN i5 adapter_12	This dissertation	AATGATACGGCGACCACCGAGATCTACACTATA ACCTACACTCTTTCCCTACACGACGCTCTTCCGA TCT
CUT&RUN i5 adapter_13	This dissertation	AATGATACGGCGACCACCGAGATCTACACAAGG ATGAACACTCTTTCCCTACACGACGCTCTTCCGA TCT
CUT&RUN i5 adapter_14	This dissertation	AATGATACGGCGACCACCGAGATCTACACGGAA GCAGACACTCTTTCCCTACACGACGCTCTTCCGA TCT
CUT&RUN i5 adapter_15	This dissertation	AATGATACGGCGACCACCGAGATCTACACTGAC GAATACACTCTTTCCCTACACGACGCTCTTCCGA TCT
CUT&RUN i5 adapter_16	This dissertation	AATGATACGGCGACCACCGAGATCTACACCAGT AGGCACACTCTTTCCCTACACGACGCTCTTCCGA TCT
CUT&RUN i5 adapter_17	This dissertation	AATGATACGGCGACCACCGAGATCTACACATAT TCACACACTCTTTCCCTACACGACGCTCTTCCGA TCT
CUT&RUN i5 adapter_18	This dissertation	AATGATACGGCGACCACCGAGATCTACACGCGC CTGTACACTCTTTCCCTACACGACGCTCTTCCGA TCT
CUT&RUN i7 adapter_01	This dissertation	GATCGGAAGAGCACACGTCTGAACTCCAGTCAC CCGCGGTTATCTCGTATGCCGTCTTCTGCTTG
CUT&RUN i7 adapter_02	This dissertation	GATCGGAAGAGCACACGTCTGAACTCCAGTCAC TTATAACCATCTCGTATGCCGTCTTCTGCTTG
CUT&RUN i7 adapter_03	This dissertation	GATCGGAAGAGCACACGTCTGAACTCCAGTCAC GGACTTGGATCTCGTATGCCGTCTTCTGCTTG

CUT&RUN i7 adapter_04	This dissertation	GATCGGAAGAGCACACGTCTGAACTCCAGTCAC AAGTCCAAATCTCGTATGCCGTCTTCTGCTTG
CUT&RUN i7 adapter_05	This dissertation	GATCGGAAGAGCACACGTCTGAACTCCAGTCAC ATCCACTGATCTCGTATGCCGTCTTCTGCTTG
CUT&RUN i7 adapter_06	This dissertation	GATCGGAAGAGCACACGTCTGAACTCCAGTCAC GCTTGTCAATCTCGTATGCCGTCTTCTGCTTG
CUT&RUN i7 adapter_07	This dissertation	GATCGGAAGAGCACACGTCTGAACTCCAGTCAC CAAGCTAGATCTCGTATGCCGTCTTCTGCTTG
CUT&RUN i7 adapter_08	This dissertation	GATCGGAAGAGCACACGTCTGAACTCCAGTCAC TGGATCGAATCTCGTATGCCGTCTTCTGCTTG
Experimental Models: Organism		
Mouse, C57BL/6J, Myt1l S710fsX knockin	This dissertation/Jax	#036428
Mouse, C57BL/6J, Wild-type	The Jackson Laboratory	#000664
Commercial Assays		
Click-iT EdU Cell Proliferation Kit for Imaging Alexa Fluor-594	Invitrogen	C10339
qScript cDNA synthesis Kit	QuantaBio	#95047
Zymo RNA Clean and ConcentratorTM-5 kit	Zymo Research	R1014
KAPA Hyper Prep Kit	Roche	KK8504
Critical Commercial Reagents		
Streptavidin, Alexa Fluor™ 568 conjugate	Invitrogen	S11226
SYBR Green Master Mix	Thermo Fisher	#4309155
BioMag®Plus Concanavalin A	Bangs Labs	86057-3
CUTANA™ pAG-Mnase	EpiCypher	SKU: 15-1016

Software and algorithms		
R	https://www.r-project.org/	R version 4.0.0
Fiji / ImageJ	https://fiji.sc	v2.0.0
GraphPad Prism	https://www.graphpad.com	v8.0
FastQC	https://www.bioinformatics.babraham.ac.uk/projects/fastqc/	v0.11.9
Trimmomatic	(Bolger et al., 2014)	v0.39
Bowtie2	http://bowtie-bio.sourceforge.net/bowtie2/index.shtml	v2.4.0
STAR	https://github.com/alexdobin/STAR	v2.7.0
ITK-SNAP	http://www.itksnap.org/pmwiki/pmwiki.php	v3.8.0
Samtools	http://www.htslib.org	v1.12
Picard	https://github.com/broadinstitute/picard/releases/tag/2.25.2	v2.25.2
Macs2	(Zhang et al., 2008)	N/A
Homer	(Heinz et al., 2010)	v4.11
edgeR	(Robinson et al., 2010)	v3.12
RUVseq	(Risso et al., 2014)	v3.12
DeepTools	https://deeptools.readthedocs.io/en/develop/	v2.0
HTSeq	(Anders et al., 2015)	v0.11.1
Cytoscape	https://cytoscape.org/	v3.8.0

GSEA	(Subramanian et al., 2005)	v4.0.3
BioMart	(Durinck et al., 2009)	N/A
ChIPpeakAnno	(Zhu et al., 2010)	v2.0.5
Metagene2	https://github.com/ArnaudDroitLab/metagene2	v3.13
BioRender	https://app.biorender.com/	
Data Deposit		
RNA-seq	Gene Expression Ominibus	GSE173943
ATAC-seq	Gene Expression Ominibus	GSE173943
CUT&RUN	Gene Expression Ominibus	GSE161252

Table 2: Characterization of *Myt1l* Index patient.

Clinical Characteristic	Proband
Mutation location	chr2: 1895969 (hg19): c.2117dupG, p.S707QfsX56
Social Responsiveness Scale-2	100
Developmental delay	Yes
Speech delay	Yes
ASD	Moderate (age 4 Dx)
Intellectual Disability	Yes
Eye contact	Deficit
Repetitive behavior	Yes
WASI-II IQ	47 (56, verbal; 47 perceptual)
ADHD	Yes
Depression and Anxiety	Subtle Anxiety
BMI (no hyperphagia)	99th percentile
Seizure history	No
MRI	Normal
Dysmorphia	No

We note that the index patient was a male who had been diagnosed with ASC in early childhood; he exhibited sustained pathognomonic features of the condition including repetitive thinking, subtle stereotypic motor mannerisms, deficiency in eye gaze, and interpersonal aloofness when focused on the objects of his own mental pursuits, fully consistent with DSM5 level 1 severity of impairment in function ("requiring support"). He required frequent verbal (rarely physical) redirection for silliness, perseveration, or engagement in non-preferred tasks. His stereotypic behaviors included repetitive hand wringing, body rocking, stereotypic tensing and vocalizing behaviors. These ASC symptoms were out of proportion to social impairments that would be attributable to the comorbid conditions of ADHD and mild ID with which he was also diagnosed, and he displayed the compensatory strength of a distinct affability (at times to the point of joviality) and enjoyment of social interaction despite the quality and consistency of social interaction being compromised by his ASC symptoms. He required a full time paraprofessional in his early school years, but responded significantly to the combination of clonidine and bupropion

for improvement in hyperactivity, impulsivity, and aggression, and over time he made incremental gains in composure as well as improved impulse control. By early adolescence he had mastered enough social interest and competency that he was described as “the mayor” of a summer camp, and he was participating avidly in a musical band. He is able to read, and is very conversational; he has a sense of humor, has made friends, and enjoys telling jokes; his interpersonal exchanges remain silly at times, overly chatty, over-focused on topics of interest to him, and with marginal eye contact and some degree of residual fidgetiness. Medical comorbidities have included obesity and idiopathic scoliosis of adolescence.